1   *Revision 1, Manuscript submission 4*

2

3   **Eu speciation in apatite at 1 bar: an experimental study of valence-state**

4   **partitioning by XANES, lattice strain and Eu/Eu* in basaltic systems**

5

6   Nicholas D. Tailby[1,2], Dustin Trail[3], E. Bruce Watson, Antonio Lanzirotti[4], Matthew Newville[4], Yanling

7   Wang[3]

8   [1]Department of Earth and Planetary Sciences, American Museum of Natural History, Central Park West

9   at 79th St, New York, 10024-5192, U.S.A.

10   **[2]**Department of Earth and Environmental Sciences, Rensselaer Polytechnic Institute, Jonsson-Rowland

11   Science Center, Troy, New York, 12180, U.S.A.

12   [3]Department of Earth and Environmental Sciences, University of Rochester, Rochester, NY, 14627, U.S.A.

13   **[4]**GSE-CARS, University of Chicago, Chicago, Illinois,60637, U.S.A.

14

15   **Abstract**

16   Partition coefficients for rare earth elements (REEs) between apatite and basaltic melt were determined

17   as a function of oxygen fugacity (f_{O_2}; iron-wüstite to hematite-magnetite buffers) at 1 bar and between

18   1110 and 1175 °C. Apatite-melt partitioning data for REE^{3+} (La, Sm, Gd, Lu) show near constant values at

19   all experimental conditions, while bulk Eu becomes more incompatible (with an increasing negative

20   anomaly) with decreasing f_{O_2}. Experiments define three apatite calibrations that can theoretically be

21   used as redox sensors. The first, a XANES calibration that directly measures Eu valence in apatite,

22   requires saturation at similar temperature-composition conditions to experiments and is defined by:

$$\left(\frac{\mathrm{Eu}^{3+}}{\Sigma\mathrm{Eu}}\right)_{\mathrm{Apatite}} = \frac{1}{1 + 10^{-0.10\pm0.01\times\log(f_{O_2})-1.63\pm0.16}}$$

23   The second technique involves analysis of Sm, Eu and Gd in both apatite and coexisting basaltic melt

24   (glass), and is defined by:

$$\left(\frac{\mathrm{Eu}}{\mathrm{Eu}*}\right)_{D}^{\sqrt{\mathrm{Sm}\times\mathrm{Gd}}} = \frac{1}{1 + 10^{-0.15\pm0.03\times\log(f_{O_2})-2.46\pm0.41}}$$

25   The third technique is based on the lattice strain model and also requires analysis of REE in both apatite

26   and basalt. This calibration is defined by:

$$\left(\frac{\mathrm{Eu}}{\mathrm{Eu}*}\right)_{D}^{\mathrm{lattice\ strain}} = \frac{1}{1 + 10^{-0.20\pm0.03\times\log(f_{O_2})-3.03\pm0.42}}$$

27

28   From an application perspective, the Eu valence-state partitioning techniques based on ($\sqrt{\mathrm{Sm}\times\mathrm{Gd}}$) and

29   lattice strain are virtually indistinguishable, such that either methodology is valid. Application of any of

30   these three calibrations is best carried out in systems where both apatite and co-existing glass are

31   present and in direct contact with one another. In holocrystalline rocks, whole rock analyses can be used

32   as a guide to melt composition, but considerations and corrections must be made to either lattice strain

33   or $\sqrt{(\mathrm{Sm}\times\mathrm{Gd})}$ to ensure that the effect of plagioclase crystallization either prior to or during apatite

34   growth can be removed. Similarly, if the melt source has an inherited either a positive or negative Eu

35   anomaly, appropriate corrections must also be made to lattice strain or $\sqrt{(\mathrm{Sm}\times\mathrm{Gd})}$ techniques that

36   are based on whole rock analyses. This being the case, if apatite is primary and saturates from the

37   parent melt early during the crystallization sequence, these corrections may be minimal.

38   In addition to redox calibrations, the partition coefficients for the REE range from a maximum $D_{Eu^{3+}}$ =

39   1.67 ± 0.25 (as determined by lattice strain) to $D_{Lu^{3+}}$ = 0.69± 0.10. The REE partition coefficient pattern,

40   as observed in the Onuma diagram, is in a fortuitous situation where the most compatible REE (Eu^{3+}) is

41   also the polyvalent element used to monitor f_{O_2}. These experiments provide a quantitative means of

42   assessing Eu anomalies in apatite and how they be used to constrain the oxygen fugacity of silicate

43   melts.

44

45

46

47   **Keywords**: apatite, europium, Eu/Eu*, XANES, oxygen fugacity, f_{O_2}, valence, anomaly, KREEP, basalt,

48   lunar, merrillite, Jim Webster.

49

50

51 **Introduction**

52 The similar valence state observed among the rare earth elements (REE), along with systematically

53 decreasing the ionic radii from La→Lu, lead to a generally coherent behavior for this group of elements,

54 with predicable features in silicate melts and minerals (Trail et al., 2012; Burnham and Berry, 2012).

55 There are two notable exceptions – (i) Ce commonly shows a positive excursion and (ii) Eu can show

56 positive/negative excursions from an otherwise smooth trend when normalized to chondrite or host

57 medium concentrations (noting that simultaneous positive Eu deviations and negative Ce deviations are

58 also possible in certain natural systems; for examples see Hoskin and Schaltegger, 2003; Trail et al.,

59 2015; Kato et al., 2002; Elderfield et al., 1981; Plank and Langmuir, 1998). These positive and/or

60 negative excursions, generally known as anomalies, occur because Ce and Eu exhibit polyvalent behavior

61 over the oxygen fugacity (f_{O_2}) range observed in the terrestrial bodies (e.g., Earth, Moon, Mars, Vesta).

62 Here we focus on apatite-basalt partitioning of Eu valence species (Eu^{2+} and Eu^{3+}) to calibrate a new

63 apatite redox (f_{O_2}) sensor. As the two Eu valence species show notably different ionic radii ($^{[VI]}Eu^{2+}$ =

64 1.17 Å and $^{[VI]}Eu^{3+}$ = 0.947 Å), it is not surprising that the two can have different partition coefficients

65 between basalt and a crystallizing phase – making Eu and REE partitioning a potentially useful redox

66 sensor among magmatic systems.

67 The study of REE partitioning between co-existing phases has a long history within the petrology

68 community and arguably the best known or cited example relates to the reciprocal REE relationship

69 observed between the lunar highland crust and the mare basalt source regions (where the REE are

70 generally normalized to the chondritic uniform reservoir or CHUR). The average highland crust (Taylor et

71 al., 1973) shows the development of a pronounced positive Eu anomaly, while virtually all lunar mare

72 basalts have negative Eu anomalies (Taylor et al., 1973; Taylor, 1982). Pioneering work done by Philpotts

73 (1970) and later used by numerous authors (Drake, 1972, 1975; Drake and Weill, (1975; Grutzeck et al.,

4

74   1974; Watson and Green, 1981) used Sr as a proxy for Eu^{2+}. Use of this Sr-proxy made it possible to infer

75   the partitioning behavior of different Eu valence species (namely Eu^{2+} versus Eu^{3+}) between mineral-

76   basaltic melt pairs. Moreover, the use of the Sr-proxy permitted Eu partitioning to be evaluated against

77   the other monovalent REE at defined P-T-f_{O_2} conditions. This subsequently led to REE partitioning

78   studies involving plagioclase-basalt, diopside-basalt and apatite-basalt systems. Such studies,

79   particularly the work of Drake and co-workers (1972, 1975) confirm plagioclase is the dominant mineral

80   in basaltic systems in which Eu^{2+} is more compatible than Eu^{3+}. This led to plagioclase-rich rocks (e.g.,

81   lunar highland crust) with positive Eu anomalies, and whereas melt sources from which a significant

82   amount of plagioclase has separated (e.g., lunar mare basalt source/s) contained a pronounced

83   complementary negative Eu anomaly. More recent studies into the pyroxene-basalt system (Karner et

84   al., 2010) have provided an Eu^{2+}:Eu^{3+} XANES valence calibration for augite and a synthetic Martian

85   basalt, while the works of Trail et al. (2012) and Burnham and Berry (2012) have extended the use of Eu

86   valence calibrations to zircon (in these examples Eu/Eu* is used to measure intensity of a negative Eu

87   anomaly in zircon which varies systematically in response to the intrinsic oxygen fugacity).

88   The use of apatite as a redox sensor is highly advantageous because, like zircon, apatite saturation has

89   been shown to depend on key variables in silicate melts (e.g., P_2O_5, SiO_2 and temperature; Watson,

90   1979; Tollari et al., 2006). Partitioning data for the trivalent REE^{3+} (particularly La, Pr, Sm, Gd, Dy and Lu)

91   has also been constrained between apatite-silicate and apatite-carbonatite systems (Watson and Green,

92   1981; Klemme and Dalpé, 2003), providing a basic knowledge of the trivalent Onuma diagram for

93   apatite. It should also be noted that apatite, along with the merrillite-whitlockite group minerals, is also

94   known to represent a dominant REE host within lunar basalts (Jolliff et al., 1993), making it among the

95   most suited to REE valence-based studies in basalts from terrestrial planets. Apatite has also been

96   reported from a large range of rock types, of different ages, from many locations on the Moon (e.g.,

97   KREEP, mare basalt, anorthosites, etc), Mars and the eucrite parent body (i.e., Vesta), making any Eu

98   valence calibration of potentially broad application.

99   The last decade of research into lunar apatite has seen an intense focus on the OH-F-Cl content of the

100   mineral's column anion sites. Direct comparison to terrestrial apatite grains, for example, has led to

101   different hypotheses regarding the original volatile content of the Moon (McCubbin et al., 2010a, 2010b,

102   2011; Boyce et al., 2010; Greenwood et al., 2011; Tartèse et al., 2013). Notably, thermodynamic

103   considerations regarding the uptake of several volatile species into apatite have been linked to f_{O_2}

104   (Patino-Douce and Roden, 2006), and thus apatite volatile content models of the Moon would become

105   more complete with well constrained f_{O_2}s. For instance, the development of an independent f_{O_2} sensor

106   for apatite provides a direct evaluation of equilibria controlling uptake of volatiles into and the stability

107   of apatite. The development of an apatite redox sensor can also be directly compared to other methods

108   used to constrain f_{O_2} in various types of lunar magmas (Sato, 1976; Delano, 1990; Herd, 2008; Wadhwa,

109   2008), and as a means to cross check and evaluate redox preservation among different mineral phases

110   from the Moon. The use of REE as a redox sensor in apatite has the added advantage that, unlike other

111   elements/components found in apatite (e.g., OH, F, Cl, Sr, Pb, etc), the REE diffusivities in apatite are

112   among the slowest (Cherniak, 2000). This makes the REE among the more likely elements within the

113   mineral to preserve primary magmatic signatures (e.g., lunar basalts). It should also be noted the

114   calibration presented here can also be directly compared to results of the research of Konecke et al.

115   (2017, 2019) and Brounce et al. (2019) which uses $S^{6+}/\Sigma S$ in apatite as a means to determine oxygen

116   fugacity in silicate melts.

117

118   **Background information**

119   Use of the intensity of a negative Eu anomaly in apatite as a proxy for redox conditions [e.g., (f_{O_2})]

120   requires an understanding of Eu valence behavior in a basaltic (silicate) melt and the partitioning

121   behavior between a silicate liquid and a co-existing mineral phase (e.g., apatite). The europium valence

122   ratio within a silicate melt can be linked to f_{O_2} by the reaction:

123

124        $$EuO(melt) + \tfrac{1}{4}O_2 = EuO_{1.5}(melt) \qquad (eq.\ 1)$$

125

126   The equilibrium constant for the *Equation 1* reaction can be expressed as:

127

128        $$K = \frac{a^{melt}_{Eu^{3+}O_{1.5}}}{a^{melt}_{Eu^{2+}O_{1.0}} \cdot f_{O_2}^{1/4}} \qquad (eq.\ 2)$$

129   where, $a_{EuO_{1.5}}$ and a_{EuO} are the activities of $EuO_{1.5}$ (Eu^{3+}) and EuO (Eu^{2+}) in the melt. As the activity term

130   for a component is the product of the mole fraction and the activity coefficient, *Equation 2* can be

131   rearranged as:

132

133        $$\log K = \log \frac{X^{melt}_{Eu^{3+}O_{1.5}}}{X^{melt}_{Eu^{2+}O_{1.0}}} + \log \frac{\gamma^{melt}_{Eu^{3+}O_{1.5}}}{\gamma^{melt}_{Eu^{2+}O_{1.0}}} - \frac{1}{4}\log f_{O_2} \qquad (eq.\ 3)$$

134

135   where, X is the mole fraction and γ is the activity coefficient. Assuming Henrian behavior, which is

136   consistent with the low concentration of Eu within experiments/natural systems, the activity coefficients

137   can be considered constant. A modified equilibrium constant (K') for the silicate melt can be expressed

7

138   by rearranging *Equation 2* to give (Berry and O'Neill, 2004; Burnham and Berry, 2012; and Trail et al.,

139   2012):

140

141   $$\frac{Eu^{3+}}{\Sigma Eu} = 1/(1 + 10^{(-x\,\log f_{O_2}) + \log K'})$$ (*eq. 4*)

142

143   According to *Equation 4,* $Eu^{3+}/\sum Eu$ can be linked to $\log(f_{O_2})$ via a sigmoidal relationship, where "x" is

144   proportional to the number of electrons associated with the reaction. In this example the reaction

145   involves a single electron and thus the sigmoid "x" should approximate a value ~0.25 (as would be

146   predicted from *Equation 1*). For an apatite (or any mineral) coexisting with a silicate melt of mixed Eu

147   valence, $\log(f_{O_2})$ can be evaluated by way of apatite-melt Eu^{2+}-Eu^{3+} partitioning. In this study we use a

148   series of experiments (equilibrated at specific T-f_{O_2} conditions) to constrain the functional form

149   described in *Equation 4* by three different methods.

150

151   ***Crystal chemical controls on REE partitioning***

152   To appreciate how the redox calibrations relate to REE partitioning between apatite and melt, it is

153   important to understand the substitution mechanisms and potential crystallographic sites within the

154   apatite crystal structure that will influence REE partitioning. The structure of apatite (Fig. 1; modelled

155   after Hughes and Rakovan, 2015) can be described by the formula (Fleet and Pan, 2000):
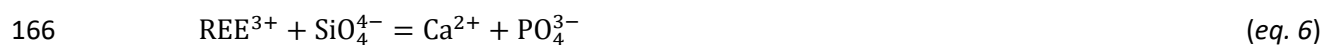
156

157   $^{[VI+III]}Ca(1)_4 {}^{[VII]}Ca(2)_6(PO_4)_6X_2$ (*eq. 5*)

8

158

159   Where the roman numeral (in closed brackets) refers to site coordination, Ca(1) and Ca(2) correspond to

160   specific calcium sites, and X refers to the column anion site (e.g., F⁻, Cl⁻, OH⁻, S²⁻). The substitution of REE

161   in apatite requires some knowledge of the potential REE^{3+} and Eu^{2+} substitution mechanisms observed in

162   apatite. Studies from natural and experimentally grown apatite demonstrate that numerous coupled

163   substitution mechanisms exist for the REE^{3+}, with the dominant substitution mechanisms including

164   (Hughes et al., 1991; Hughes and Rakovan, 2015):

165

166    $$REE^{3+} + SiO_4^{4-} = Ca^{2+} + PO_4^{3-}$$ (*eq. 6*)

167    $$REE^{3+} + M^+ = 2Ca^{2+}$$ (*eq. 7*)

168    $$REE^{3+} + X^{2-} = Ca^{2+} + F^-$$ (*eq. 8*)

169    $$2REE^{3+} + \square = 3Ca^{2+}$$ (*eq. 9*)

170

171   Where, M = monovalent cation (e.g., Na^+), X = divalent anion groups (e.g., SO_4^{2-}), and □= vacancy. The

172   substitution of Eu^{3+} and other REE^{3+} cations required to constrain Eu/Eu* (i.e., Sm^{3+} and Gd^{3+} for eq. 13

173   or La^{3+} through Lu^{3+} for eq. 14) likely requires some combination of one or more of the substitution

174   mechanisms described by eq. 6-9.

175

176   The substitution of Eu^{2+} is far simpler than the REE^{3+} cations and can be described as:

177

178    $$Eu^{2+} = Ca^{2+}$$ (*eq. 10*)

179

180   The REE^{3+} and Eu^{2+} site occupancy coupled substitution – and how they pertain to the redox calibrations

181   – is presented in the "Discussion" section of this manuscript.

182

183   **Method 1: XANES determination.**

184   The most direct measurement of $Eu^{3+}/\sum Eu$ (where $\sum Eu = Eu^{2+} + Eu^{3+}$) in apatite from experiments is

185   obtained by monitoring spectral features that are dependent on, and are proportional to, Eu valence.

186   Previous studies have used Eu L_3 X-ray absorption near edge structures (henceforth described as XANES)

187   to constrain Eu valence in silicate melts (Cicconi et al., 2012; Burnham et al., 2015), to constrain Eu

188   valence partitioning among a co-existing mineral and silicate melt (Karner et al., 2010; Shearer et al.,

189   2006), or to study Eu valence variation within an individual mineral (Rakovan et al., 2001). Previous

190   XANES studies by Konecke et al. (2017, 2019) and Brounce et al. (2019) on the sulfur K-edge

191   demonstrate the use of sulfur speciation in apatite as a viable redox sensor in magmatic systems,

192   making apatite the host of numerous, useful polyvalent elements. The use of Eu L_3 XANES spectra to

193   determine valence is based on the observation that the near-edge region shows notable white lines,

194   corresponding to a $2p_{3/2} \rightarrow 5d$ transition, that are sensitive to the relative abundance of Eu^{2+} and Eu^{3+}

195   components within the analytical volume. The Eu^{2+} compounds show a dominant Eu L_3 XANES white line

196   at ~6975.5 eV with a peak intensity at ~2 arbitrary units, while Eu^{3+} compounds show a dominant

197   whiteline at ~6983.3 eV with a peak intensity of ~3 arbitrary units. From an analytical perspective the

198   intense white line observed in the Eu L_3 XANES spectra is fortunate, as the different valence absorption

199   bands show significant energy separation (~7 eV) and make spectral deconvolution of different Eu

200   valence species straight-forward. This work employs direct and in-situ Eu L_3 XANES spectroscopy from

201   synthetic apatite and basalt equilibrated at controlled temperature-(f_{O_2}) conditions. Spectral analysis

202   from normalized XANES data, discussed further in the methods section of this paper, can be used to

203   define an $Eu^{3+}/\sum Eu$-f_{O_2} calibration for basaltic apatite applicable to natural apatite grains that

204   crystallize and equilibrate at temperatures equivalent to experiments presented here (e.g., 1110-1175

205   °C). The $Eu^{3+}/\sum Eu$ in apatite (co-existing with melt/glass) can be determined from the following

206   equation (noting that an arc tangent is also used to model the edge step):

207

208   $$\left(\frac{Eu^{3+}}{\sum Eu}\right)_{Apatite} = \frac{\varphi_{6983.3 \text{ eV}}}{(\varphi_{6983.3 \text{ eV}} + \varphi_{6975.5 \text{ eV}})}$$ (eq. 11)

209

210   where, φ_x corresponds to the amplitude or area under the gaussian curve at energy "x" eV (noting that

211   peak shape is unit normalized such that peak height and area are proportional). This method of

212   calculation can be applied without direct measurement of the co-existing glass, though it assumes

213   crystallization in a melt of similar composition at temperatures described in experiments. In an ideal

214   scenario analysis of both apatite and co-existing glass can be used to evaluate equilibrium.

215

216   **Method 2: Lattice strain calculation of (Eu/Eu*)$_D$.**

217   Where direct valence determination is not possible (i.e., XANES), Eu partitioning behavior can be

218   modeled against the partitioning of other trivalent rare earth elements present within experiments

219   (henceforth labeled REE^{3+}) - namely La, Ce, Sm, Gd and Lu. In the lattice strain technique, shown

220   graphically in Figure 2a, the REE^{3+}-based Onuma diagram from individual experiments can be used to

221   calculate a theoretical partition coefficient for Eu^{3+} ($D_{Eu^{3+}}^{Apatite/basalt}$). The intensity of a negative Eu

222   anomaly can be calculated from the difference between the measured Eu value from an experiment to

11

223   the estimated Eu^{3+} partition coefficient from a lattice strain model based on the REE^{3+} in apatite from

224   the same experiment [the intensity of this negative anomaly we henceforth label $(Eu/Eu^*)_D$].

225   The lattice strain model is defined as:

226

227    $$D_i = D_0 \cdot \exp\left[\frac{-4\pi E N_A \left[\frac{r_0}{2}(r_i - r_0)^2 + \frac{1}{3}(r_i - r_0)^3\right]}{RT}\right]$$ (eq. 12)

228

229   where, D_i = the partition coefficient for the element in question, D_0 = strain-free or ideal radius partition

230   coefficient for the cation site, E = Young's modulus, N_A = Avogadro's number, R = the universal gas

231   constant, r_i = ionic radius for the element in question (in the coordination of the site in question), r_0 =

232   ideal ionic radius for the cation site, and T = temperature (in K). The Eu/Eu* lattice strain model, labeled

233    $\left[\left(\frac{Eu}{Eu^*}\right)_D^{lattice\ strain}\right]$, of Brice (1975) and Blundy and Wood (1994) was previously used to calculate REE

234   partitioning between apatite-carbonatitic melt (Klemme and Dalpé, 2003) and was also used by

235   Burnham and Berry (2012) and Smythe and Brenan (2016) to calculate $Ce^{4+}/\sum Ce$ or Ce/Ce* (i.e.,

236   similar redox-dependent valence behavior among other REE) between zircon-silicate melt. The equation

237   used to describe the lattice strain calculated partitioning of Eu valence species is:

238

239    $$\left(\frac{Eu}{Eu^*}\right)_D^{lattice\ strain} = \frac{D_{Eu}^{Apatite/basalt}}{\left[D_{Eu^{3+}}^{\frac{Apatite}{basalt}}\right]_{lattice\ strain}}$$ (eq. 13)

240

241   **Method 3: $(Eu/Eu^*)_D$ calculated from neighboring Sm^{3+} and Gd^{3+}.**

242   The third calibration technique uses the intensity of the negative Eu anomaly (i.e., the negative

243   excursion of $D_{Eu}^{Apatite/basalt}$), relative to neighboring $D_{Sm}^{Apatite/basalt}$ and $D_{Gd}^{Apatite/basalt}$, determined by

244   measuring co-existing apatite and glass. The theoretical partition coefficient for Eu^{3+} ($D_{Eu^{3+}}^{apatite/melt}$) can

245   be calculated from $\sqrt{D_{Sm}^{Apatite/basalt} \times D_{Gd}^{Apatite/basalt}}$. A graphic describing this method (Figure 2b) is

246   henceforth labeled $\left[\left(\frac{Eu}{Eu*} \right)_D^{\sqrt{Sm \times Gd}} \right]$ and can be expressed:

247

248    $$\left[\left(\frac{Eu}{Eu*} \right)_D^{\sqrt{Sm \times Gd}} \right] = \frac{D_{Eu}^{Apatite/basalt}}{\sqrt{D_{Sm}^{Apatite/basalt} \times D_{Gd}^{Apatite/basalt}}}$$ (eq. 14)

249

250   It should be stressed that *Equations 13* and *14* are both examples where $(Eu/Eu*)_D$ can be considered a

251   proxy for $Eu^{3+}/\sum Eu$ in apatite. It is also worth noting that Methods 2 (*eq. 13*) and 3 (*eq. 14*), unlike

252   XANES methods, strictly requires analysis of both apatite and co-existing glass.

253

254   **Experimental methods**

255   The parameters required to ensure apatite saturation within a basaltic melt at 1 bar (e.g., synthetic

256   KREEP) have been previously evaluated (Watson, 1979; Tollari et al., 2006). Apatite crystallization from a

257   silicate melt may be characterized through system components, and these necessarily include a_{CaO}^{basalt},

258    $a_{P_2O_5}^{basalt}$, a_F^{basalt}, a_{Cl}^{basalt}, $a_{H_2O}^{basalt}$ and f_{O_2} – with each likely playing a role in apatite saturation. Experimental

259   results indicate that the three dominant components/variables related to apatite saturation include

260   P_2O_5 content (i.e., $a_{P_2O_5}^{basalt}$), SiO_2 content ($a_{SiO_2}^{basalt}$) and temperature (Watson, 1979; and Tollari et al., 2006).

261   The model of Watson (1979), for example, predicts a minimum P_2O_5 content of ~3.1 wt% to attain

262   apatite saturation for a synthetic KREEP 15386 basalt at 1150 °C (where bulk SiO_2 = 50.83 wt%; Rhodes

263   and Hubbard, 1973). In this manner it is possible to calculate the P_2O_5 content required for apatite

264   saturation in experiments at temperatures from 1110-1175 °C. For experiments containing ~50 wt% SiO_2

265   the melt will require approximately 3.1-3.5 wt% P_2O_5, and as indicated by Table 1 experimental starting

266   compositions are doped accordingly. While experiment temperatures are on the higher end of what

267   would be expected to crystallize apatite in a natural systems, we choose these temperatures to produce

268   crystals could be analyzable by XANES, with no or limited possibility of X-ray overlap/interaction with

269   the co-existing glass.

270

271   Experimental starting material (Table 1) was modeled after Apollo sample KREEP 15386,1 considered to

272   be an uncontaminated KREEP sample as interpreted from noble metal compositions (Warren et al.,

273   1978). KREEP represents an excellent target composition because the elevated REE makes it the most

274   suited for REE analysis, while the elevated P-content makes it the most likely system to saturate in

275   apatite along the liquid line of descent. A 4 gram starting mixture was synthesized by mechanical mixing

276   of high purity, reagent grade powders of SiO_2 (α-Aesar, 99.8 % purity), TiO_2 (α-Aesar, 99.9 %), Al_2O_3 (α-

277   Aesar, 99.98 % purity), FeO (α-Aesar, 99.5 % purity), $KAlSi_3O_8$ (α-Aesar), $NaAlSi_3O_8$ (α-Aesar), $Ca_3(PO_4)_2$ (α-

278   Aesar, >96.0 % purity), Mg_2SiO_4 (α-Aesar), $CaSiO_3$ (α-Aesar, 99.0 % purity), MgF_2 (α-Aesar, 99.99 %

279   purity), La_2O_3 (Spex), CeO_2 (Aldrich), Sm_2O_3 (REaction), Eu_2O_3 (REaction), Gd_2O_3 (REaction), Lu_2O_3 (Spex).

280   This starting material is henceforth labelled as "syn-KREEP 15386-01a" It is worth noting that the REE

281   starting mix is tailored to limit potential interferences in electron microprobe analysis, with a

282   La:Ce:Pr:Sm:Eu:Gd:Lu by weight of 1:2:1:1:8:1:1. It should also be stressed that the REE concentration of

283   the starting mix, ranging from 0.22-1.06 wt% REE^{3+}, is significantly higher than natural KREEP samples

14

284   but is sufficiently low to maintain undersaturation in phases like monazite, xenotime, etc (which are

285   never observed within experimental run products). Such a saturation would not invalidate the

286   experiment, but it would present an additional layer of complexity if Eu valence species and Sm-Eu-Gd

287   "group" elements were fractionated among three co-existing phosphate-rich phases (i.e., melt-apatite-

288   "REE phosphate").

289

290   Mixing of starting powders was carried out by grinding compounds under acetone within an agate

291   mortar-pestle for 20 minutes, and then mechanically agitating powder-bearing vials in a slowly-rotating

292   centrifuge at an orientation ~70 degrees to the rotational axis for a minimum of 3 hours. This process of

293   'grinding and mechanical agitation' was then repeated three times. The synthetic starting powder was

294   fired at 600 ˚C and then stored in a desiccator to ensure that the mixture remained nominally

295   anhydrous.

296

297   Experiments were carried out in an evacuated SiO_2 tube suspended from an Al_2O_3 rod by a Pt wire and

298   held within the hotspot of a 1 bar furnace. A control, type K, thermocouple was held immediately

299   adjacent to the experimental charge to ensure experiment temperatures are maintained to within ± 5 °C

300   (Figure 3). Two different experimental approaches were used. The first employed a double capsule

301   technique, where the buffer and experimental charge are separated by crushed SiO_2 chips. The second

302   experimental technique employed a participatory capsule (e.g., graphite or Mo metal or Fe metal),

303   where the capsule also represents a component of the oxygen buffer within the charge. The bulk of

304   experiments were carried out in AgPd capsules (14 experiments), with the exception of low f_{O_2} runs

305   ApREE-03b and ApREE-07b (Mo-MoO_2), ApREE-09 and ApREE-12 (graphite-CO-CO_2), and ApREE-06b (Fe-

306   FeO). As discussed in later sections of this manuscript, all low-f_{O_2} participatory capsules tend to result in

15

307   lower Fe glasses due to a combination of alloying with the capsule (Mo capsules) and/or saturation in

308   Fe-rich phases (e.g., olivine, schreibersite, etc). The exception to this is experiment ApREE-06b (Fe-FeO),

309   which saw considerable enrichment in Fe within the experimental glass (for this reason this experiment

310   was not included in XANES analysis). In all experiment types the top of the "syn-KREEP-15386-01a

311   bearing" capsule remained open within the evacuated silica tube. The experimental suite involved eight

312   different solid-state f_{O_2} buffers (Fe$_2$O$_3$-Fe$_3$O$_4$, Ni-NiO, SiO$_2$-Fe$_2$SiO$_4$-Fe$_3$O$_4$, W-WO$_2$, FeO-Fe$_3$O$_4$, Fe-FeO,

313   Mo-MoO$_2$, graphite-CO-CO$_2$) along with syn-KREEP 15386-01a basalts contained within either a noble

314   metal capsule (AgPd) or bored out apatite/graphite/Mo or Fe charge (gem quality Durango apatite

315   crystals or high purity rods). At completion, experiments were "drop quenched" in water to limit any

316   post-experiment (i.e., ΔT) crystallization within the charge. Assuming equilibrium, the buffer assemblage

317   will fix the oxygen fugacity so long as the buffer components exist within silica tube, and the individual

318   components are not modified by alloying or mixing with other experimental components (such that

319   activity remains constant). Upon quenching, experiments were mounted in standard 1" epoxy rounds

320   and polished to ¼ micron + colloidal silica for analysis. Subsequent optical and BSE imaging was used to

321   determine the phases present within the experimental charge and also to ensure the metal-metal oxide

322   buffer was not exhausted during the experiment (Figure 4). A detailed list of the oxygen fugacity buffer,

323   absolute fugacity, run duration, temperature and observed mineral assemblage for each experiment is

324   provided for the reader in Table 2.

325

326   **Analytical Techniques**

327

328   **Energy dispersive spectroscopy, back scattered electron and cathodoluminescence mapping.**

329   Energy dispersive spectroscopy and back scattered electron (BSE) imaging was performed on a Zeiss Evo

330   60 environmental SEM fitted with a LaB_6 crystal filament, housed at the American Museum of Natural

331   History. All imaging was carried out at 10 keV and 30 nA. Cathodoluminescence (CL) imaging was carried

332   out on a Gatan MonoCL attached to a Cameca sx100 electron microprobe, housed at the Rensselaer

333   Polytechnic Institute. Analysis involved an accelerating voltage of 15 kV and a beam current of 10 nA.

334   The CL images in Figure 5e-5f were obtained by combining spectra acquired through red (R), green (G)

335   and blue (B) filters in Digital Micrograph software with equal weighing.

336

337   **EPMA.**

338   Major and minor element concentrations of experimental glasses and mineral phases (e.g., apatite,

339   merrillite, plagioclase and pyroxene) were acquired on a Cameca sx100 electron microprobe housed at

340   the American Museum of Natural History. Analyses used a beam current ranging from 4-40 nA, an

341   accelerating voltage of 10-15 kV, and a ~1x1 μm focused beam. The analytical setup included 3 beam

342   conditions and involved a sweep of 18 elements. The first condition was at 10 kV and 4 nA, involved 10 s

343   counting times on F (LPC1) and Na (TAP) calibrated against MgF_2 and jade standards. It should be noted

344   that initial analyses (e.g., experiments ApREE-01 to ApREE-04) did not include fluorine in the analytical

345   routine. The second condition was at 15 keV and 20 nA, and involved counting times of 20-30 seconds

346   against standards of Ti, Mn, Ca, Mg, Al, P and K (calibration standards include rutile, rhodonite,

347   wollastonite, enstatite, K-feldspar and berlinite). The third condition was at 15 keV and 30-40 nA, and

348   involved counting times of 30 seconds for Si and 200 s for La, Ce, Sm, Eu, Gd and Lu calibrated against K-

349   feldspar, $LaPO_4$, $CePO_4$, $SmPO_4$, $EuPO_4$, $GdPO_4$ and $LuPO_4$. The same three-condition, focused beam

350   techniques were used for both mineral and glass analyses. Given the proximity of peak and background

351   positions for neighboring lanthanides, peak and background positions were first modeled in Virtual WDS

17

352   (Reed and Buckley, 1996) and were compared with full wavelength scans from experimental apatites

353   and REE phosphates standards on the LLIF spectrometer. The background peak positions (in $\sin\theta$) and

354   average detection limits are for La (-600,+800; 734 ppm), Ce (-660,+660; 729 ppm), Sm (-650,+650; 663

355   ppm), Eu (-560,+720; 680 ppm), Gd (-500,+600; 704 ppm), Lu (-415,+595; 1146 ppm). Supplementary

356   Material #1 provides details regarding the wavelength scans and peak/background positions used for

357   WDS analysis.

358

359   The EPMA protocol involved analysis of between 4-6 apatite grains per experiment, with transects

360   across individual crystals involving between 3-8 points, to evaluate the composition and variation among

361   apatite populations from individual experiments. Elements like Al, Si, Ti and K were used to monitor

362   signal contamination from glass or mineral inclusions within apatite. Durango and Wilberforce apatite

363   standards were analyzed across all EPMA sessions (8), with measurements on the standard being made

364   after approximately every 6 ApREE apatite analyses (i.e., every 1½ hours). This Durango data was used

365   to monitor any potential drift (none observed) and to evaluate accuracy of the REE data via comparison

366   with the standard geochemistry information by Marks et al. (2012). A comparison of standard data can

367   be found in Supplementary Material #3. Glass and apatite analyses from each experiment involved

368   measurements obtained from two different regions of the capsule, though some capsules (e.g., ApREE-

369   02a and ApREE-02b) have measurements from throughout the capsule (e.g., sequentially from four

370   regions parallel to the long axis of the capsule) to investigate heterogeneity. Analysis from other phases

371   from experiments (e.g., plagioclase, merrillite and pyroxene) are dependent on the size and distribution

372   within experimental charges, with thin plagioclase laths presenting a particular analytical challenge (e.g.,

373   plagioclase compositions are not reported from experiments where the phase is too small for

374   reliable/consistent analytical totals).

375

376   **LA-ICP-MS.**

377   While the bulk of the geochemical data in this study is based on EPMA and XANES analyses, we also

378   include LA-ICP-MS analyses from 4 representative experiments with f_{O_2} buffers that range from Fe_3O_4-

379   Fe_2O_3 to Mo-MoO$_2$ (ApREE-03a, ApREE-03b, ApREE-07, ApREE-09). This provides an independent

380   evaluation of statistical variations within experiments, while also representing a "quality control" check.

381   All LA-ICP-MS analyses were carried out on a Photon Machines 193 nm G2 laser systems equipped with

382   a HelEx 2-volume sample chamber connected to an Agilent 7900 quadrupole mass spectrometer

383   instrument at the University of Rochester. Analysis involved two laser footprints (or "spot sizes"), the

384   first involving a 3 μm spot for merrillite and apatite analysis and, the second involving a 20 μm circular

385   spot for glass analysis. These two analytical protocols employ a fluence of 4.72 J/cm^{2,} and a constant 7

386   Hz pulse rate over 16 seconds. At these conditions analysis involves a total of 105 laser pulses, with a 20

387   second pre-ablation background and a 30 second post-ablation background used in both types of

388   analysis. The He flow rate in the sample chamber was set to 0.6 L/min whereas the flow rate in the

389   HelEx arm was 0.2 L/min.

390

391   All analysis employed a mass sweep comprised of ^{23}Na, ^{24}Mg, ^{29}Si, ^{31}P, ^{43}Ca, ^{139}La, ^{140}Ce, ^{147}Sm, ^{153}Eu,

392   ^{157}Gd and ^{175}Lu. Several masses (e.g., those corresponding to Na, Mg, Si, P and Ca) are useful in terms of

393   resolving clean spectra, such that mass ratios in the time-resolved spectra can be used to identify when

394   apatite signal is contaminated by glass and vice versa. Given the small spot size, particularly during

395   apatite/merrillite analysis, the locus of the LA-ICP-MS analyte was also imaged in BSE to ensure ablation

396   pits are contained within the desired target material (see Fig. 5.g-5.h).

397

398   NIST612 was used as an internal standard for glass analyses, USGS standard AGV-1 was used as a

399   secondary standard. Silicon-29 was used as the internal standard for data reduction, as determined from

400   EPMA analysis. The American Museum of Natural History Durango apatite standard (#41651) was used

401   as the primary standard for apatite analysis (the same standard with detailed EPMA information

402   presented in Supplement 3), NIST612 was used as a secondary standard, and ^{43}Ca was used as an

403   internal standard. Glass standards NIST612 and AGV-1 were measured for every ten ApREE experimental

404   glass analyses, while Durango apatite and NIST612 was measured for every ten ApREE apatite/merrillite

405   analyses. All data reduction was carried out in Iolite 3.1 software with background fit with a spline

406   function (Paton et al., 2010, 2011).

407

408   **XANES.**

409   Eu L_3 edge XANES spectra was collected at Beamline 13-ID-C (GSECARS), at the 7 GeV Advanced Photon

410   Source, Argonne National Laboratory (IL, USA). Analyses of Eu-standards were collected on synthetic

411   powders mounted in thin film in Kapton tape and measured in transmission mode. These standards are

412   of known valence and include $Eu^{2+}TiO_3$, $Eu_2^{3+}O_3$, $Eu^{3+}PO_4$, $Eu^{3+}Cl_3$ and $Eu^{3+}(NO_3)_3 \cdot 5H_2O$ (Fig. 6.1c).

413   Spectral analyses of ApREE experiments (Fig. 6.1a-b), by contrast, were carried out from focused

414   fluorescence measurements made in-situ on the same 1" epoxy mounts used in EPMA. All XANES

415   measurements were made prior to EPMA (and LA-ICP-MS analyses) to limit any potential damage to the

416   apatite prior to X-ray measurements. Here it should also be pointed out that no common apatite grains

417   from an individual experiment were analyzed across analytical methods – this was done to limit any

418   potential damage across techniques.

419

420   The incident photon energy was selected via a cryogenically-cooled Si-(111) double crystal

421   monochromator and the energy resolution for measurements made at the Eu K-edge is ~0.5 eV. Energy

422   calibration of the monochromator was carried out on the V K-edge and by defining the first derivative

423   peak observed in a V metal foil spectrum at 5465 eV. The beam was located and focused to a 2 x 2 μm

424   spot using Kirkpatrick-Baez (KB) mirrors by imaging on a Ce-doped YAG phosphor. The critical angle cut-

425   offs of the mirrors on the instruments provided excellent rejection of high energy harmonics. Absorption

426   spectra were recorded from 6897-7115 eV, with steps of 5 (<6962 eV), 0.5 (6962-7007 eV), and ~3 eV

427   (7007-7115 eV). Fluorescence was recorded at 45° to the sample and perpendicular to the incident X-ray

428   beam using simultaneous counting and equal weighing on four Vortex-EX silicon drift detectors (SII

429   NanoTechnology Inc.) with digital signal processing electronics from which the Eu L_3 integrated intensity

430   was extracted and recorded digitally. At the concentrations observed in both glass and apatite, reported

431   analyses represent single points acquired using 3 second counting periods for a total analytical window

432   of just under 7 minutes. Visual inspection and BSE observations made from both glass and apatite

433   regions of analyses show no evidence for beam damage. Similar to 1 atmosphere experiments in mafic

434   glasses carried out by Burnham and Berry on the Ce L_3-edge (2014), this study did not see beam-induced

435   changes in fluorescence intensity. This is supported by repeat analyses on common apatite crystals

436   during rotation analyses, which saw no indication of fluorescence intensity change across the trio of

437   measurements, nor any significant variation observed in the relative intensity of the Eu^{2+} and Eu^{3+} peaks

438   (outside of that corresponding to mineral anisotropy).

439

440   The REE-doped minerals (apatite and merrillite) show excellent luminescence under the X-ray beam,

441   with merrillite luminescing in red and apatite in purple to blue colors. This optical luminescence makes it

442 possible to actively image the footprint of the beam in real-time and identify regions within the

443 experiment that are best suited to either mineral or glass analysis (see Fig. 7). Rapid "flyscan" X-ray

444 fluorescence mapping of a region of interest (ROI) immediately surrounding a target

445 apatite/merrillite/glass material (typically involving energies corresponding to Eu L-α line, Ca K-α line

446 and Ti K-α line), in addition to optical luminsescence, provides an additional check for locating

447 mineral/melt regions most suited to analysis. These flyscan maps employed a 7.1 keV incident X-ray

448 energy, with a 45 ms/pixel dwell time and a ROI defined by the target crystal.

449

450 Aside from direct imaging of the X-ray path, the photon cross section for apatite can be calculated in

451 Hephaestus (version 0.9.13). At the Eu L_3 edge (6977 eV) and at the average density of apatite (3.17

452 g/cm^3) a single absorption length is 24.7 μm (though the majority of fluorescence X-rays recorded by the

453 detector likely source from the near-surface environment) and as a general practice only grains that

454 exceed twice this length were targeted (i.e., grains with a diameter ≥50 μm).

455

456 Two analytical approaches, employing the described analytical setup, were used. The first involved

457 analysis of randomly oriented apatite grains from throughout the experimental charge to evaluate the

458 statistical variation within the experiment (Fig. 6.2c). Spectra using this approach were recorded from 28

459 synthetic apatite crystals from 9 experiments, 6 synthetic merrillite crystal from 1 experiment, and 20

460 glass analyses from 9 experiments. Efforts were made to analyze synthetic plagioclase crystals from

461 several experiments (notably ApREE-07 runs at HM and MMO) but the fine-grained plagioclase laths and

462 the long absorption length at 6977 eV (24.6 μm) give rise to inconsistent results due to signal

463 contamination from other co-existing phases.

464

465   The second approach involved orientation scans (relative to a reference or "north position" on the

466   epoxy mount), with scans conducted at 0°, 60° and 120° at a common point from four different grains

467   within a given experiment. To accurately record the same position a rapid "flyscan" X-ray fluorescence

468   mapping technique was used. This was done by identifying four target grains within an experiment at

469   the 0° reference orientation, then linearly combining X-ray fluorescence maps with the Ti Kα, Ca Kα and

470   Eu Lα lines. These three fluorescence lines can be combined to produce an RGB image that makes it

471   possible to identify and distinguish regions of glass/apatite suitable for analysis while also helping target

472   specific crystal (i.e., by visually confirming X-ray maps reproduce key features when rotated by a 60°

473   interval). In Fig. 6.2, glass regions are generally represented by light blue hues while apatite grains are

474   represented by red-pinkish hues. Analysis involving this approach includes 24 spectra, from 8 apatite

475   grains from 2 experiments. Once the initial fluorescence analyses are complete, the sample is then

476   rotated to a 60° rotation and remapped in Ti-Ca-Eu space. The reference map and rotated map are

477   directly compared (visually inspected) to ensure the same common grains and points are analyzed. Then

478   fluorescence analyses are again carried out, though the new scans are at a 60° rotation to the original

479   reference. Finally, the sample is rotated a further 60° (now 120° from the original orientation) and

480   measured a final time.

481

482   The basic principle behind the two described techniques is that the first (analyses at multiple locations

483   within an experimental charge) provides a snapshot of variation observed within a given phase within a

484   given experiment, while the second (oriented scans) provides some quantitative estimate of anisotropy

485   controls on the Eu L_3 XANES spectra in said phases. In reality, the two techniques provide

486   complementary information and should be evaluated as a whole, because they represent analyses from

23

487   a common experiment, but it does represent an important control on factors contributing calibration

488   and analytical uncertainty.

489

490   Spectra normalization was performed with Athena software (version 0.9.25, Ravel and Newville, 2005)

491   using the same set of normalization parameters from all spectra. Background subtraction over the pre-

492   edge energy range employed a linear regression with clamps at 6915 and 6950 eV. The post-edge region

493   involved regression with a quadratic polynomial with clamps at 7040 and 7175 eV. Visual inspection of

494   the pre-edge and post-edge lines ensured that the energy range (or input parameters in Athena) of pre-

495   edge and post-edge lines were optimal for normalization (i.e., to check whether the post-edge was

496   affected by other absorption lines).

497

498   As indicated in Fig 6.1d, Eu^{2+}:Eu^{3+} or Eu^{3+}/ΣEu were calculated using the 'peak fitting' function in Athena

499   (Ravel and Newville, 2005) with the peak positions (energies) for spectral components fixed across all

500   experiments. These fits involved gaussian curves centered to absorption features at 6983.3 eV (Eu^{3+}) and

501   6975.5 eV (Eu^{2+}), with an arc tangent centered at 6983.8 eV (used to model the energy step), with the

502   overall fitting region including 81 individual data points over a 45 eV energy range (6962-7007 eV).

503   Analyses involved up to 6 measurements from individual apatite grains at random orientation and/or

504   glass domains within the capsule, and error was calculated from the standard deviation across all

505   measurements from an individual experiment. The orientation effect on spectra was not confirmed via

506   individual grain rotations, but crystal habit does permit an evaluation of differences in Eu^{3+}/ΣEu for

507   measurements carried out perpendicular versus parallel to the apatite c-axis (see Fig. 7a and Fig. 7b).

508

24

509   **Results**

510   **Experimental run products.**

511   Experimental run products are listed in Table 2, while representative BSE/CL photomicrographs are

512   shown in Figure 5 and phase compositions are reported in Table 3 and Supplement 1. As indicated by

513   these tables and figures, all experiments are apatite-saturated, such that it is possible to calculate

514   apatite-melt partition coefficients for the REE. Apatite is euhedral in all experiments except one, with

515   the hexagonal dipyramids clearly observed from crystal habit in all studied f_{O_2} conditions (see Fig. 5 or

516   Fig. 6.2) and as shown in Supplement 1 is restricted to compositions close to end-member fluorapatite.

517   The only exception is experiment ApREE-01b, which employs a participatory apatite capsule, where the

518   observed apatite crystals show irregular and rounded crystal habits. The apatite grains from ApREE-01b

519   also display observable zonation in CL (Fig 5.i, ApREE-01b), where dull BSE cores correspond to "seeds"

520   from the Durango apatite capsule and bright rims correspond to new apatite growth.

521

522   In addition to apatite, phases present within experiments comprise variable mixtures of plagioclase and

523   pyroxene, which become increasingly abundant in lower temperature experiments. The mineralogy and

524   crystallization sequence observed in these experiments broadly match phase equilibria for a Ca-rich

525   starting material reported from the experimental work of Walker et al. (1973), where apatite and

526   plagioclase crystallization occur with decreasing temperature until the plagioclase-pyroxene cotectic is

527   intercepted. Merrillite is also present in some experiments and is generally restricted to high

528   temperature and high oxygen fugacity experiments (e.g., > 1150 °C and f_{O_2}>NNO).

529

530   The glass composition from experiments can generally be described as basaltic to picritic basalt, though

531   low SiO_2 observed in experiments is the result of elevated P_2O_5 required for apatite saturation

532   (Supplement 1). With progressive crystallization for the lower T set of experiments, and saturation of

533   different phases with changing f_{O_2} (namely schreibersite), melt composition can vary from experiment

534   to experiment. Most importantly, and as also observed in the experiments reported by Drake (1972), the

535   Fe content of experimental glass decreases with decreasing $\log(f_{O_2})$. This is particularly true for

536   experiments equilibrated at $\log(f_{O_2})<-12$, where schreibersite saturation is achieved. It should also be

537   noted that the metal-metal oxide solid state buffer can also influence glass/melt composition within

538   experiments, as these components must attain some vapor pressure within the charge that enables

539   chemical communication.

540

541   **Cathodoluminescence.**

542   The CL intensity has been demonstrably linked to REE concentration – specifically and Gd^{3+}, Ce^{3+} and

543   Sm^{3+} – and so it is not surprising that apatite, merrillite and plagioclase all activate under the electron

544   and X-ray beam (Mariano and Ring, 1975; Roeder et al., 1987; Barbar and Pagel, 2001). This

545   luminescence makes it possible to visually target glass domains that are free of small crystalline

546   material. Many of the dominant phases present in the experimental charge luminesce at different

547   wavelengths – e.g., apatite crystals are often seen as "red" while plagioclase commonly displays a "blue"

548   luminescence – making it possible to distinguish regions within an experiment where two or more

549   phases may be intergrown (Fig. 5.e-f).

550

551   **EPMA data.**

26

552   Average and 1σ (in wt% oxide) for experimental run products, including apatite, glass and some

553   additional run products are presented in Supplement 1. The REE concentrations in experiment ApREE-

554   01b (particularly La and Ce) are significantly different from "unseeded" experiments, suggesting that

555   analytical totals are unreliable due to contamination from Durango apatite seeds in this experiment.

556   Partitioning data from ApREE-01b is, therefore, not considered further. Faint sector zoning is also noted

557   from some experiments (Fig 5.i, ApREE-12; WM), but this variation is not accompanied by any

558   detectable multimodality in minor or trace element data distribution (see Fig. 9 and discussion section

559   "An evaluation of data…"). No inter-grain variation is observed in REE concentration within individual

560   experiments, such that there appears to be no zonation depending on capsule position or crystal size.

561

562   Three experiments from this study (ApREE-01a, ApREE-03a, ApREE-04) contain large, euhedral RE-

563   merrillite (where RE indicates the phase is 'Rare Earth' rich) crystals. These crystals are often also called

564   whitlockite (or whitlockite group under Dana classification) and are members of a mineral group that

565   show some multiplicity among the different cation sites. Given that the experimental starting material

566   was designed to be anhydrous and EPMA analytical totals are ~100 % (Table 3; 100.55 ± 2.03, 99.98 ±

567   1.18), we conclude that these phosphates are members of the ~OH-free Merrillite family (e.g., Hughes

568   et al., 2006; Jolliff et al., 2006). As shown in Figure 5a, the merrillite crystals show much higher BSE

569   intensity relative to apatite, which is a good indication of the higher REE content of merrillite. The

570   merrillite compositions reported from experiments are presented in Table 3 and generally show REE

571   concentrations that are >1 wt% $\sum REE$ (in wt% oxide), thus making the phase the dominant REE host

572   within experiments. The calculated mineral compositions, based on 56 oxygens, is

573      $Ca_{16.8}REE_{1.5}(Mg,Fe)_{2.0}P_{13.7}Si_{0.2}O_{56}$ for ApREE-01a and $Ca_{16.5}REE_{1.6}(Mg,Fe)_{2.2}P_{13.7}Si_{0.6}O_{56}$ for ApREE-04 – thus

574   confirming saturation in an RE-Merrillite phase in experiments ApREE-01a, ApREE-03a and ApREE-04.

575

576   In addition to apatite, merrillite and glass analyses, attempts were made to obtain measurements from

577   plagioclase and/or pyroxenes observed in experiments, but the REE concentrations were too low to be

578   measured by EPMA (with the exception of experiments ApREE-01a, ApREE-02a, ApREE-04 and ApREE-

579   15X, where attempted plagioclase/pyroxene analysis are included in Table 5). Reliable plagioclase

580   analysis is a particular problem, as the fine-grained nature of laths makes it difficult to isolate an

581   analytical volume suitable for EPMA. It is worth noting that experiments ApREE-15X and ApREE-02x do

582   show large Eu concentrations, while all other REE exist at concentrations below the detection limit. In

583   other words, these experiments likely record a negative anomaly in apatite and have plagioclase with an

584   associated positive anomaly.

585   **LA-ICP-MS.**

586   Average and 1σ (in wt% oxide) for experimental run products obtained from LA-ICP-MS analysis of a

587   representative group of experiments, including values for apatite, glass and RE-merrillite are also

588   presented in Supplement 2 (bottom). A representative apatite LA-ICP-MS spectra shows down hole

589   decreases in counts typical of our analytical session (Figure 8). Such data correspond to near-surface

590   BSE image laser ablation spots (e.g., Fig. 5.g-h), which show the dimension of the laser pit and the target

591   phase. Collectively these two observations provide strong evidence analyses are clean.

592

593   Individual analyses of REE concentrations of glass and apatite are remarkably similar to those reported

594   from EPMA, and generally range from 950-13,000 ppm (by weight). While glass analyses from LA-ICP-MS

595   have a much smaller error than EPMA measurements, apatite analyses across the two techniques are

596   remarkably consistent (see Fig. 17). Here it is important to stress that LA-ICP-MS analyses are included

28

597 from experiments at both high (i.e., hematite-magnetite buffer) and low f_{O_2} conditions (i.e., graphite-

598 CO-CO_2 or Mo-MoO_2 buffer) in this dataset – including experiments ApREE-03a, ApREE-03b, ApREE-07,

599 ApREE-09, such that a full range of potential $Eu^{3+}/\Sigma Eu$ can be evaluated across both datasets.

600

601 **XANES data.**

602 Standard Eu compounds used in this study (Figure 6.1c) demonstrate that Eu^{2+}-compounds record a

603 dominant Eu L_3 XANES feature (or whiteline) at 6975.5 eV, while Eu^{3+}-compounds record a dominant

604 XANES feature at 6983.3 eV (note: XANES standard data can be made available by contacting the

605 author). Data from spectral fits on apatite and glass (average and 1σ) from a select number of individual

606 experiments are reported in Table 6, while representative spectra from both apatite and glass are

607 shown in Fig. 6.1a-b.

608

609 As described in the methods, XANES data can be separated into two groups, where the first is used to

610 provide a statistical snapshot of variation within an experiment through a data comparison of

611 measurements collected at multiple locations within the experimental charge. The other group is used

612 to investigate orientations effects (i.e., oriented XANES scans).

613

614 The first method (analyses throughout the charge involving randomly oriented apatite grains) show that

615 variations in $Eu^{3+}/\Sigma Eu$ are generally small in glass analyses (with σ varying from 0.0008-0.006 or 0.008-

616 1.72 %). Apatite analyses show higher standard deviations than glass, an observation consistent with the

617 EPMA and LA-ICP-MS results, and is likely related to the combined effect of anisotropy (a concern for

29

618   both EPMA and XANES but not LA-ICP-MS) and intrinsic variation within apatite. The largest inter-grain

619   variation in XANES analysis is observed within the most reduced experiments where the Eu^{2+} content

620   reaches significant proportions (i.e., >13 %) – most notably among experiments ApREE-07 (Mo-MoO$_2$

621   buffer), ApREE-09 (C-CO-CO$_2$ buffer) and ApREE-15X (IW buffer) – where σ for $Eu^{3+}/\sum Eu$ are 2.75, 9.29

622   and 5.67 % respectively. It is possible that some of this variation relates to crystallographic orientation

623   effects on the in-situ XANES method (a condition that would extend to calibration applications), but such

624   variations only appear to influence the estimated totals by ~2-10 %.

625

626   The second analytical technique involves oriented analyses from four apatite grains from representative

627   experiments, rotated at three 60° orientations. The observed orientation-dependent variation in

628   calculated $Eu^{3+}/\Sigma Eu$ in repeat apatite analyses from experiment ApREE-02 ranges from 1.3-7.2 %, while

629   experiment ApREE-12 ranges from 3.0-7.9 %. Here it is worth noting that oriented analyses show

630   remarkably similar $Eu^{3+}/\Sigma Eu$ variation to that measured from numerous randomly oriented apatite

631   grains described in XANES methodology 1. It is also worth highlighting that ApREE-12 (C-CO-CO$_2$) and

632   ApREE-02b (IW) represent examples where both Eu^{2+} and Eu^{3+} spectral features are abundant (i.e., the

633   samples contain a mixture of Eu valence species), such that potential orientation-dependent spectral

634   variation is maximized. In other words, if the maximum variation in orientation-dependent calculated

635    $Eu^{3+}/\Sigma Eu$ is observed in the relative peak heights at $\varphi_{6975.5}$ and $\varphi_{6983.3}$, then by definition the largest

636   variation must be observed at the inflection point of the valence speciation sigmoid curve. This variation

637   will likely decrease systematically as one valence species (and one spectral feature) begins to dominate

638   the system. The average, maximum observed orientation-dependent variation observed in all oriented

639   samples is 4.8 ± 2.2 %, indicating that while apatite anisotropy can result in subtle changes to

640     $\varphi_{6975.5}:\varphi_{6983.3}$ in the Eu L_3 XANES features, the influence of this effect can be measured and calculated

641   using synchrotron-based techniques.

642

643   **Discussion**

644   **Experimental products.**

645   Run products from experiments include phases that would be predicted from a Ca-rich KREEPy starting

646   mix (equilibrated at 1 bar) at temperatures ranging from 1110 to 1175 °C. All experiments are saturated

647   in apatite, with melts at lower temperature generally showing an increasing abundance of plagioclase

648   and pyroxene. It should be noted that the crystallization of schreibersite at low f_{O_2} does complicate use

649   of the crystallization sequence in some experiments. It is also worth noting that many experiments here

650   contain vapor bubbles, indicating the presence of one or more volatile species within the experimental

651   charge. The simplest explanation is that volatile components within experiments attain a vapor pressure

652   at experimental conditions (namely things like Na, F, K, P, CO and CO_2). The alternative interpretation

653   relates to experiments employing a rapid, drop quench into water that ensures the sample is quenched

654   in ~1 second (thus locking in experimental fugacity and temperature). It is possible some H_2O is trapped

655   within glasses in this manner. The important thing here to note is that (i) analytical totals approximate

656   100 % and indicate a syn-KREEP experimental glasses are anhydrous glass; (ii) if any water is present in

657   experiments, volume expansion is likely to break the silica ampoule as the capsule is added to the

658   furnace (making H_2O unlikely to be in any experiment), and (iii) even if minor amounts of water are

659   contained within experiments it has previously been shown H_2O content has negligible influence on REE

660   partitioning into apatite (Watson and Green, 1981).

661

662   **An evaluation of EPMA data robustness and analytical considerations**

663   Accurate analysis of apatite via EPMA has been studied by numerous authors, including Jim Webster and

664   his research group (to whom this special volume is dedicated - see Goldoff et al., 2012). The work by

665   Laputina et al. (1999), Reed and Buckley (1998), Marks et al. (2012) and Henderson (2011) collectively

666   demonstrate the use of the electron microprobe for the study of major, minor and trace elements in

667   natural apatite – most notably the REEs – is possible when done properly and where concentration/s

668   permit. This requires analytical protocols that take specific note of beam setup, orientation affects,

669   background positions, potential overlap corrections and the use of appropriate standards. Interested

670   readers are strongly encouraged to explore Supplementary Material #3 and #5 section of this paper for

671   further information. Here it is important to acknowledge previous studies into REE partitioning, most

672   notably those involving the study of lunar phosphates (i.e., apatite, RE-merrillite) have largely required

673   ion microprobe techniques (including, but not limited to, the works of Jolliff et al., 1993; Shearer et al.,

674   2011; Robinson et al., 2017). This is due to a combination of factors, including low concentration (i.e.,

675   ppm or lower concentrations), potential matrix mismatch between standards and unknowns (i.e., the

676   use of REEs in glasses versus REE-phosphates), and X-ray peak overlap issues among the various REE.

677   Among the REE, some elements have historically proven more truculent than others during analysis of

678   lunar phosphates, with the elements generally falling in two categories: (i) those deemed "hard to

679   measure" group; and (ii) those deemed "less difficult to measure". The "hard to measure" group of REEs

680   typically includes odd-# RE elements and the HREE (the latter largely pertaining to the LEE:HREE slope of

681   the parent melt) and typically includes elements like Lu, Yb, Tm, Ho, Tb, Eu, Pr (Lindstrom et al., 1985,

682   1991; Shervais et al., 1984; James et al., 1987; Jolliff et al., 1993). The "less difficult to measure" group

683   includes elements somewhat easier to measure by more conventional trace-/minor-element analytical

684   techniques - such as ion microprobe, mass spectrometer or EPMA (this group typically involves the

685   even-# RE elements and the light REE) and usually includes Y, La, Ce, Nd and Gd (Albee and Chodos,

686   1970; Keil et al., 1971; Gancarz et al., 1971; Griffin et al., 1972; Brown et al., 1971, 1972; Jolliff et al.,

687   1993). What is important to note here is the various issues that make lunar apatite analysis difficult (as

688   listed above), can and have all been almost entirely avoided in this study by deliberately doping

689   experiments at elevated concentrations. This is to say experiments contain thousands of ppm of select

690   REE while (rather than many of the REE existing at ppm or ppb in natural silicate-phosphate systems),

691   while also avoiding the odd-even effect. The experimental approach also has the advantage that

692   elevated REE concentration is kept specifically low (such that partitioning remains Henrian) ensuring

693   primary REE-bearing phase/s saturation (like monazite or xenotime) is not achieved.

694

695   Here it should also be stressed that experiments presented here are deliberately designed to avoid REEs

696   that cause potential WDS overlaps that will influence either the lattice parabola or Sm:Eu:Gd (in either

697   peak or background position), with the highest overlap correction calculated in VirtualWDS software

698   (Reed and Buckley; 1998) from any apatite/glass/merrillite measurement made in this study is 0.00008

699   % (a correction on Ce concentration when WDS is carried out against $L\alpha_1$ peak; see Supplementary

700   Material #3). Here we should also stress to the reader that while application of the various calibrations

701   presented this study can be conducted by EPMA and LA-ICP-MS, application to natural samples (lunar,

702   martian or terrestrial) will likely require the use of an ion microprobe or mass spectrometer.

703

704   It is important emphasize the manner in which errors are calculated, as this will explain why the error

705   bars associated with $\left[\left(\frac{Eu}{Eu^*}\right)_D^{\text{lattice strain}}\right]$ are larger than those of $\left(\frac{Eu}{Eu^*}\right)_D^{\sqrt{Sm \times Gd}}$. As an example, the error

706   bars for individual data points from the apatite and silicate glass from ApREE-03b (at Mo-MoO$_2$

707   equilibrium – i.e., mixed valence with a clear negative Eu anomaly) represent the standard deviation

33

708   derived from the EPMA counting statistics (glass: Fig. 14a apatite: Fig. 14b). Note that the individual

709   REE_2O_3 concentrations of apatite and glass reflect the La:Ce:Sm:Eu:Gd:Lu (1:2:1:1:8:1:1) of the

710   experiment. This odd REE shape necessitates that it is highly unlikely to replicate a lattice strain parabola

711   by analytical artifacts, rather it is only possible through the combined clean analysis of both apatite and

712   glass.

713

714   As shown in Fig. 14c the $D_{REE}^{Apatite/baslt}$ an individual apatite within experiment ApREE-03b can

715   collectively shift up or down in Sm, Eu and Gd partitioning space. This collective shift results in an

716    $\left(\frac{Eu}{Eu*}\right)_D^{\sqrt{Sm \times Gd}}$ that remains relatively consistent from grain to grain (or analysis to analysis), while the

717   concentration-based variation in absolute partition coefficients may vary for individual REE. If we take 8

718   apatite-glass pairs from representative ApREE-03b experiment, and propagate through Sm, Eu and Gd

719   across all the apatite and glass data we get a $\left(\frac{Eu}{Eu*}\right)_D^{\sqrt{Sm \times Gd}}$ = 0.74±0.06 (noting these are the values

720   reported in Supplement 2 and Fig. 17-18). If we simply take the $\left(\frac{Eu}{Eu*}\right)_D^{\sqrt{Sm \times Gd}}$ from the 8 apatite-glass

721   pairs and look at the variation amongst that population (rather than propagating error through Sm, Eu

722   and Gd across all apatite and glass analyses), then $\left(\frac{Eu}{Eu*}\right)_D^{\sqrt{Sm \times Gd}}$ =0.74±0.04 (i.e., there is a near halving

723   in the reported error).Here it is worth noting that propagating the error for $\left[\left(\frac{Eu}{Eu*}\right)_D^{lattice\ strain}\right]$ uses all 6

724   REE elements described from our ApREE experiments (La, Ce, Sm, Eu, Gd and Lu) in both apatite and

725   glass, thus leading to larger error bars when $\left(\frac{Eu}{Eu*}\right)_D^{\sqrt{Sm \times Gd}}$ and $\left[\left(\frac{Eu}{Eu*}\right)_D^{lattice\ strain}\right]$ are directly compared.

726   While we see merit in using either mechanism for reporting error – the first involving error propagation,

727   the second involving inter-grain variation in Eu/Eu* without propagating through Sm and Gd) – we have

728   decided to use the former throughout this manuscript.

729

730   **Comparison of EPMA and LA-ICP-MS datasets and analytical uncertainty.**

731   To assess the quality of the EPMA data from a specific set of experiments presented in this study (as an

732   example), we first take ApREE-06 (buffered at the QFM equilibrium) and observe the statistical variation

733   within the REE measurements (Fig. 9.a). If the 34 individual apatite analyses (generally core to rim

734   transects) from 4 apatite crystals are considered we can first note several key observations: (a) all

735   elements show a normal distribution about the mean (see Fig. 9.a; reported in wt% RE_2O_3); (b) all the

736   REEs doped in the experiment are all well above detection limits (see $EPMA_{Gd_2O_3}^{LOD.}$ and $EPMA_{Smd_2O_3}^{LOD.}$ in

737   Fig. 9.b for an example); (c) analytical uncertainty of EPMA analyses ($EPMA_\delta$) is comparable to the

738   intrinsic experimental inter-grain variation (Exp_δ). To emphasize this, Fig. 9.b shows direct comparison of

739   all data from the same analyses (ApREE-06) where we report the analytical uncertainty ($EPMA_\delta$; light

740   error bars) based on spectrometer counting statistics, while inter-grain variation based on analyses from

741   throughout the experiment and the same data reported in Supplement 1 is shown Fig 9.b (Exp_δ; heavy

742   error bars and large circles).

743

744   Both EPMA and LA-ICP-MS analyses have been conducted and compared for ApREE-03b, buffered at

745   Mo-MoO_2 equilibrium (Fig. 9.c-9.d). Firstly, the instrumental and inter-grain variation is similar to our

746   previous example (ApREE-06) and is again well above detection limit. It can also be seen that despite

747   different counting statistics (signal/noise) across the two analytical techniques, apatite analytical

748   uncertainty (see Fig. 9.c or $EPMA_\delta$ and LA-ICP-MS_δ) is remarkably consistent across the two techniques.

35

749   Similarly, as shown in Fig. 9.d, the inter-grain uncertainty (Exp$_\delta$) is also remarkably similar. In other

750   words, the inter-grain variation, particularly the inter-grain variation within the apatite population from

751   a given experiment, does not depend on the analytical technique. The similar inter-grain variation

752   between the two techniques demonstrates the reported error is related to intrinsic experimental

753   variation (i.e., Exp$_\delta$) and as such the calibration curves presented in Fig. 17-18 will not be dramatically

754   improved by using techniques with superior counting techniques. Here it also be noted that while glass

755   analysis (in terms of error) is vastly improved by employment of LA-ICP-MS, apatite analyses is not. In

756   this regard, most of the error of the provided calibrations presented in *Equations 17* and *18* (in terms of

757   both [Eu/Eu*]$_{Sm-Gd}$ or [Eu/Eu*]$_{lattice}$) will unlikely be improved greatly by employing other techniques

758   capable of obtaining better counting statistics. (e.g., ion microprobe).

759

760   Given this research is dependent on accurately determining the relative concentration of specific REE –

761   namely La, Ce, Sm, Eu, Gd and Lu – we present numerous checks in supplementary material in order to

762   provide a rigorous evaluation of data quality (including full wavelength scans of standards, potential

763   overlap calculations/corrections, detection limits, etc). The greatest check in this study is to directly

764   compare results from EPMA and LA-ICP-MS analyses on common experiments (see Tables 4, 4a and Fig.

765   17). The strong positive correlation between the two techniques provide internally consistent partition

766   coefficients and thus calculated Eu anomalies (Fig. 17.c and 17.d).

767

768   If we take the average detection limit across all EPMA analyses (La = 734 ppm, Ce = 729 ppm, Sm = 663

769   ppm, Eu = 680 ppm, Gd = 704 ppm, Lu = 1146 ppm) and compare these values directly to LA-ICP-MS

770   from experiment ApREE-07 (La = 0.03 ppm, Ce = 0.03 ppm, Sm = 0.14 ppm , Eu = 0.04 ppm, Gd = 0.15

771   ppm, and Lu = 0.03 ppm; noting all LA-ICP-MS record similar detection limit values), clearly the LA-ICP-

772   MS has lower detection limits. Even so, the measured concentrations reported in Supplement 1a and

773   Supplement 1b are well above these reported detection limits for EPMA. With this in mind, evaluation of

774   the standard deviation (δ) across the two dataset shows remarkable similarity (Tables 4a,b Fig. 17). As

775   the interferences across the two methods are not directly transferable (particularly wavelength overlap

776   versus mass interference) that the two datasets are in excellent agreement demonstrates the two

777   techniques are accurately recording a statistical snapshot of apatite-glass distribution coefficients.

778   Looking at the same data in more detail, it is equally important to note despite having nearly 4 orders of

779   magnitude difference in detection limit, the two sets of data record similar error. In fact in some

780   experiments the LA-ICP-MS methodology records marginally higher error than the EPMA dataset despite

781   having a lower LOD (we suggest this relates to the difference in analyte volume across the two

782   techniques). In some cases, techniques with superior counting statistics will improve error in data like

783   that Fig 14-18 or calibrations presented in *Equations 17-18*. However in this case, the two techniques

784   record the same error when apatite analyses of single charge are considered, which is strong evidence

785   that the uncertainty is intrinsic to the experimental technique (i.e., reported from multiple analyses

786   from multiple crystals within a common experiment). Thus, the error represents the statistical variation

787   observed within the population of apatite grains from the experimental technique rather than being

788   related to analytical counting statistics. As a check of this hypothesis, one can compare results

789   presented in this paper with experimental data within the literature by Fleet and Pan (1995; n = 11 or

790   12; La-doped = 9.93±0.74, Nd-doped = 12.74±0.54, Gd-doped = 10.36±0.54, Dy-doped = 9.08±0.35),

791   Watson and Green (1985; n = 7-10; experiment 818 La_2O_3= 0.29±0.07, Sm_2O_3= 0.43±0.05, Dy_2O_3 =

792   0.35±0.06; Lu_2O_3 = 0.19±0.05, experiment 811, La_2O_3= 0.84±0.10, Sm_2O_3= 1.47±0.13, Dy_2O_3 = 1.34±0.12,

793   Lu_2O_3 = 0.65±0.10) and Trail et al., 2012 (here we use experiment zfo2_16d because it has the highest n

794   within the dataset; La_2O_3 = 0.232±0.183, Ce_2O_3 = 0.323±0.168, Pr_2O_3 = 0.269±0.155) are all in the same

795   reported range as that reported in the various Tables and Figures presented here.

796

Apatite saturation, glass compositions and application considerations

798   The apatite saturation calibration for mafic melts (Watson, 1979; Green and Watson, 1982) indicates

799   that, P_2O_5, SiO_2 and temperature play dominant roles that define apatite saturation. Results presented

800   in this study, which include 421 individual glass measurements, show agreement with the original

801   Watson (1979) apatite saturation calibration for experiments at 1 bar (Fig. 10). Specifically, the bulk of

802   glass measurements show the same topology in P_2O_5-SiO_2 space and the data falls between the 1165-

803   1200 °C saturation curves. This is an important observation in that the two sets of experiments

804   reproduce similar results and can be used to suggest apatite crystallization likely occurred under

805   equilibrium saturation conditions. Apatite saturation models are important when considering the

806   process of apatite crystallization in mafic systems (e.g., terrestrial, lunar or martian basalts), because at

807   the silica contents in question, apatite saturation tend to indicate a significant P_2O_5 content enrichment

808   is required to attain apatite nucleation. This being said, it should be stressed that experimental

809   petrology often represents a simplified or an artificially doped system and as such they may not be an

810   exact match for the full breadth of factors or complexities surrounding all range natural systems. This

811   being said, experimental petrology is an extremely useful guide to elucidating mechanisms that drive

812   geochemical variations observed in natural systems, of which oxygen fugacity is one of the most

813   important and hard to calculate.

814

815   The complex multiplicity of potential REE substitution mechanisms in apatite described by *eq. 6-9*, in

816   conjunction with the compositional range of apatite-saturated magmas, suggests that the activity of

817   other system components may influence REE[3+] and Eu^{2+} partitioning. As described by *eq. 6* and *7* the

818   a_{SiO_2}, a_{Na_2O}, and a_{CaO} in a silicate melt, though difficult to calculate in terms of absolute values without

38

819   a suitable buffer reaction, all potentially influence the relative partitioning of REE^{3+} and Eu^{2+}. If we take

820   *eq. 6* as an example, theory predicts melts of higher silica activity (e.g., rhyolites) will contain apatite of

821   higher $D_{\Sigma REE^{3+}}$ (at a constant REE activity) than silicate melts at lower silicate activity (e.g., basalts). The

822   apatite-melt REE partitioning presented by Watson and Green (1981) helps provide some evidence for

823   this (with details surrounding the different experimental starting materials presented in Table 4). The

824   more mafic melts presented by Watson and Green (1981) with low SiO_2 content (38.4-56.5 wt% SiO_2;

825   basanites, tholeiites, hawaiites, tholeiitic andesites) show notably lower partition coefficients (D_{MREE} =

826   4.0-6.0) than more silicic melts (56.5-69.7 wt% SiO_2; granites and andesite, where D_{MREE} = 9.0-40.0).

827   When the data from this study and that of Watson and Green (1981) are considered collectively, results

828   indicate melt composition and coupled substitution can affect REE partitioning in apatite.

829

830   Moreover, experimental studies into other accessory phases (e.g., zircon) have shown that mineral

831   solubility can also be dependent on the alkalinity of a melt. In holocrystalline rocks this is often

832   visualized in terms of the alumina saturation index (ASI) versus the "Na_2O+K_2O content" (in wt%) from

833   bulk rock analysis. In experimental systems where both glass and mineral can be measured, a slightly

834   different methodology is commonly used, known as the M factor (where M = [Na+K+2·Ca]/[Al·Si];

835   Watson and Harrison, 1983). This melt composition control not only plays a role in the solubility of the

836   mineral species, but also has the capacity to affect the coordination (and thus partitioning behavior) of

837   REE^{3+} and Eu^{2+} respectively. It is for this reason, for example, that redox calibrations in zircon require

838   different calibrations (e.g., $[Ce/Ce^*]_D$) depending on the alkalinity of the parent melt (Trail et al., 2012).

839   It is possible then, that melts significantly different to those presented in this study (i.e., peraluminous

840   and peralkaline magmas), likely have different $(Eu/Eu^*)_D$ redox curves from those in *eq. 17* and *18*.

841

39

842   Apatite practitioners who wish to utilize the experimental data presented here will need to carefully

843   consider whether the experimental conditions, the constraints provided, and reproducibility of the data

844   can be appropriately applied the system they seek to investigate.

845   **REE site occupancy and partitioning in apatite.**

846   A summary of REE partition coefficient data can be found in Supplement 2 and is shown graphically in

847   Figures 10-19. The data presented here can be used to evaluate the REE^{3+} coupled substitution

848   mechanism in apatite within experiments. As outlined in *eq. 6-9*, several possible substitution

849   mechanisms have been hypothesized. Watson and Green (1981), Fleet and Pan (1994; 1995) and

850   Cherniak (2000) indicate the dominant REE substitution mechanism in fluorapatite involves Si (i.e., *eq.*

851   *6*). The apatite data from this study (Supplement 1) and the mafic, REE-doped experiments of Watson

852   and Green (1981) generally show $\Sigma REE^{3+} + Si^{4+}:Ca^{2+} + P^{5+}$ (in apfu) close to the 1:1 coupled substitution, or a

853   strong positive correlation between ΣREE_2O_3 and SiO_2 (Fig. 11). This observation, coupled with the low

854   measured Na content in experimental apatite grains (i.e., generally below detection limit), indicates a

855   single dominant substitution mechanism within experiments.

856

857   The REE^{3+} partitioning data for apatite in basalt, here focusing on La, Ce, Sm, Gd and Lu, all show a

858   general concave down topology when plotted against ionic radii (Fig. 12, 13, 14 and 20). Moreover,

859   direct comparison of EPMA data and LA-ICP-MS data (see Fig. 11 and 18) show excellent Onuma

860   topology agreement across the two techniques, for both apatite and merrillite. All measured REE^{3+}

861   partition coefficients from apatite in this study straddle unity, with the MREE (Sm, Eu^{3+} and Gd; *D*

862   ranging from 1.0-2.0) and are considered to be marginally compatible, while the LREE and HREE being

863   marginally incompatible (La, Ce^{3+}, Lu; *D* ranging from 0.5-1.0). Interestingly, these experimental values

864   are similar to REE^{3+} partition coefficient data from lunar apatite grains reported by Jolliff et al. (1993)

865   which record MREE values ~0.4 and LREE and HREE recording slightly lower values (0.12-0.30). As shown

866   in Figures 10 and 11 this lattice strain topology and compatibility is also in agreement with previous

867   experimental work in apatite-saturated melts (Watson and Green, 1981; Prowatke and Klemme, 2006),

868   all showing the highest compatibility (or the ideal trivalent cation radius in the Onuma diagram)

869   somewhere between Sm and Gd (i.e., MREE). As all lattice strain calculations from this work indicate

870   that Eu^{3+} is the most proximal REE^{3+} element to the apex of the parabola (i.e., it is the most compatible

871   trivalent element in apatite), suggests that it is theoretically possible to produce a $\left(\frac{Eu}{Eu*}\right)_D^{\sqrt{Sm \times Gd}}$ slightly

872   >1. This is because Eu^{3+} is slightly more compatible than both Sm and Gd, and thus the square root

873   methodology could result in small positive $\left(\frac{Eu}{Eu*}\right)_D^{\sqrt{Sm \times Gd}}$ values in highly oxidized systems based on

874   *Equation 14*. This being the case, partitioning among the $MREE^{3+}$ are so similar that the development of

875   a measurable positive Eu anomaly based on partitioning among Sm^{3+}, Eu^{3+} and Gd^{3+} is unlikely.

876

877   The MREE (Sm, Eu and Gd) cations show a slightly smaller ionic radii than the ideal Ca^{2+} site apatite (be it

878   [XII], [IX] or the simplified [VI] structure used in this study), while the Eu^{2+} displays a slightly larger ionic

879   radii than Ca^{2+} in all coordinations relevant to the apatite structure. This could be used to suggest a

880   minor pressure effect on the relative partition coefficient of the two Eu valence species in apatite. This

881   could also be used to explain the marginally higher (i.e., ~half log unit) partition coefficients observed in

882   both the Watson and Green (1981) and Prowatke and Klemme (2006) studies – all equilibrated at

883   pressures between 0.75-2.00 GPa – relative to data presented in this study (where experiments are

884   equilibrated at 1 bar). Another plausible explanation for the marginally lower partition coefficients

885   observed in experiments presented here versus Watson and Green (1981) – the only other experimental

886   study of silicate-apatite systems – is that those experiments were generally conducted at lower

887   temperature (950-1120 °C). As partition coefficients generally increase with decreasing temperature (for

888   examples based on experimental trace element partitioning between silicate melts and zircon or apatite

889   or monazite see Trail et al., 2012; Watson and Green, 1981; Xing et al., 2013) the higher temperature

890   experiments in this study would predict a lower partition coefficient while displaying the same topology.

891   The restricted range of temperatures (1110-1175 °C) and compositions (40-50 wt% SiO_2) observed in

892   experiments from this study makes it unsurprising that the topology in REE partitioning data between

893   apatite and basalt are remarkably consistent across all experiments presented here. The similarity in

894   measured partition coefficients justifies the lack of a temperature term in *Equation 3*, as any

895   temperature effect on REE^{3+} partitioning over the small range in temperature of the present

896   experiments is essentially less than the uncertainties associated with the various analytical techniques.

897

898   It is possible to calculate the weighted relative partition coefficient of Eu^{2+} and Eu^{3+} in experiments

899   where both Eu L_3 XANES $\left[\left(\frac{Eu^{3+}}{\Sigma Eu}\right)_{Apatite}\right]$ and partitioning data $\left[\left(\frac{Eu}{Eu*}\right)_D^{\sqrt{Sm \times Gd}}\right]$ exist. This represents the

900   first direct evaluation of Eu^{2+} partitioning in apatite, though many previous studies have used Sr^{2+}

901   partitioning data as a proxy for Eu^{2+}. Direct comparison of $Eu^{3+}/\Sigma Eu$ XANES speciation curves for basalt

902   and apatite (see Fig. 15.b-c) converge at $\log(f_{O_2})$ values >-9 (i.e., >QFM), where Eu^{2+} content in both the

903   glass and apatite is small and the shape of the sigmoid becomes of limited use in terms of defining the

904   redox-related Eu partitioning. In order to estimate partition coefficients of both Eu valence states, we

905   recommend preferred values (Table 6) based on experiments at $\log(f_{O_2})$ values <-9 (i.e., at f_{O_2} conditions

906   near the locus of the sigmoid inflection). This method yields a combined XANES-EPMA $D_{Eu^{3+}}^{Ap/melt}$ of

907   1.81±0.26, which is very similar to the average partition coefficient calculated from lattice strain

908   methods applied to all experiments in this study, where $D_{Eu^{3+}}^{Ap/melt}$ is 1.67±0.25 (noting that the ideal

909   radius or r_0=0.957 is very similar to the radius of $^{[VI]}Eu^{3+}$=0.947). Similarly, the $\left(\frac{Eu}{Eu*}\right)_D^{\sqrt{Sm \times Gd}}$ method can

910   be used to calculate a $D_{Eu^{3+}}^{Ap/melt}$ of 1.67±0.23 and thus also indicates a value similar to the combined

911   XANES-EPMA $D_{Eu^{3+}}^{Ap/melt}$ of 1.81±0.26. The partition coefficient of divalent Eu calculated from this study

912   indicates Eu^{2+} is less compatible than Eu^{3+} within apatite and records an average $D_{Eu^{2+}}^{Ap/melt}$ of 0.87±0.08

913   and the $\left(D_{Eu^{2+}}^{Ap/melt}/D_{Eu^{3+}}^{Ap/melt}\right)$=0.48±0.27. The only comparison that can be made from previous

914   experimental work into apatite-basalt REE partitioning is that of Watson and Green (1981), whose data

915   can be used in lattice strain calculations to constrain $D_{Eu^{3+}}^{Ap/melt}$, and where $D_{Sr^{2+}}^{Ap/melt}$ can be used to

916   estimate $D_{Eu^{2+}}^{Ap/melt}$. This method results in similar values, where $D_{Eu^{3+}}^{Ap/melt}$ is 5.18±0.35, $D_{Eu^{2+}}^{Ap/melt}$ is

917   1.35±0.07 and $\left(D_{Eu^{2+}}^{Ap/melt}/D_{Eu^{3+}}^{Ap/melt}\right)$=0.26±0.03. In other words, the techniques described here and re-

918   evaluation of the Watson and Green (1981) data indicate that Eu^{3+} is approximately 2-4 times more

919   compatible than Eu^{2+} in apatite crystallizing from basalt.

920

921   Another important observation from this work, shown in Fig. 16, is the REE partition coefficients

922   ($D_{REE^{3+}}^{Ap/melt}$) for the strictly trivalent elements (i.e., isovalent cations: La, Sm, Gd and Lu) are nearly

923   constant over the complete range of experiment f_{O_2} conditions, such that the bulk of the REE appear

924   independent of f_{O_2}. It is important to note that Ce partitioning also remains constant over all

925   experimental f_{O_2} suggesting that the Ce^{4+} is highly incompatible in apatite and/or the Ce valence

926   speciation curve likely exists at higher f_{O_2} conditions than the experimental buffers used in this study.

927   This observation is consistent with previous studies in REE partitioning into the zircon-silicate melt

928   systems (Trail et al., 2012; Burnham and Berry, 2012) which demonstrates the $Eu^{2+} \leftrightarrow Eu^{3+}$ transition

929   occurs at much lower f_{O_2} than the Ce^{3+}-Ce^{4+}.

930

931   Another important observation that may be discerned from the Watson and Green (1981) experiments,

932   is where experiments are held at nearly constant melt composition-temperature-pressure-f_{O_2}, while

933   with H_2O content varies (in terms of wt% and presumably extending to $a_{H_2O}^{silicate\ melt}$), the REE

934   partitioning behavior remains nearly constant. As the Watson and Green (1981) experiments H_2O

935   contents generally exceeds the content observed in most terrestrial, lunar and martian basalts, can be

936   used to indicate that water activity plays a negligible role REE valence partitioning.

937

938   It has also been speculated that the volatile anion site may also play a role in the coupled substitution of

939   REE^{3+} (Fleet and Pan, 1997) by virtue of the F^-, Cl^- and OH^- each affecting the [VII]Ca(2) site (i.e., bond

940   angles and lengths describing the polyhedra) and thus potentially influencing REE^{3+} solubility in apatite.

941   While this may give rise to subtle differences in REE^{3+} partitioning among hydroxyapatite, fluorapatite

942   and chlorapatite end-members, the dominance of fluorapatite in igneous systems (Piccoli and Candela,

943   2002; Webster and Piccoli, 2002) and experiments presented here, likely means the anion site control

944   on REE partitioning among magmatic apatite grains is negligible for the bulk of magmatic redox

945   calibration purposes. The experimental studies into REE solubility among F^- and OH^- apatite by Prowatke

946   and Klemme (2006) also show only subtle differences on REE partitioning, again suggesting the anion

947   site plays little role on REE^{3+} partition coefficient.

948

949   These observations collectively demonstrate the two (Eu/Eu*)$_D$ calibrations for apatite theoretically laid

950   out in *Equations 7* and *8* and defined by calibrations presented in *Equations 17* and *18* here are best

951   applied to metaluminous, near basaltic melts that are similar in composition and pressure to those

44

952   presented in this experimental study. In other words, this calibration should not be applied to more

953   silicic systems that are either peralkaline or peraluminous. Further experimentation is needed to

954   accurately extend the working range of the apatite redox sensor to a broader range of magmatic

955   systems, including those of significantly different melt composition (silicic systems, peralkaline and

956   peraluminous systems) and at different pressures, (in order extend use from volcanic to plutonic

957   systems).

958

959   **Lattice strain calculations and assumptions.**

960   The lattice-strain model presented in *Equation 12* (Blundy and Wood, 1994) has previously been applied

961   to a wide range of phases (e.g., plagioclase, clinopyroxene, garnet, zircon, etc), where Klemme and

962   Dalpé (2003) present the only calculations made from experimental apatite crystals co-existing with a

963   melt. This calculated Eu^{3+} partition coefficient - which can be determined from a suite of trivalent ions

964   (e.g., REE^{3+}, Y^{3+}, Sc^{3+}, etc) that substitute on the same structural site(s) - can be combined with the

965   measured Eu partition coefficient (which includes both Eu^{2+} and Eu^{3+} components) in order to determine

966   the intensity of a negative Eu anomaly. Similar methods have been reported for Ce in zircon-melt

967   partitioning studies in the works of Burnham and Berry (2012) and Smythe and Brenan (2016).

968

969   As the results presented in Tables 4, 4b and 5 predict REE^{3+} substitution for Ca^{2+} (*eq. 5*), lattice strain

970   calculations necessarily assume substitution on the Ca sites within apatite. This being the case, the

971   apatite structure has two Ca sites - here defined as Ca(1) and Ca(2) (Fig. 2). The Ca(1) site can be

972   described as a 9-coordinated, tricapped trigonal prism site where 6 oxygens form a trigonal prism with

973   bond lengths varying from 2.40-2.46 Å (here modeled on Gd substitution on the Ca(1)-01 and Ca(1)-02

45

974   sites; Hughes and Rakovan, 2002; Fleet and Pan, 1995). An additional three oxygen atoms (Ca(1)-03),

975   essentially coplanar with the Ca(1) site, are found at greater distance (2.81 Å) from the central ion. The

976   Ca(2) site is bound to 6 oxygens with broadly similar ionic radii [Ca(2)-01 = 2.67 Å, Ca(2)-02 = 2.37 Å,

977   Ca(2)-03 = 2.50 Å, Ca(2)-03^d = 2.35 Å; again based on Hughes and Rakovan, 2002; Fleet and Pan, 1995]

978   and one column anion (*X*, in experiments generally F). As discussed by Klemme and Dalpé (2003),

979   substitution on both the Ca(1) and Ca(2) sites in apatite is dominated by 6-coordinated structural

980   components, with only minor contributions from the more distal Ca(1)-03 and Ca(2)-F bonds. In order to

981   make lattice strain calculations and to be consistent with previous calculations made from apatite (i.e.,

982   Klemme and Dalpé, 2003), here the REE^{3+} substitution in apatite is based on a simplified 6-fold

983   coordination (Fig. 1). As a consequence of this methodology, calculations necessarily assume there is no

984   site preference or change in solubility among the two Ca sites (Ca1 and Ca2) at experimental conditions.

985

986   While the simplified $^{[VI]}$Ca site can be justified, X-ray diffraction (XRD) unit cell refinements of high REE-

987   concentration apatite grains (carbonatitic and alkaline magmas) by Hughes et al. (1991), a study

988   reporting substitution consistent with *eq. 6* and *eq. 7* dominating charge balance, indicates minor site

989   preference for the LREE on the $^{[VII]}$Ca(2) site, no observable site preference for the MREE and, minor

990   preference for the HREE on the $^{[VI+III]}$Ca(1) site. While these site preferences may be important in some

991   systems, the Hughes et al. results indicate no complete exclusion of specific REE on any site, with

992    $\mathrm{REE}_{[VII]_{Ca(2)}}/\mathrm{REE}_{[VI+III]_{Ca(1)}}$ ranging from 1.8-3.0. As the $\left[\left(\frac{\mathrm{Eu}}{\mathrm{Eu*}}\right)_D^{\sqrt{\mathrm{Sm}\times\mathrm{Gd}}}\right]$ redox calibration is largely

993   dependent on mid-REE, this suggests site preference is highly unlikely to affect *eq. 14*. The subtle

994   variations in site preference between LREE+HREE and MREE have some capacity to affect the shape of

995   the Onuma projection, and therefore r_0. This could explain the subtle differences in the LREE:MREE seen

996   between the results of this study and the Watson and Green study (1981) versus that observed in

46

997   Prowatke and Klemme (2006), though additional XRD or X-ray absorption fine structures (XAFS) data

998   would be required to confirm any crystal chemical control on site preference among the different REE^{3+}

999   cations.

1000

1001   For comparison purposes, lattice calculations $\left[\left(\frac{Eu}{Eu^*}\right)_D^{lattice\ strain}\right]$ made from apatite in Klemme and

1002   Dalpé (2003) are included in a complete list of lattice strain calculations from experiments in this study

1003   presented in Table 5. In order to make direct comparison with other experimental studies in mafic

1004   silicate systems, lattice strain calculations were made on apatite-melt data presented by Watson and

1005   Green (1981; Table 5).

1006

1007   The ionic radius of Eu^{3+} in 6-coordination (0.947 Å) is very similar to the ideal radius calculated from

1008   lattice strain averaged from all apatite-basalt experiments in this study (r_0 = 0.957 ± 0.008 Å) and from

1009   data reported by Watson and Green (1981; 0.960 and 0.952 Å for apatite grains reported from mafic

1010   systems). This demonstrates the apex of the REE^{3+} parabola or the most compatible REE^{3+} element in

1011   apatite is proximal to Eu^{3+}, meaning the most compatible REE in apatite is also the most important

1012   variable-valence REE. This is a fortuitous situation in terms of use of an REE anomaly, as it means the

1013   proximity to the apex of the Onuma parabola - when coupled to the relatively incompatible nature of

1014 Eu^{2+} - should give rise to the greatest possible resolution in the redox variable element (i.e., the lowest

1015   possible analytical uncertainty).

1016

47

1017   Comparison of $\left[\left(\frac{Eu}{Eu^*}\right)_D^{\text{lattice strain}}\right]$ and $\left[\left(\frac{Eu}{Eu*}\right)_D^{\sqrt{Sm \times Gd}}\right]$ is shown in Figures 17 and 18, with the two

1018   techniques showing excellent correlation (i.e., plotting very close to the 1:1, with a slope of 0.97 and an

1019   intercept of 0.03). As stressed earlier in the discussion, two factors complicate lattice strain models for

1020   apatite: (1) Apatite has two distinct cation sites [Ca(1) and Ca(2)] and a complete lattice strain model

1021   requires determination of, and projection of, partitioning data for each individual Ca site (a condition

1022   not possible to measure via EPMA or LA-ICP-MS); and (2) The various coupled substitution mechanisms

1023   for REE partitioning into apatite (see eq. 6-9) likely distort the cation site locally (and proportionately for

1024   the individual coupled substitution mechanisms) and this likely complicates lattice strain calculations for

1025   REE in apatite. Even where the assumptions in the lattice strain model are an oversimplification (e.g., 6-

1026   coordination on a single site), the calculated [ln(D_0)] and r_0 still represent an accurate evaluation of the

1027   intensity of the Eu anomaly. The Young's modulus estimates presented in Table 5, by contrast, should be

1028   regarded with caution (even though results are consistent with previous methods of Klemme and Dalpé,

1029   2003).

1030

1031   **Comparison of the three calibrations.**

1032   The different analytical techniques and three different Eu valence calibrations presented in this study all

1033   show a smooth trend of increasing (Eu/Eu*)$_D$ or (Eu^{3+}/ΣEu)$_{Apatite}$ or (Eu^{3+}/ΣEu)$_{Melt}$ with increasing

1034 $\log(f_{O_2})$ (see Fig. 14, 15 and 18). The simplest way to envisage the relationship between oxygen

1035   fugacity and intensity of (Eu/Eu*)$_D$ is to directly compare partitioning data among isothermal

1036   experiments at different f_{O_2}. This is shown graphically in Fig. 14, where 1150 °C experiments at Fe$_2$O$_3$-

1037   Fe$_3$O$_4$ (HM) shows no anomaly, Ni-NiO (NNO) shows a small anomaly and C-CO-CO$_2$ (CCOCO2) shows a

1038   pronounced negative Eu anomaly. This change in partitioning behavior follows a sigmoidal relationship

1039   in $\log(f_{O_2})$-$(Eu/Eu^*)_D$ or $\log(f_{O_2})$-$(Eu^{3+}/\Sigma Eu)_{Apatite}$ space, as would be predicted by *Equation 4*. By

1040   carrying out least squares regressions on experiments using each method (i.e., *Equations 11*, *13*, and

1041   14), it is possible to derive redox calibrations for each (shown graphically in Figures 15 and 18) and these

1042   are described in *Equations 15-18*.

1043

1044   **XANES calibration.**

1045   A total of 9 representative experiments ranging in $\log(f_{O_2})$ from -14.5 to -3.3, or from the graphite-CO-

1046 CO_2 buffer to the hematite-magnetite buffer, are used to define the Eu valence sigmoid for both apatite

1047   and the co-existing glass. The sigmoid calculated from $(Eu^{3+}/\Sigma Eu)_{apatite}^{XANES}$ data are from individual

1048   experiments, presented in Table 6, define the following calibration (Fig. 15):

1049

1050 $$\left(\frac{Eu^{3+}}{\Sigma Eu}\right)_{apatite}^{XANES} = \frac{1}{1+10^{-0.10\pm0.01\times\log(f_{O_2})-1.63\pm0.16}}$$ *(eq. 15)*

1051

1052   The $(Eu^{3+}/\Sigma Eu)_{glass}^{XANES}$, by contrast, reports a calibration shifted slightly to higher f_{O_2} (see Fig. 15):

1053

1054 $$\left(\frac{Eu^{3+}}{\Sigma Eu}\right)_{glass}^{XANES} = \frac{1}{1+10^{-0.15\pm0.01\times\log(f_{O_2})-2.49\pm0.18}}$$ *(eq. 16)*

1055

1056   The minor f_{O_2} shift recorded in calibrations for both apatite and co-existing glass (Fig. 15) is essentially a

1057   measure of the differing compatibilities of Eu^{3+} and Eu^{2+} in apatite. As Eu^{3+} is more compatible, the

49

1058   sigmoid shifts to lower f_{O_2} than is directly observed in the glass. Very similar results have been reported

1059   from Eu L_3 XANES spectra from augites in basalt (Karner et al., 2010), while the inverse relationship is

1060   observed between plagioclase and basalt (because Eu^{2+} is the more compatible valence species in

1061   plagioclase; Drake, 1975). It is also possible that some of this offset between the XANES Eu sigmoid

1062   between glass and apatite is related to the non-systematic substitution of Eu^{2+} in the different cation

1063   sites (i.e., 7- and 9-coordinated polyhedra) when compared directly to Eu^{3+}.

1064

1065   **The lattice strain calibration.**

1066   The lattice strain-based Eu valence calibration or $\left[\left(\dfrac{Eu}{Eu^*}\right)_D^{\text{lattice strain}}\right]$ based on results presented in Table

1067   5 and shown graphically in Figure 18.b is defined by:

1068

1069 $$\left(\frac{Eu}{Eu*}\right)_D^{\text{lattice strain}} = \frac{1}{1+10^{-0.20\pm0.03\times\log\left(f_{O_2}\right)-3.03\pm0.42}}$$ *(eq. 17)*

1070

1071   **The $\left(\dfrac{Eu}{Eu*}\right)_D^{\sqrt{Sm\times Gd}}$ calibration**

1072   The Eu valance calibration based on neighboring Sm and Gd or $\left[\left(\dfrac{Eu}{Eu*}\right)_D^{\sqrt{Sm\times Gd}}\right]$ records a very similar (as

1073   shown in Fig. 18.a) trend to the lattice strain calibration and is defined by:

1074

1075 $$\left(\frac{Eu}{Eu*}\right)_D^{\sqrt{Sm\times Gd}} = \frac{1}{1+10^{-0.15\pm0.03\times\log\left(f_{O_2}\right)-2.46\pm0.41}}$$ *(eq. 18)*

50

1076

1077   It should be noted that "x" in *Equation 4*, or the coefficient defining the slope of the sigmoid, for all

1078   three techniques–0.10±0.01 from Eu XANES; 0.20 ± 0.03 from $\left[\left(\frac{Eu}{Eu^*}\right)_D^{\text{lattice strain}}\right]$, and; 0.15±0.03 from

1079 $\left[\left(\frac{Eu}{Eu^*}\right)_D^{\sqrt{Sm \times Gd}}\right]$ – is slightly lower than the theoretical value described by *Equation 1* (where x = 0.25).

1080   There are many possible explanations for this, but the mostly likely explanation is changing melt

1081   composition with ΔT and Δf_{O_2}, with the most reducing experiments (i.e., $\log(f_{O_2})<-12$) showing a

1082   dramatic decrease in FeO* content with the crystallization of schreibersite (see Fig. 19). This change in

1083   melt composition and structure likely means the activity coefficients described in *Equation 3* are not

1084   strictly constant. As discussed earlier in this manuscript, oxide solid state buffers can also influence

1085   glass/melt composition within experiments, which may also subtly influence activity coefficients across

1086   different experiments. This is the most likely cause for the difference between measured and theoretical

1087   coefficients for the sigmoid, but we note that natural basalts crystallizing at low f_{O_2} (e.g., lunar basalts)

1088   can also exhibit native iron (metal) and also likely undergo dramatic changes in melt composition during

1089   fractionation.

1090

1091   **Comments on Merrillite REE partitioning.**

1092   Several experiments in this study permit an evaluation of the relative partitioning of REE^{3+} and Eu^{2+}

1093   valence species between apatite-merrillite-silicate melt, under the caveat that merrillite is present only

1094   in oxidized experiments from this study (ApREE-01a and ApREE-04). The merrillite results presented

1095   here should only be considered a guide to partitioning, as further experimentation is required to confirm

1096   partitioning over a full range of f_{O_2} conditions. As in previous comments regarding the lattice parabola

1097   in apatite, it is important to note that the Onuma diagram from LA-ICP-MS and EPMA techniques are in

51

1098   excellent agreement. As shown in Fig. 13.c and 20.a, the $D_{\mathrm{REE}^{3+}}$ are ~2.9 (Lu) to ~5.7 (La) times more

1099   compatible or approximately half an order of magnitude more compatible in merrillite than in apatite

1100   (see Supplement 2). It is also important to note that the topology of the Onuma diagram for both phases

1101   are similar, though the LREE:HREE (as measured by La/Lu) tends to be lower in apatite (1.79±0.38) than

1102   in merrillite (3.05±0.57). This similarity in topology tends to suggest the that two phases are unlikely to

1103   fractionate REE^{3+} sufficiently to dramatically change parameters used to constrain the intensity of an Eu

1104   anomaly [i.e., $(\mathrm{Eu/Eu^*})_D$; parameters like $\sqrt{\mathrm{Sm} \times \mathrm{Gd}}$ or the topology of the lattice strain parabola].

1105

1106   Direct comparison of $\left(\dfrac{\mathrm{Eu}}{\mathrm{Eu}*}\right)_D^{\mathrm{Sm-Gd}}$ for merrillite and apatite (see Fig. 20) also demonstrates that the two

1107   phases show complementary or positive correlation among Eu valence species. As shown in Figure 18a-

1108   18b, experiments at the hematite-magnetite buffer ($\log(f_{O_2})$ = -3.28) show a mildly positive $\left(\dfrac{\mathrm{Eu}}{\mathrm{Eu}*}\right)_D^{\mathrm{Sm-Gd}}$

1109   in both merrillite (1.04±0.02) and apatite (1.03±0.11). At the Ni-NiO buffer ($\log(f_{O_2})$ = -8.02) both

1110   phases show the development of a small negative anomaly, with $\left(\dfrac{\mathrm{Eu}}{\mathrm{Eu}*}\right)_D^{\mathrm{Sm-Gd}}$ merrillite (0.88±0.02) and

1111   apatite (0.94±0.14) both reporting values below unity. From this limited dataset it can be hypothesized

1112   that Eu^{2+} is slightly more incompatible within the merrillite structure than it is within the apatite

1113   structure, leading to the merrillite recording slightly larger negative Eu anomalies than apatite. This

1114   being the case, the relative difference in compatibility between REE^{3+} and Eu^{2+} is sufficiently small that

1115   neither phase (merrillite or apatite) is likely to significantly influence oxygen fugacity estimates made

1116   from the other phase based on either $\left(\dfrac{\mathrm{Eu}}{\mathrm{Eu}*}\right)_D^{\mathrm{Sm-Gd}}$ or $\left(\dfrac{\mathrm{Eu}}{\mathrm{Eu}*}\right)_D^{\mathrm{lattice\ strain}}$. This is true of a situation where

1117   both phases co-crystallize or where phase saturation occurs at different times/temperatures in the

1118   liquid line of decent (i.e., if saturation of one phase occurs earlier than the other).

52

This is the peer-reviewed, final accepted version for American Mineralogist, published by the Mineralogical Society of America. The published version is subject to change. Cite as Authors (Year) Title. American Mineralogist, in press. DOI: https://doi.org/10.2138/am-2022-8388. http://www.minsocam.org/

1119

1120 **Application to natural apatite.**

1121 Existing REE valence calibrations in minerals, namely Ce/Ce*-in-zircon (Trail et al., 2012; Burnham and

1122 Berry, 2012; Smythe and Brenan, 2016), can be applied to "out of context" grains under specific

1123 circumstances, largely because independent thermometers for the mineral exist (e.g., Ti-in-zircon or

1124 zircon saturation models). This is because Ce^{4+}/Ce^{3+} is not considered to be strongly fractionated from

1125 neighboring LREE by crystallization of additional phases during magmatic evolution. The same scenario is

1126 not true of magmatic apatite, and there are two major concerns regarding application of Equations 17

1127 and 18: (i) fractionation of Eu^{3+}/Eu^{2+} during crystal-melt evolution can be influenced by the

1128 crystallization of phase/s that preferentially partition one of the Eu valence species, thus giving rise to

1129 spurious estimates of the Eu/Eu*, and (ii) basaltic melts can have an intrinsic Eu^{3+}/Eu^{2+} derived from the

1130 composition of the melt source.

1131

1132 Previous f_{O_2}-temperature experimental studies, combined with this study into basaltic systems,

1133 demonstrate that augite, diopside and apatite (and on the basis of crystal structures/compositions,

1134 presumably olivine and spinel) all show partition coefficients where $D_{Eu^{2+}}^{Mineral/melt}<D_{Eu^{3+}}^{Mineral/melt}$, and

1135 where $D_{Eu^{3+}}^{Mineral/melt}$ are approximately at or below unity (see Fig. 20). Calculations based on natural

1136 systems (e.g., Schnetzler and Philpotts, 1970; Jolliff et al., 1993, 2006) and experimental studies by

1137 Drake (1972) and Drake and Weill (1975), demonstrate that the partition coefficient of Eu^{2+} in

1138 plagioclase is significantly higher than for other REE^{3+}. The experiments of Drake (1972) equilibrated at

1139 1290-1300 °C, for example, show $D_{Eu^{2+}}^{plag/basalt}=1.65$, while $D_{Eu^{3+}}^{plag/basalt}=0.045$ (at temperatures

1140 comparable to this study). This represents a two order of magnitude difference in partitioning among Eu

53

1141   valence species, where one valence species is compatible and the other highly incompatible. This

1142   partitioning behavior, particularly in melts existing at an f_{O_2} that approximates the inflection point of

1143   the $Eu^{2+} \leftrightarrow Eu^{3+}$ sigmoid (i.e., existing at mixed valence state), has the capacity to significantly fractionate

1144   bulk Eu from neighboring Sm and Gd (thus influencing estimates of f_{O_2} made from revised *Equations 13*

1145   and *14*; i.e., where melt composition cannot be analyzed). Moreover, these studies (Drake, 1972; Drake

1146   and Weill, 1975) indicate that while Eu^{3+} partitioning appears to be insensitive to temperature variations

1147   (i.e., the slope approaches zero in $\frac{1}{T} - \ln D_{Eu^{3+}}^{plag/basalt}$ space; with similar slopes observed for Sm and Gd),

1148   the partitioning of Eu^{2+} appears to show a notable temperature effect. The work of Drake (1972; 1975)

1149   and Drake and Weill (1975) show an increasing compatibility with decreasing temperature (as is the case

1150   for most trace elements) – but this temperature effect is also accompanied by a change in plagioclase

1151   composition (from anorthitic to albitic compositions with decreasing temperature). The net result of

1152   decreasing temperature and changing plagioclase composition is that a melt develops an increasing

1153   negative Eu anomaly with progressive plagioclase crystallization. Given the control of bulk composition

1154   on the liquid line of descent — particularly the temperatures, composition and quantity of plagioclase

1155   and apatite crystallization — each basaltic system likely needs to be considered individually (i.e., there is

1156   no unique solution that can be broadly applied among basalts). This being the case, if apatite and

1157   plagioclase crystallize at similar conditions, or the temperature-composition interval for each phase can

1158   be calculated, then the reciprocal relationship among the Eu/Eu* (i.e., intensity of the negative anomaly

1159   in apatite and positive anomaly in co-existing plagioclase) should converge on a common calculated f_{O_2}

1160   and could be used to evaluate f_{O_2} equilibria among co-existing phases. See Supplementary Material #4

1161   for a simplified example of calculating the effect of plagioclase fractionation on $\left[\left(\frac{Eu}{Eu*}\right)_D^{\sqrt{Sm \times Gd}}\right]$.

1162

1163   The second (ii) major concern regarding eq. 13 and eq. 14 (where melt composition cannot be

1164   measured), is whether the parent melt from which apatite saturates has an intrinsic Eu anomaly

1165   derived/inherited from the source material. Where global MORB or N-MORB or E-MORB appear to show

1166   no negative Eu anomaly, this likely relates to the lack of plagioclase in the mantle source region. This

1167   observation is not universally true of all basaltic melt sources. Lunar basalts, for example, all record a

1168   pronounced negative Eu anomaly thought to be related to the development of the lunar highlands (e.g.,

1169   plagioclase fractionation from the lunar magma ocean). In cases where there is an intrinsic anomaly, it is

1170   possible to calculate the effect of an inherited negative europium anomaly (Eu/Eu*) if the melt Eu^{2+}:Eu^{3+}

1171   is fixed at a given f_{O_2} (i.e., defined by XANES data) and partitioning is concentration independent and

1172   constant. Examples for $\left(\frac{Eu}{Eu*}\right)_D^{\sqrt{Sm \times Gd}}$ corrected for equilibrium fractionation of plagioclase and for

1173   inherited Eu anomalies are presented in Supplementary Material #2. While these calculations involve

1174   simplifications, they do demonstrate methodologies that can be used to make Eu valence corrections.

1175

1176   Clearly the 'best-case' scenario for all valence calibrations presented in this study involves situations

1177   where partitioning pairs (i.e., apatite-melt) can be calculated from melt inclusions hosted in apatite, or

1178   where apatite is found within glass, such that the two phases share a near contemporaneous

1179   temperature and chemical history. Whole rock analysis may be used to calculate REE concentrations

1180   within a melt, but the relative timing of phase crystallization (which can effectively fractionate among

1181   the REE) will be crucial to interpreting any calculated REE abundance. Similarly, if the melt composition

1182   changes significantly during fractional crystallization and REE are fractionated during crystallization of an

1183   accessory phase, bulk analysis can lead to spurious calculations.

1184

1185   **Implications and conclusions**

1186   This experimental study demonstrates that partitioning of Eu valence species into apatite can be used as

1187   an effective oxygen fugacity sensor. The REE content of apatite, like other phases that may potentially

1188   crystallize from metaluminous melts (e.g., zircon, pyroxene, etc.), can be used to determine redox

1189   conditions [log(f_{O_2})] in basaltic systems over a 1110-1175 °C range (i.e., the temperatures broadly

1190   approximating the near-solidus in a dry basalt at 1 bar pressure). Application of this calibration is best

1191   carried out in systems where co-existing apatite and glass are present (e.g., melt inclusions in volcanic

1192   apatite phenocrysts or where glass-apatite are immediately adjacent), under such circumstances no

1193   corrections for fractionation (e.g., plagioclase crystallization) or inherited anomalies need be considered.

1194   Numerous studies into the various meteorite and Apollo collections, which demonstrate apatite

1195   abundance within a range of mafic rocks, suggest that the calibration has broad application and can be

1196   used to evaluate the oxidation state of numerous terrestrial bodies.

1197

1198   **Acknowledgements**

1214   **References**

1215

1216   Barbarand, J. and Pagel, M. (2001). Cathodoluminescence study of apatite crystals. American

1217   Mineralogist. 86, 473-484.

1218

1219   Berry, A.J. and O'Neill, H.St.C. (2004). A XANES determination of the oxidation state of chromium in

1220   silicate glasses. American Mineralogist. 89, 790-798.

1221

1222   Blundy, J. and Wood, B. (1994). Prediction of crystal-melt partition coefficients from elastic moduli.

1223   Nature. 372, 452-454.

1224

1225   Boyce, J.W., Liu, Y., Rossman, G.R., Guan, Y., Eiler, J.M., Stolper, E.M. and Taylor, L.A. (2010). Lunar

1226   apatite with terrestrial volatile abundances. Nature. 466, 7305.

1227

1228   Boyce, J.W., Tomlinson, S., McCubbin, F., Greenwood, J. and Treiman, A. (2014). The lunar apatite

1229   paradox. Science, 344 (6182), 400-402.

1230

1231   Brice, J.C. (1975). Some thermodynamic aspects of the growth of strained crystals. Journal of Crystal

1232   Growth. 28, 249-253.

58

1233

1234   Brounce, M., Boyce, J., McCubbin, F.M., Humphreys, J., Reppart, J., Stolper, E. and Eiler, J. (2019). The

1235   oxidation state of sulfur in lunar apatite. American Mineralogist. 104 (2), 307-312.

1236

1237   Burnham, A.D. and Berry, A.J. (2012). An experimental study of trace element partitioning between

1238   zircon and melt as a function of oxygen fugacity. Geochimica et Cosmochimica Acta. 95, 196-212.

1239

1240   Burnham, A.D. and Berry, A.J. (2014). The effect of oxygen fugacity, melt composition, temperature and

1241   pressure on the oxidation state of cerium in silicate melts. Chemical Geology. 366, 52-60.

1242

1243   Burnham, A.D., Berry, A.J., Halse, H.R., Schofield, P.F., Cibin, G. and Mosselmans, J.F.W. (2015). The

1244   oxidation state of europium in silicate melts as a function of oxygen fugacity, composition and

1245   temperature. Chemical Geology. 411, 248-259.

1246

1247   Cherniak, D.J. (2000). Rare earth element diffusion in apatite. Geochimica et Cosmochimica Acta. 64,

1248   3871-3885.

1249

1250   Cicconi, M.R., Giuli, G., Paris, E., Ertel-Ingrisch, W., Ulmer, P. and Dingwell, D.B. (2012). Europium

1251   oxidation state and local structure in silicate melts. American Mineralogist. 97, 918-929.

1252

1253   Drake, M.J. (1972). The distribution of major and trace elements between plagioclase feldspar and

1254   magmatic silicate liquid: an experimental study, 191 p. Ph.D. thesis, University of Oregon.

1255

1256   Drake, M.J. (1975). The oxidation state of europium as an indicator of oxygen fugacity. Geochimica et

1257   Cosmochimica Acta.39, 55-64.

1258

1259   Drake, M.J. and Weill, D.F. (1975). Partition of Sr, Ba, Ca, Y, Eu^{2+}, Eu^{3+}, and other REE between

1260   plagioclase feldspar and magmatic liquid: an experimental study. Geochimica et Cosmochimica Acta. 39,

1261   689-712.

1262

1263   Elderfield, H., Hawkesworth, C.J. and Greaves, M.J. (1981). Rare earth element geochemistry of oceanic

1264   ferromanganese nodules and associated sediments. Geochimica et Cosmochimica Acta. 45, 513-528.

1265

1266   Fleet, M.E. and Pan, Y. (1994). Site preference of Nd in fluorapatite [Ca10(PO$_4$)$_6$F$_2$]. Journal of Solid State

1267   Chemistry. 112, 78-81.

1268

1269   Fleet, M.E. and Pan, Y. (1995). Site preference of rare earth elements in fluorapatite. American

1270   Mineralogist. 80, 329-335.

1271

1272   Goles, G., Randle, K., Osawa, M., Schmitt, R.A., Wakita, H., Ehmann, W.D. and Morgan, J.W.(1970).

1273   Elemental abundances by instrumental activation analyses in chips from 27 lunar rocks. Proceedings of

1274   the Apollo 11 Lunar Science Conference.2, 1165-1176.

1275

1276   Green, T.H. and Watson, E.B. (1982). Crystallization of apatite in natural magmas under high pressure,

1277   hydrous conditions, with particular reference to 'orogenic' rock series. Contributions to Mineralogy and

1278   Petrology. 79, 96-105.

1279

1280   Greenwood, J.P., Itoh, S., Sakamoto, N., Warren, P., Taylor, L. and Yurimoto, H. (2011). Hydrogen isotope

1281   ratios in lunar rocks indicate delivery of cometary water to the Moon. Nature Geoscience. 4, 79.

1282

1283   Grutzeck, M., Kridelbaugh, S. and Weill, D. (1974). The distribution of Sr and REE between diopside and

1284   silicate liquid. Geophysical Research Letters. 1, 273-275.

1285

1286   Helmke, P.A., Blanchard, D.P., Haskin, L.A., Telander, K., Weiss, C. and Jacobs, J.W. (1973). Major and

1287   trace elements in igneous rocks from Apollo 15. The Moon. 8, 129-148.

1288

1289   Henderson, C.E. (2011). Protocols and Pitfalls of Electron Microprobe Analysis of Apatite. Masters thesis,

1290   University of Michigan. 68 pages.

1291

1292   Hubbard, N.J., Gast, P.W., Rhodes, J.M., Bansal, B.M. and Wiesmann, H. (1972). Nonmare basalts: Part II.

1293   Proceedings of the Third Lunar Science Conference. 2, 1161-1179.

1294

1295   Hughes, J.M., Jolliff, B.L. and Gunter, M.E. (2006). The atomic arrangement of merrillite from the Fra

1296   Mauro Formation, Apollo 14 lunar mission: The first structure of merrillite from the Moon. American

1297   Mineralogist. 91, 1547-1552.

1298

1299   Jolliff, B.L., Haskin, L.A., Colson, R.O. and Wadhwa, M. (1993). Partitioning in REE-saturating minerals:

1300   Theory, experiment, and modelling of whitlockite, apatite, and evolution of lunar residual magmas.

1301   Geochimica et Cosmochimica Acta. 57, 4069-4094.

1302

1303   Jolliff, B.L., Hughes, J.M., Freeman, J.J. and Zeigler, R.A. (2006). Crystal chemistry of lunar merrillite and

1304   comparison to other meteoritic and planetary suites of whitlockite and merrillite. American

1305   Mineralogist. 91, 1583-1595.

1306

1307   Karner, J.M., Papike, J.J., Sutton, S.R., Burger, P.V., Shearer, C.K., Le, L., Newville, M. and Choi, Y. (2010).

1308   Partitioning of Eu between augite and a highly spiked martian basalt composition as a function of

1309   oxygen fugacity (IW-1 to QFM): Determination of Eu^{2+}/Eu^{3+} ratios by XANES. American Mineralogist. 95,

1310   410-413.

1311

1312   Kato, Y., Kano, T. and Kunugiza, K. (2002). Negative Ce anomaly in the Indian Banded Iron Formations:

1313   evidence for the emergence of oxygenated deep-sea at ~2.9-2.7 Ga. Resource Geology. 52 (2), 101-110.

1314

1315   Klemme, S. and Dalpé, C. (2003). Trace-element partitioning between apatite and carbonatite melt.

1316   American Mineralogist.88, 639-646.

1317

1318   Konecke, B.A., Fiege, A., Simon, A.C., Linsler, S. and Holtz, F. (2019). An experimental calibration of a

1319   sulfur-in-apatite oxybarometer for mafic systems. Geochimica et Cosmochemica Acta. 265, 242-258.

1320

1321   Konecke, B.A., Fiege, A., Simon, A.C., Parat, F. and Stechern, A. (2017). Co-variability of S^{6+}, S^{4+}, and S^{2-} in

1322   apatite as a function of oxidation state: implications for a new oxybarometer. American Mineralogist.

1323   102, 548-557.

1324

1325   Mariano, A.N. and Ring, P.J. (1975). Europium-activated cathodoluminescence in minerals. Geochimica

1326   et Cosmochimica Acta. 39, 649-660.

1327

1328   Marks, M.A.W., Wenzel, T., Whitehouse, M.J., Loose, M., Zack, T., Barth, M., Worgard, L., Krasz, V., Eby,

1329   N., Stosnach, H. and Markl, G. (2012). The volatile inventory (F, Cl, Br, S, C) of magmatic apatite: An

1330   integrated analytical approach. Chemical Geology. 291, 241-255.

1331

1332   McCubbin F.M., Steele, A., Hauri, E.H., Nekvasil, H., Yamashita, S. and Hemley, R.J. (2010a). Nominally

1333   hydrous magmatism on the Moon. Proceedings of the National Academy of Sciences of the United

1334   States of America. 107 (25), 11223-11228.

1335

1336   McCubbin F.M., Steele, A., Nekvasil, H., Schnieders, A., Rose, T., Fries, M., Carpenter, P.K. and Jolliff,

1337   B.L.(2010b). Detection of structurally bound hydroxyl in fluorapatite from Apollo Mare basalt 15058,128

1338   using TOF-SIMS. American Mineralogist. 95 (8-9), 1141-1150.

1339

1340   McCubbin F.M., Jolliff, B.L., Nekvasil, H., Carpenter, P.K., Zeigler, R.A., Steele, A., Elardo, S.M., and

1341   Lindsley, D.H.(2011). Fluorine and chlorine abundances in lunar apatite: Implications for heterogenous

1342   distributions of magmatic volatiles in the lunar interior. Geochimica et Cosmochimica Acta. 75, 5073-

1343   5093.

1344

1345   Pan, Y. and Fleet, M.J. (2002). Composition of the apatite-group minerals: substitution mechanisms and

1346   controlling factors. Reviews in Mineralogy and Geochemistry.48, 13-49.

1347

1348   Plank, T. and Langmuir, C.H. (1998). The chemical composition of subducting sediment and its

1349   consequences for the crust and mantle. Chemical Geology. 145, 325-394.

1350

1351   Prowatke, S. and Klemme, S. (2006). Trace element partitioning between apatite and silicate melts.

1352   Geochimica et Cosmochimica Acta. 70, 4513-4527.

1353

1354   Rakovan, J., Newville, M. and Sutton, S. (2001). Evidence of heterovalent europium in zoned Llallagua

1355   apatite using wavelength dispersive XANES. American Mineralogist.86, 697-700.

1356

1357   Ravel, B. and Newville, M.A.T.H.E.N.A. (2005). ATHENA, ARTEMIS, HEPHAESTUS: data analysis for X-ray

1358   absorption spectroscopy using IFEFFIT. Journal of Synchrotron Radiation. 12,537-541.

1359

1360   Reed, R.J.B. and Buckley, A. (1998). Rare-earth element determination in minerals by electron-probe

1361   microanalysis: application of spectrum synthesis. Mineralogical Magazine. 62, 1-8.

1362

1363   Rhodes, G. and Hubbard, N.J. (1973). Chemistry, classification, and petrogenesis of Apollo 15 mare

1364   basalts. Proceedings of the 4th Lunar Science Conference.2, 1127-1148.

1365

1366   Roeder, P.L., MacArthur, D., Ma, X.-P., Palmer, G.R. and Mariano, A.N. (1987). Cathodoluminescence and

1367   microprobe study of rare-earth elements in apatite. American Mineralogist.72, 801-811.

1368

1369   Sha, L.-K. (2000). Whitlockite solubility in silicate melts: Some insights into lunar and planetary

1370   evolution. Geochimica et Cosmochimica Acta. 64, 3217-3236.

1371

1372   Shearer, C.K., Papike, J.J. and Karner, J.M. (2006). Pyroxene europium valence oxybarometer: Effects of

1373   pyroxene composition, melt composition, and crystallization kinetics. American Mineralogist.91, 1565-

1374   1573.

1375

1376   Smythe, D.J. and Brenan, J.M.(2016). Magmatic oxygen fugacity estimated using zircon-melt partitioning

1377   of cerium. Earth and Planetary Science Letters. 453, 260-266.

1378

1379   Strasheim, A., Coetzee, J.H.J., Jackson, P.F.S., Strelow, F.W.E., Wybenga, F.T., Gricius, A.J. and Kokot,

1380   M.L.(1972). Analysis of lunar samples 15065, 15301, and 15556, with isotopic data for 7Li/6Li. In The

1381   Apollo 15 Lunar Samples (Chamberlain and Watkins, eds), 257-259. The Lunar Science Institute,

1382   Houston.

1383

1384   Tartèse, R., Anand, M., Barnes, J.J., Starkey, N.A., Franchi, I.A. and Sano, Y. (2013). The abundance,

1385   distribution, and isotopic composition of Hydrogen in the Moon as revealed by basaltic lunar samples:

1386   Implications for the volatile inventory of the Moon. Geochimica et Cosmochimica Acta.122, 58-74.

1387

1388   Taylor, S.R., Gorton, M.P., Muir, P., Nance, W.B., Rudowski, R.R. and Ware, N. (1973). Composition of the

1389   Descartes region, lunar highlands. Geochimica et Cosmochimica Acta.37, 2665-2683.

1390

1391   Taylor, Stuart Ross. *Planetary science: a lunar perspective.* Vol. 3303. Houston: Lunar and Planetary

1392   Institute, (1982).

1393

1394   Trail, D., Watson, E.B. and Tailby, N.D.(2011). The oxidation state of Hadean magmas and implications

1395   for early Earth's atmosphere. Nature. 480, 73-75.

1396

1397   Trail, D., Watson, E.B. and Tailby, N.D. (2012). Ce and Eu anomalies in zircon as proxies for the oxidation

1398   state of magmas. Geochimica et Cosmochimica Acta. 97, 70-87.

1399

1400   Trail, D., Tailby, N.D., Lanzirotti, A., Newville, M., Thomas, J. and Watson, E.B. (2015). Redox evolution of

1401   silicic magmas: insights from XANES measurements of Ce valence in Bishop Tuff zircons. Chemical

1402   Geology. 402, 77-88.

1403

1404   Tollari, N., Toplis, M.J. and Barnes, S.-J. (2006). Predicting phosphate saturation in silicate magmas: An

1405   experimental study of the effects of melt composition and temperature. Geochimica et Cosmochimica

1406   Acta. 70, 1518-1536.

1407

1408   Wakita, H., Schmitt, R.A. and Rey, P. (1970). Elemental abundances of major, minor and trace elements

1409   in Apollo 11 lunar rocks, soil and core samples. Proceedings of the Apollo 11 Lunar Science Conference.

1410   2, 1685-1717.

1411

1412   Walker, D., Grove, T.L., Longhi, J., Stolper, E.M. and Hays, J.F. (1973). Origin of lunar feldspathic rocks.

1413   Earth and Planetary Science Letters. 20, 325-336.

1414

1415   Wänke, H. Palme, H., Baddenhausen, H., Dreibus, G., Jagoutz, E., Kruse, H., Palme, C., Spettel, B.,

1416   Teschke, F. and Thacker, R.(1975). New data on the chemistry of lunar samples: Primary matter in the

1417   lunar highlands and the bulk composition of the moon. Proceedings of the 6th Lunar Science

1418   Conference.2, 1313-1340.

1419

1420   Warren, P.H., Afiattalab, F. and Wasson, J.T. (1978). Investigation of unusual KREEPy samples: Pristine

1421   rock 15386, Cone Crate soil fragments 14143, and 12023, a Typical Apollo 12 soil. Proceedings of

1422   the9[th]Lunar and Planetary Science Conference. 653-660.

1423

1424   Watson, E.B. (1979).Apatite saturation in basic to intermediate magmas. Geophysical Research Letters.

1425   6, 937-940.

1426

1427   Watson, E.B. 1980. Apatite and phosphorus in mantle source regions: An experimental study of

1428   apatite/melt equilibria at pressure to 25 kbar. Earth and Planetary Science Letters. 51, 322-335.

1429

1430   Watson, E.B. and Green, T.H. 1981. Apatite/liquid partition coefficients for the rare earth elements and

1431   strontium. Earth and Planetary Science Letters. 56, 405-421.

1432

1433   Watson, E.B., Harrison, T.M. 1983. Zircon saturation revisited: temperature and composition effects in a

1434   variety of crustal magma types. Earth and Planetary Science Letters. 64, 295-304

1435

1436   Wieczorek, M.A., Jolliff, B.L., Khan, A., Pritchard, M.E., Weiss, B.P., Williams, J.G., Hood, L.L., Righter, K.,

1437   Neal, C.R., Shearer, C.K., McCallum, I.S., Tompkins, S., Hawke, B.R., Peterson, C., Gillis, J.J. and Bussey, B.

1438   (2006). The Constitution and structure of the lunar interior. Reviews in Mineralogy and Geochemistry.
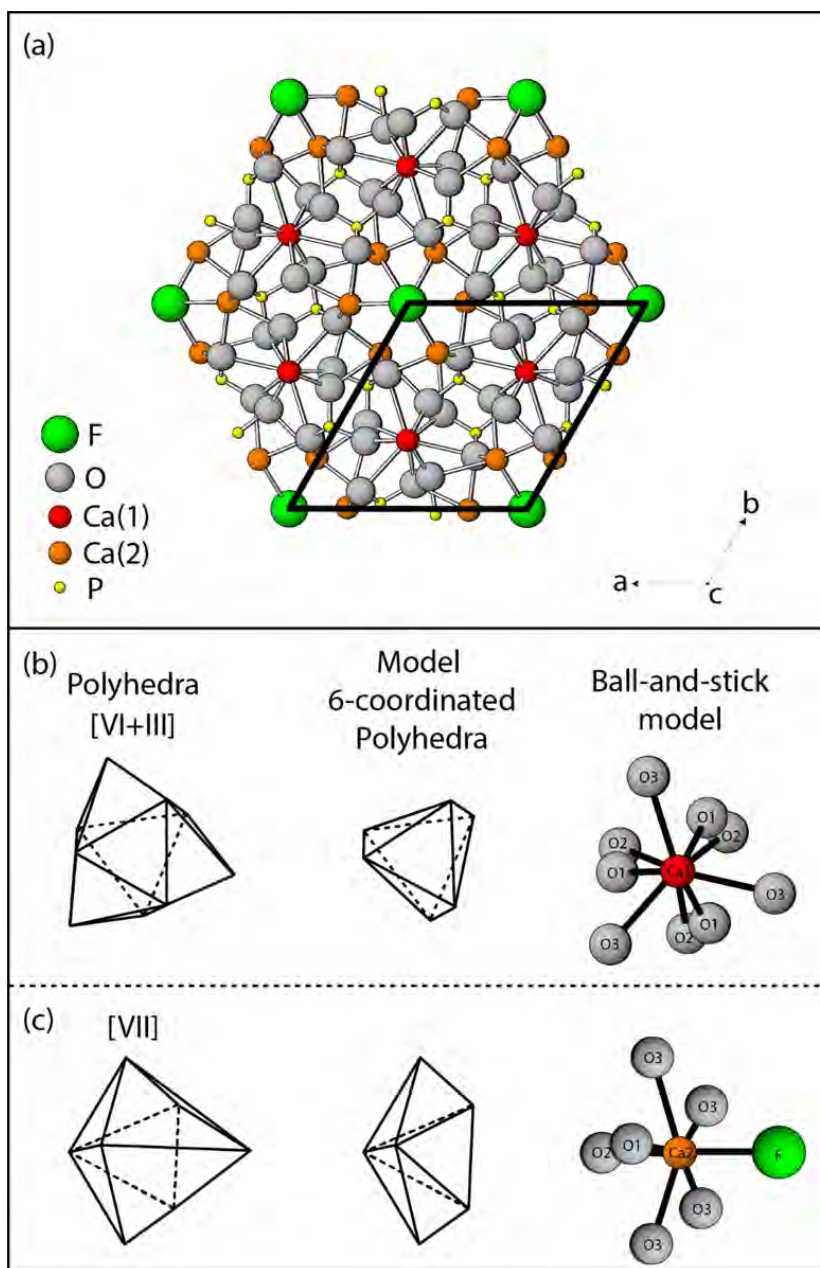
1439   60, 221-364.

1440

1441   Xing, L., Trail, D. and Watson, E.B. 2013. Th and U partitioning between monazite and felsic melt.

1442   Chemical Geology. 358, 46-53.

1443

1444   **Tables now attached in .xls format**

1445

1446

1447

Figure 1: (a) [001] projection of the apatite structure differentiating Ca(1) (red) and Ca(2) (orange) cation sites (image modified after Hughes and Rakovan, 2015). Unit cell indicated by heavy black line. (b) 9-coordinated or [VI+III]Ca(1) site, simplified 6-coordinated Ca(1) model and ball-and-stick model. (c) 7-coordinated or [VII]Ca(2) site, simplified 6-coordinated Ca(2) model and ball-stick model.

1452
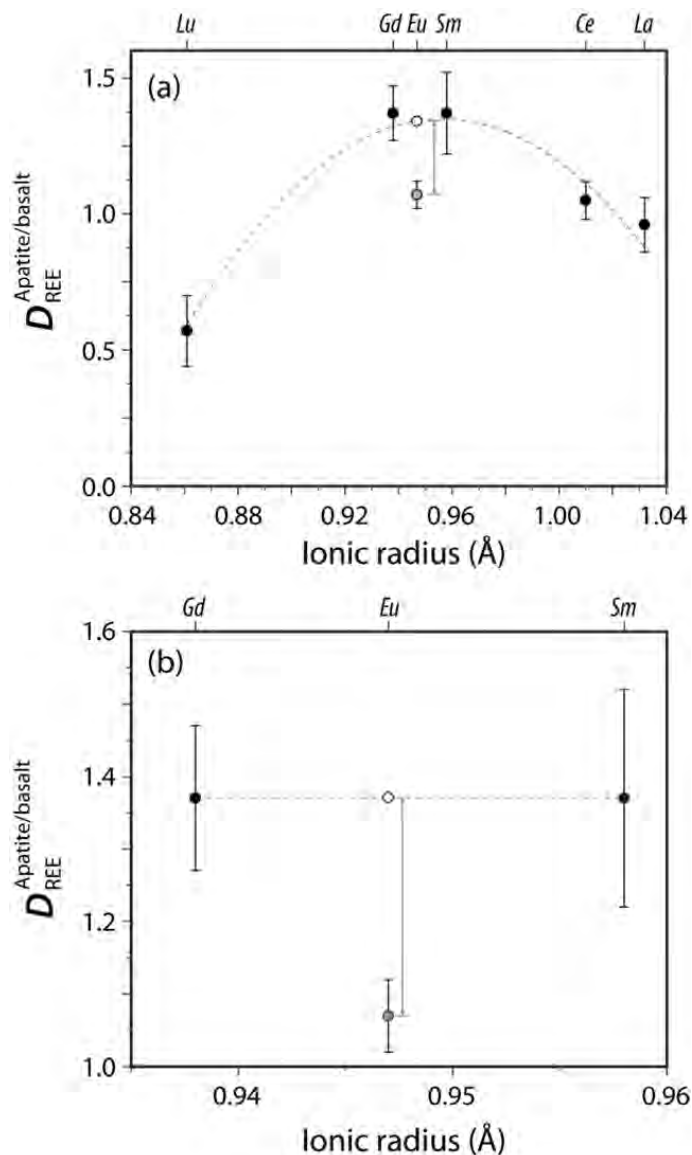
1453

1454

Figure 2: Demonstration of the two EPMA-based techniques used to calculate $(Eu/Eu^*)_D$ in this study as shown from experiment ApREE-03b (Mo-MoO$_2$ buffer) and described by *Equations 13* and *14*. (a) the lattice strain parabola (dashed curve) - fit to La, Ce, Sm, Gd and Lu data - can be used to constrain the partition coefficient for Eu^{3+}; i.e., a scenario where only trivalent Eu is present in the silicate melt. In this calculation $(Eu/Eu^*)_D$ is defined as the measured Eu content (grey circle) divided by the theoretical Eu^{3+} content of a monovalent Eu^{3+}-bearing system defined by the lattice strain parabola (white circle). (b) the $(Eu/Eu^*)_D$ defined by neighboring REE - Gd and Sm. The numerator or $D_{Eu}^{Apatite/basalt}$ in this calculation is directly measured (grey circle),while the denominator or $\left(\sqrt{D_{Sm}^{Apatite/basalt} \times D_{Gd}^{Apatite/basalt}}\right)$(white symbol) is calculated from Sm and Gd measurements. In this type of calculation $(Eu/Eu^*)_D$ is represented by the ratio defined by grey arrow between numerator and denominator. All black symbols correspond

1465   to isovalent elements measured from this experiment (including Ce, as Ce^{4+} appears to be highly

1466   incompatible in apatite) that can be used to define the REE^{3+}Onuma diagram. Note that all ionic radii

1467   assume 6-coordination (see text, Klemme and Dalpé, 2003 for details).
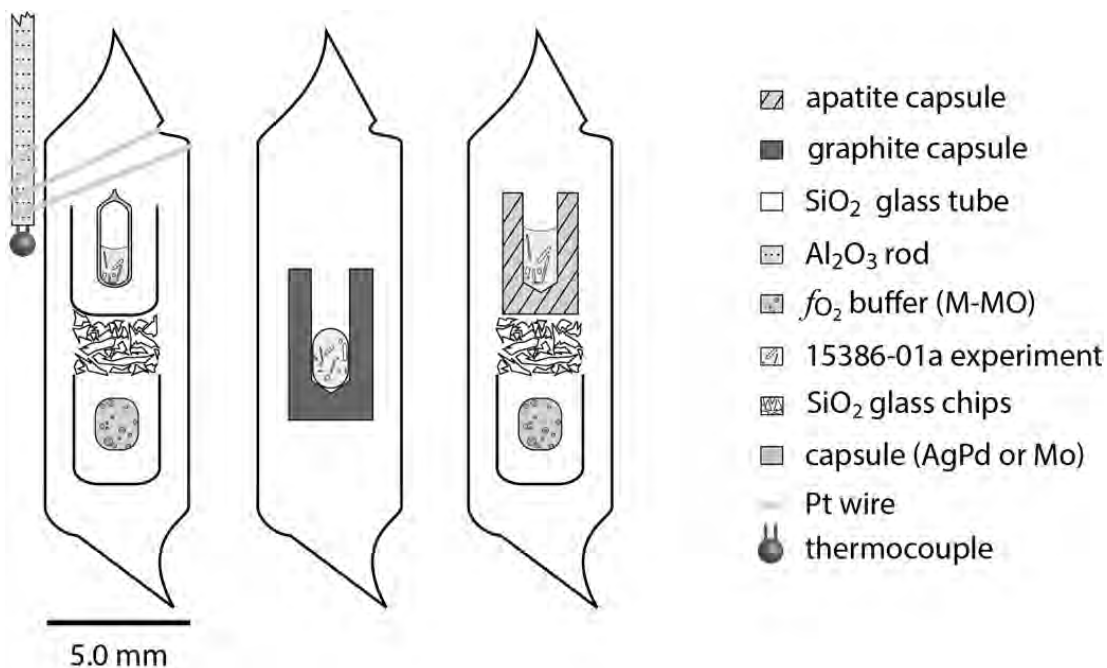
1468

1469

1470

1471

1472

1473 **Figure 3**: Experimental setup for ApREE experiments. Note that M-MO buffer represents a metal-metal
1474 oxide solid state f_{O_2} buffer (e.g., Ni-NiO). Note that left-hand and right-hand capsules include nested
1475 solid state buffers, while the middle experiment example includes a participatory buffer capsule
1476 (graphite).

1477

1478

1479

1480

1481

1482

74

1483

1484

1485
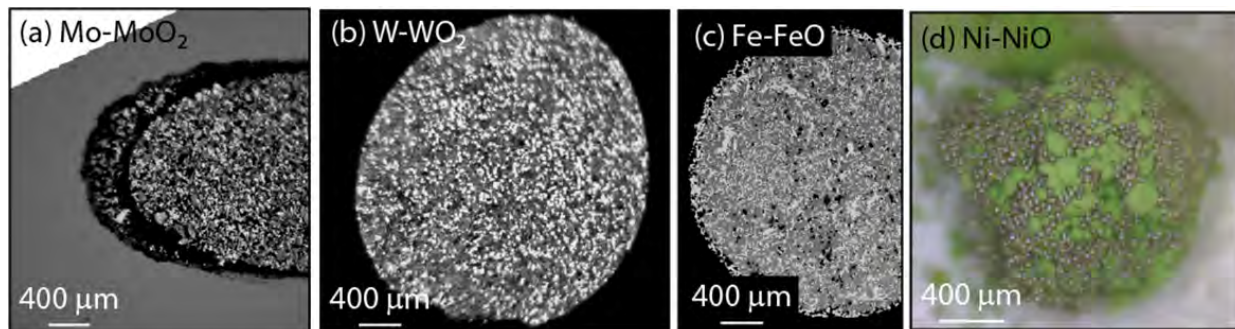
1486

1487 **Figure 4**: Post-experiment images from different solid state f_{O_2} buffers. (a)-(c) BSE images from
1488 experiments ApREE-07 (Mo-MoO$_2$), ApREE-13b (W-WO$_2$), ApREE-06 (Fe-FeO). In all examples the bright
1489 phase represents the metal compound and the lower BSE intensity (grey) material represents the metal
1490 oxide compound. (d) Optical photomicrograph from ApREE-01a (Ni-NiO), where NiO is shown in green
1491 and Ni metal in small metallic balls.

1492

1493
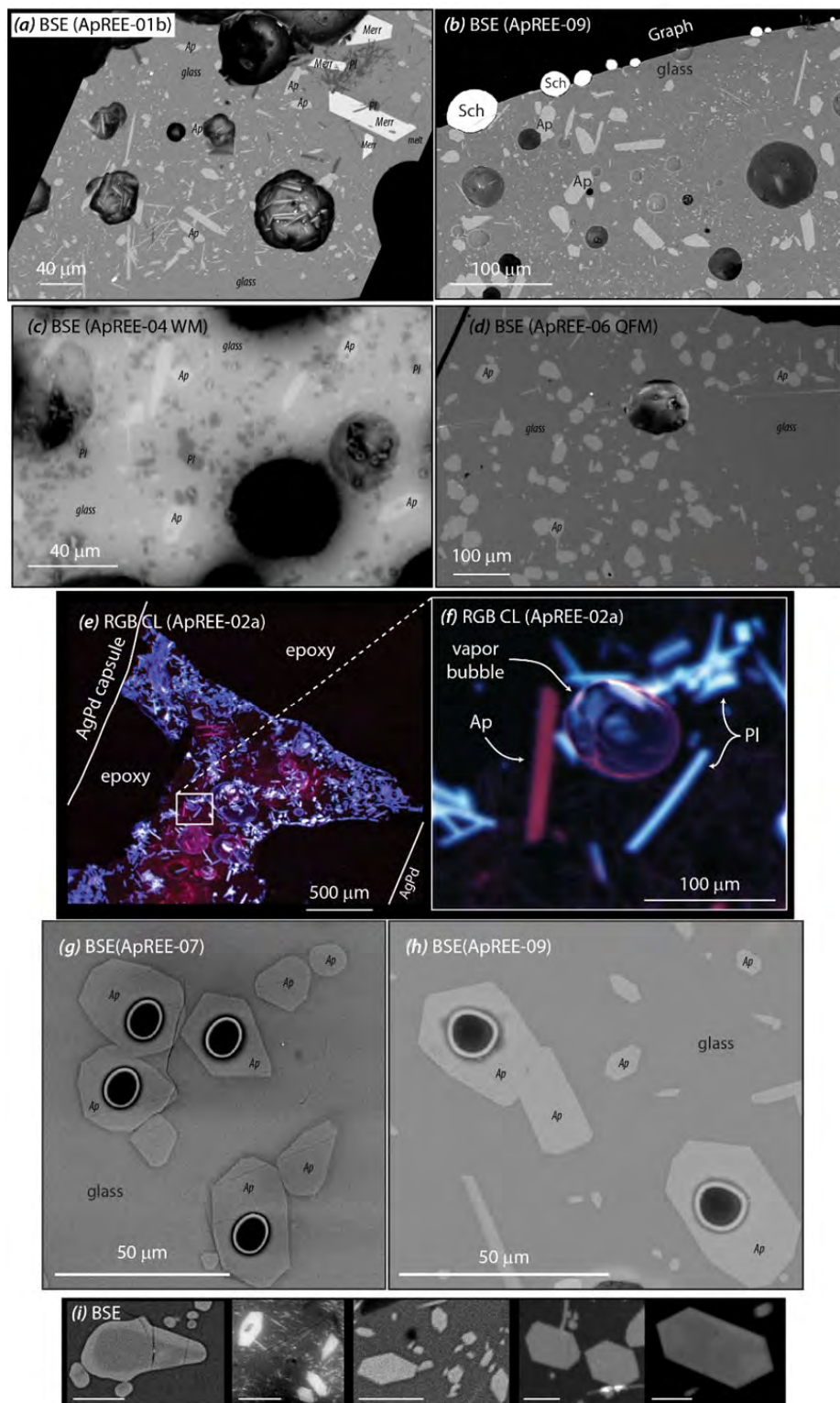
1494

Figure 5: Representative photomicrographs of experimental run products. (a)-(d) BSE images from experiments, Ap = apatite, Pl = plagioclase feldspar, melt = basaltic glass, Sch = schreibersite and Merr = merrillite. (e)-(f) Cathodoluminescence (CL) image from combined red-green-blue (RGB) filters from

1498   experiment ApREE-02a. Note the different phases present within experimental charges are easily

1499   distinguished by the wavelength of luminescence (i.e., experimental plagioclase crystals tend to

1500   luminesce at blue wavelengths, while apatites luminesce at red wavelengths). (g)-(h) Representative BSE

1501   images taken over LA-ICP-MS spots from experimental runs, note: the locus of the laser spot within

1502   apatite crystals. (i) BSE or grayscale CL from apatite crystals from various experiments showing the

1503   crystal habit from left-to-right: ApREE-01b (NNO), ApREE-03 (WM), ApREE-01a (NNO), ApREE-06 (QFM)

1504   and ApREE-12 (WM). Scale bar for BSE images in (i) are all 20 μm. Note that all experiments, with the

1505   exception of ApREE-01b which shows apatite seeds from the apatite capsule, show sharp euhedral habit

1506   indicative of equilibrium growth.

1507

1508

1509
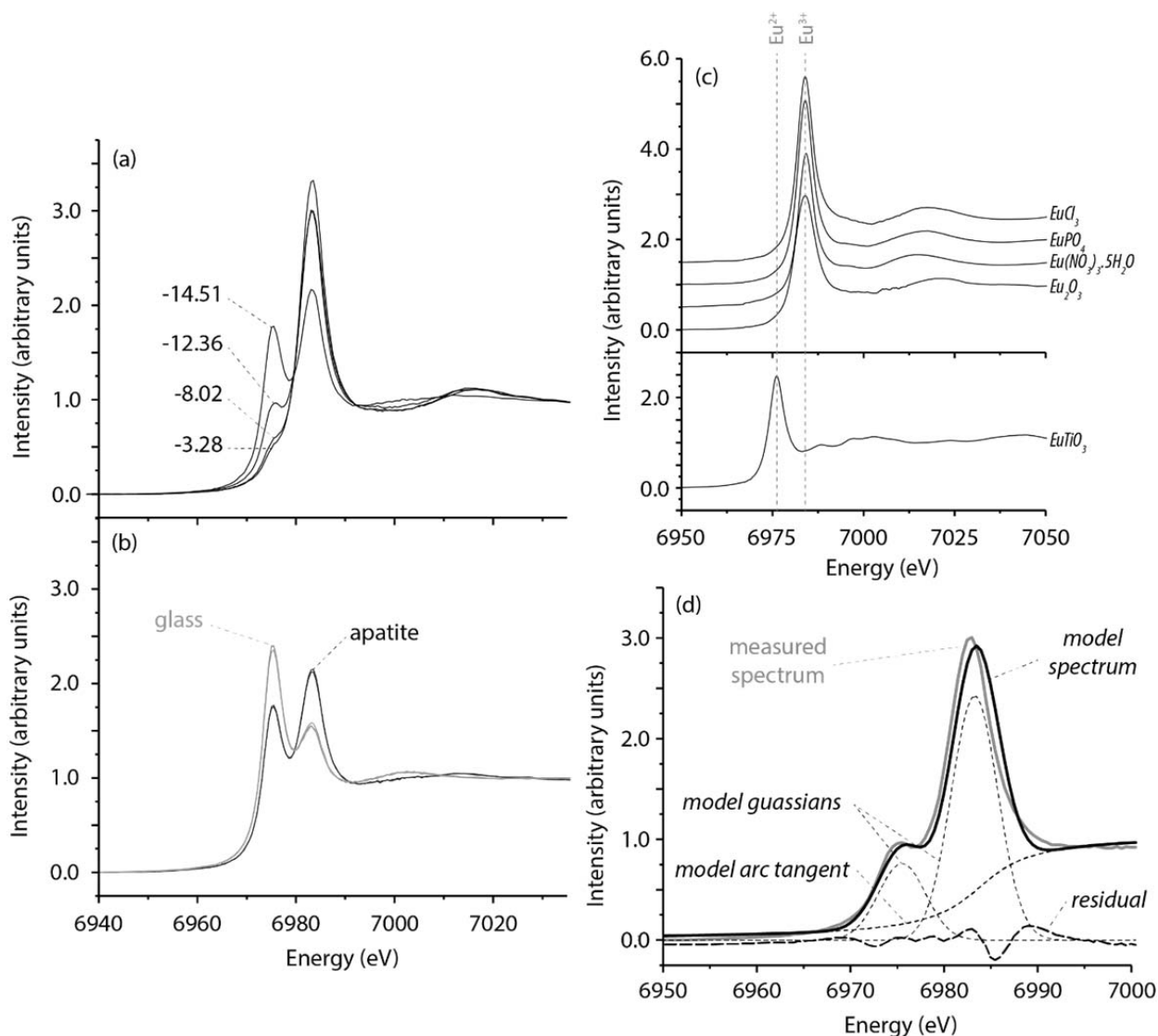
1510

Figure 6.1: Normalized Eu L_3 XANES features from experiments. (a) Spectra from representative apatite experiments, where numerical values correspond to different $\log(f_{O_2})$ defined in the experimental charge. (b) L_3 XANES spectra from co-existing glass (in grey) and apatite (in black) from experiment ApREE-07 (Mo-MoO$_2$, $\log(f_{O_2})$= -12.36). (c) L_3 XANES spectra from standard Eu compounds measured in transmission mode. Note the dominant white line for Eu^{2+} (measured here on EuTiO$_3$) exists at lower energy (6975.5 eV) and normalized intensity (~2.5 arbitrary units) than Eu^{3+} compounds (here measured on EuPO$_4$, EuCl$_3$, Eu(NO$_3$)$_3$·5H$_2$O, Eu$_2$O$_3$; with a normalized intensity between 3.0-3.5 arbitrary units). Note that individual Eu standards in (c) are stepped by 0.5 units for clarity. (d) Least squares regression from XANES spectrum from experiment ApREE-06 (QFM), where the edge-step is approximated by an arc tangent, Eu^{2+} and Eu^{3+} components are modeled as Gaussians and the residual are plotted.

1521
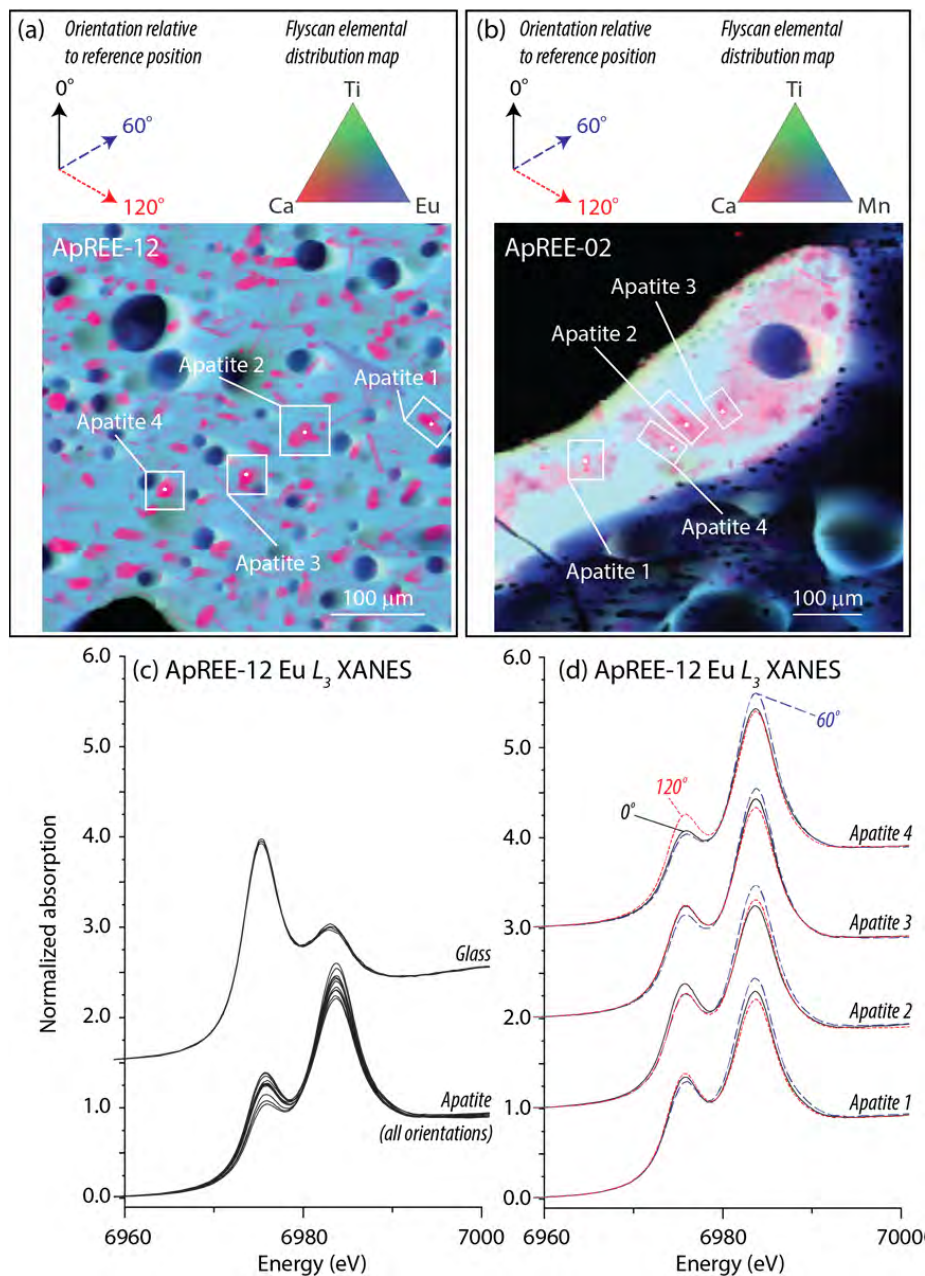
1522

Figure 6.2: Representative and normalized Eu L_3 XANES orientation scans from experiments (a) ApREE-
12 and (b) ApREE-02. Reference orientation for flyscan image is at 0° (i.e., north position). Rotations
indicated by arrows in (a) and (b) match color-coded spectra in (d), with rotation indicated by arrows or
degree symbols. RGB ternary image corresponds to X-ray fluorescence maps involving Ti Kα, Ca Kα and
Eu Lα lines, making it possible to identify and distinguish regions of glass/apatite for analysis. Glass
regions generally represented by light blue hues while apatite grains are represented by red-pinkish
hues. Eu L_3 XANES features from oriented experiments, where (c) corresponds to all glass and apatite
analysis from experiment ApREE-12, and (d) corresponds to the 4 individual apatite crystals measured at
the 3 reference orientation (0° in solid black curves, 60° in large dashed blue curves and 120° in short
red dashed curves). Note that the syn-KREEP 15386-01a glass records almost no observable orientation

79

1533   effect because it is isotropic, while apatite shows very minor variations due to the anisotropic nature of
1534   the crystal structure.

1535
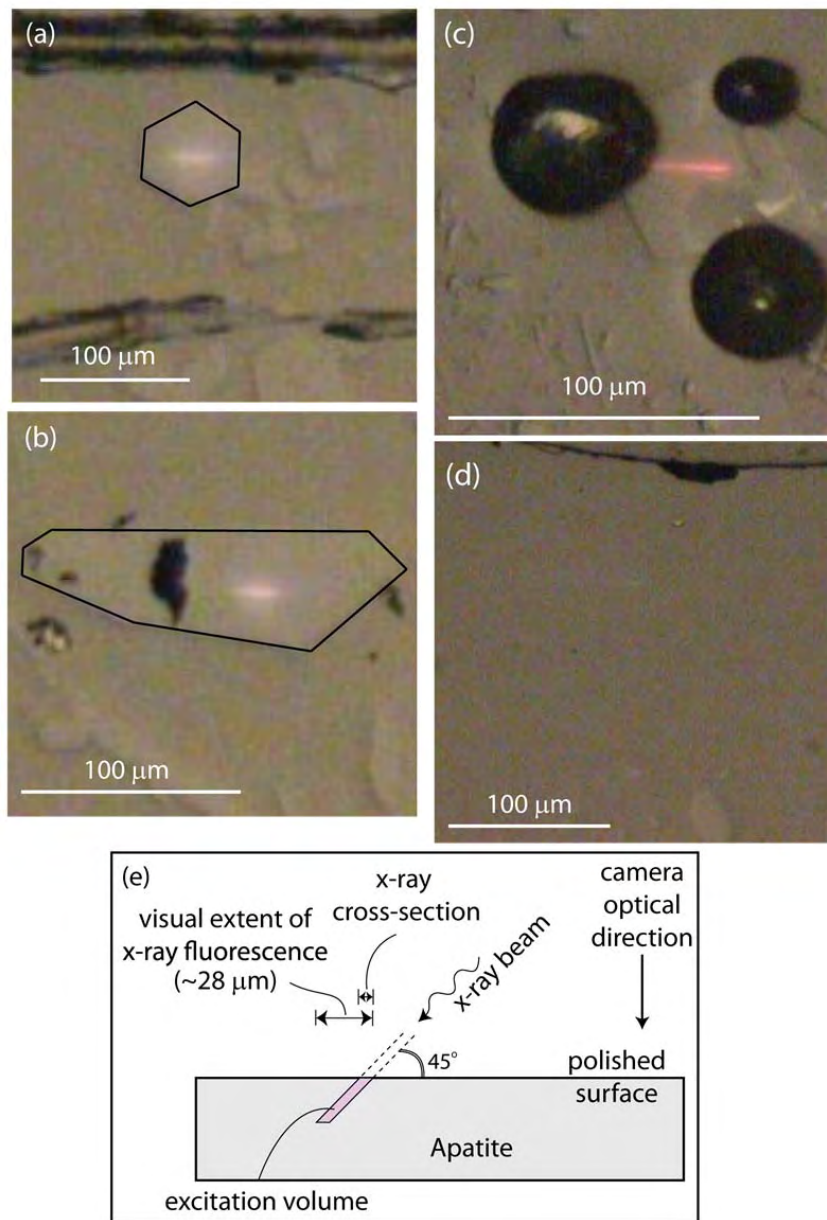
1536

Figure 7: Optical luminescence observed from ApREE experiments, with the incident X-ray beam
approaching the sample from 45° to the right. (a) Blue to purple luminescence observed within apatite
crystal in ApREE-15X with analysis carried out on crystal polished perpendicular to the c-axis. (b) Blue
luminescence from ApREE-15X conducted on apatite crystal near-parallel to the c-axis (c) Red
luminescence observed in merrillite from experiment ApREE-01a. (d) Very limited optical luminescence
observed on glass from ApREE-09. (e) Diagram illustrating the relationship between the focused beam
(2x2 µm at the crystal surface) and X-ray absorption path. The observed X-ray fluorescence in

1544   apatite/merrillite (~28 μm) is close to2 absorption lengths (49.2/2=24.7 μm; where the division accounts

1545   for the 45° angle of the sample) as predicted by Hephaestus.

1546

1547
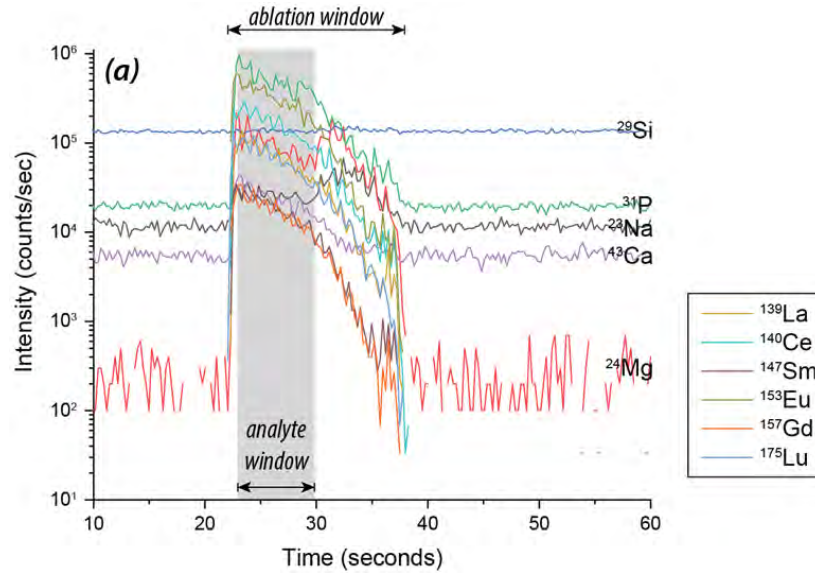
1548

1549   **Figure 8:** Time-resolved LA-ICP-MS analysis from apatite in experiment ApREE-03a. Note the lack of Si
1550   counts in the time-resolved spectra (when combined with BSE observations from the locus of ablation)
1551   indicating clean apatite analysis.

1552
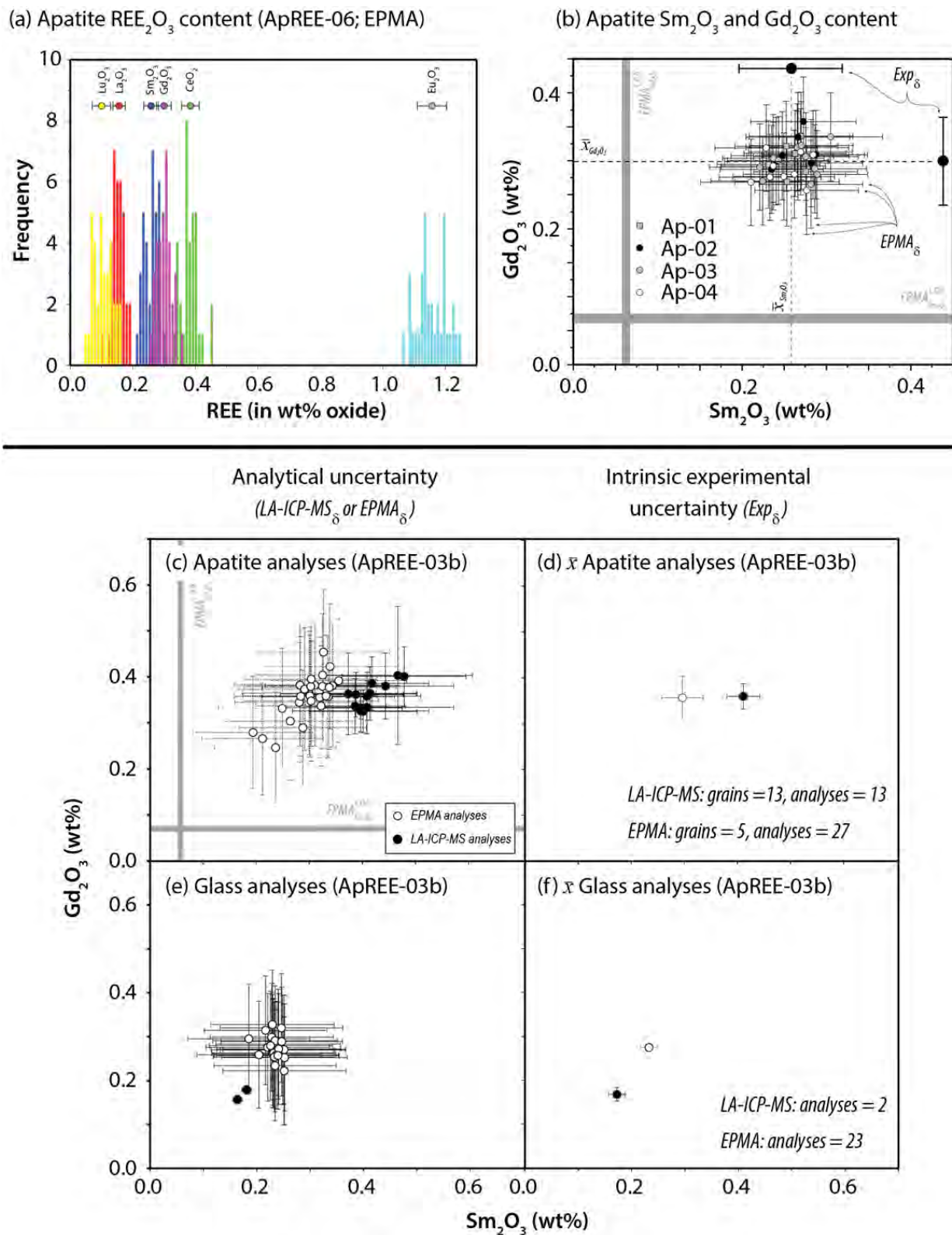
1553

Figure 9: (a) Frequency distribution histograms for individual REE oxides based on 34 REE EPMA analyses
from 4 apatite grains in experiment ApREE-06 (QFM). Note that each REE shows a normal distribution,

83

1556   with the average and 1σ projected. (b) Sm_2O_3 and Gd_2O_3 analyses from different synthetic apatite grains

1557   from experiment ApREE-06 (QFM). Different symbols correspond to analyses from a single grain, error

1558   bar in 1δ and shaded grey region corresponds to range of detection limit from all analyses. Note the

1559   clustering of data demonstrates almost no inter-grain variation in Gd- and Sm-content, arguably among

1560   the two most important elements when constraining Eu/Eu*, is observed in experiments. (c) and (e)

1561   comparison of EPMA data (with analytical uncertainty; open circles with error bars) and LA-ICP-MS data

1562   (solid circles with error bars) for both apatite and glass. Note that EPMA detection limit as indicated and

1563   LA-ICP-MS detection limit (at ppb levels) essentially correspond to the origin of the graph. (d) and (f)

1564   Intrinsic, inter-grain or inter-glass uncertainty from repeat analyses from an experimental charge.

1565

1566

1567

1568
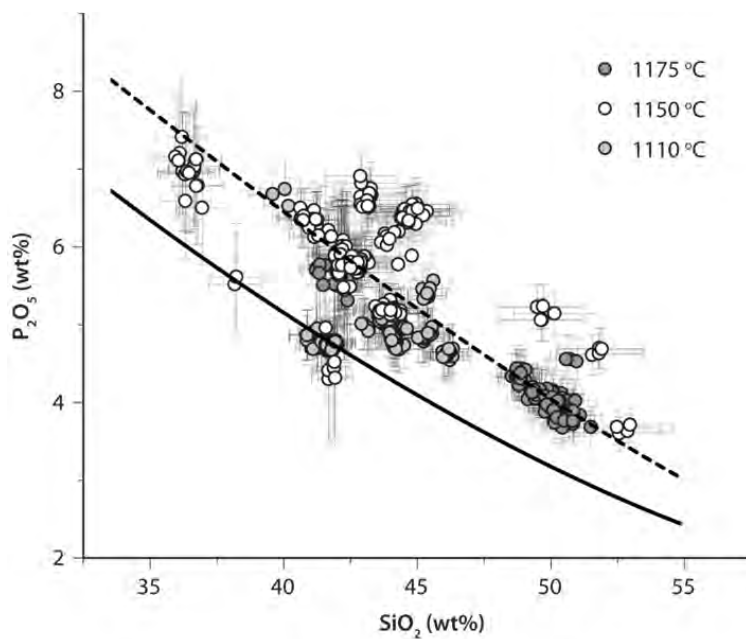
1569

1570   **Figure 10**: Measured SiO_2 vs P_2O_5 of experimental glasses from this study. Solid curve corresponds to the
1571   1165 °C apatite saturation curve and the dashed curve corresponds to the 1200 °C apatite saturation
1572   curve defined by the f_{O_2} buffered experiments of Watson (1979). Symbols as indicated and error in 2σ.

1573

1574

1575

1576

1577
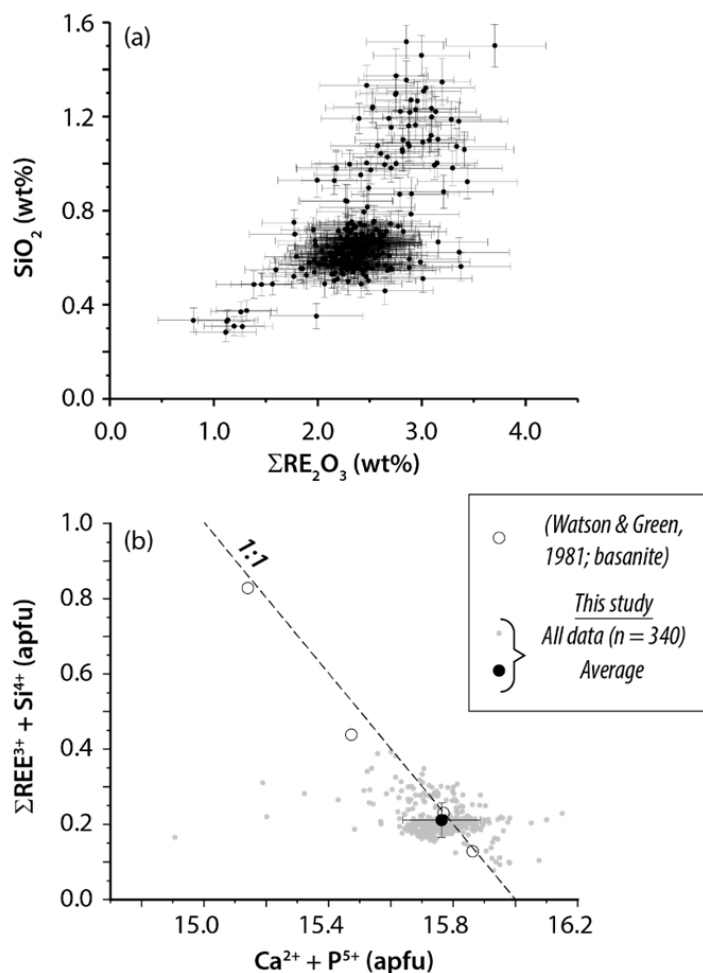
1578

1579

1580 **Figure 11:** (a) ΣRE_2O_3 (assuming CeO_2 and EuO components are negligible, which is consistent with
1581 partitioning data, XANES measurements and Eu/Eu* data) versus SiO_2 content of experimental apatite
1582 crystals. Error bars are in 2σ. (b) Calculated 'REE+Si' versus 'Ca+P' projection in atoms per formula unit
1583 (apfu) for all experimental apatite from this study (light grey circles), average from all experiments from
1584 this study (with 1δ; solid black circle) and measured compositions from comparable REE partitioning
1585 data in mafic apatite-silicate melt experiments by Watson and Green (1981; open circles). Note the
1586 dashed 1:1 curve corresponds to the coupled substitution of $REE^{3+} + Si^{4+} = Ca^{2+} + P^{5+}$. Calculations are
1587 based on 25 oxygens and assume only Eu^{3+} and Ce^{3+} are present.

1588

1589
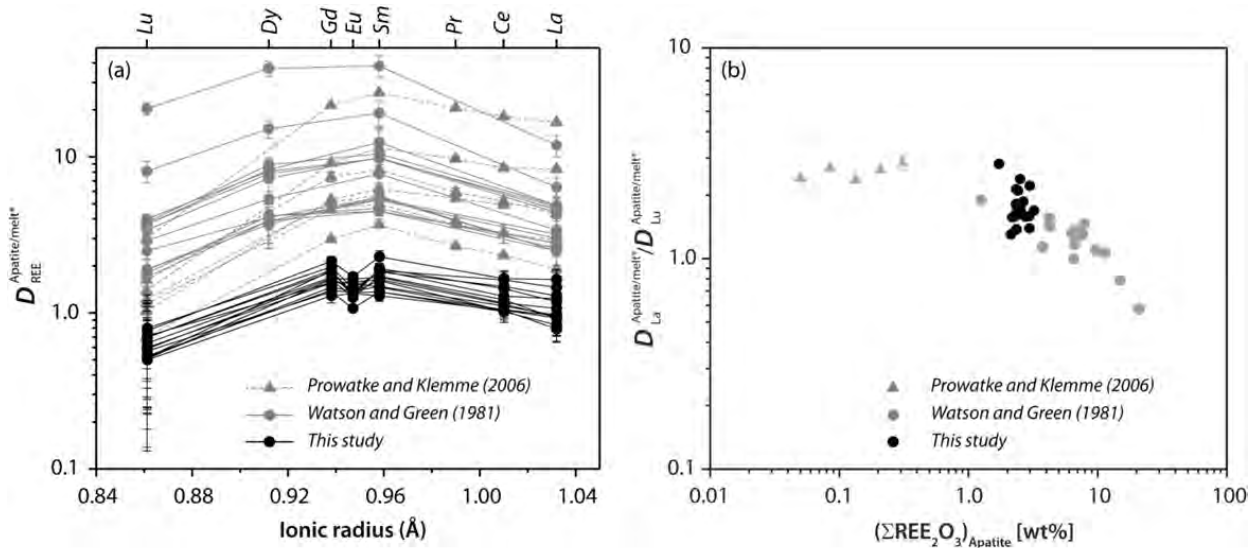
1590

1591 **Figure 12**: (a) Comparison of apatite/silicate melt partition coefficients from this study (ApREE
1592 experiments shown by black symbols curves); Watson and Green (1981, shown by grey circles and solid
1593 grey curves), and; Prowatke and Klemme (2006, shown by grey triangles and dashed grey curves). (b)
1594 Bulk REE content of apatite versus $D_{La}^{Apatite/melt}/D_{Lu}^{Apatite/melt}$ (or LREE:HREE), symbols as in (a). Note:
1595 melt* is used because previous studies (Watson and Green, 1981; Prowatke and Klemme, 2006) include
1596 a range of silicate melt types (i.e., not strictly basalt).

1597

1598
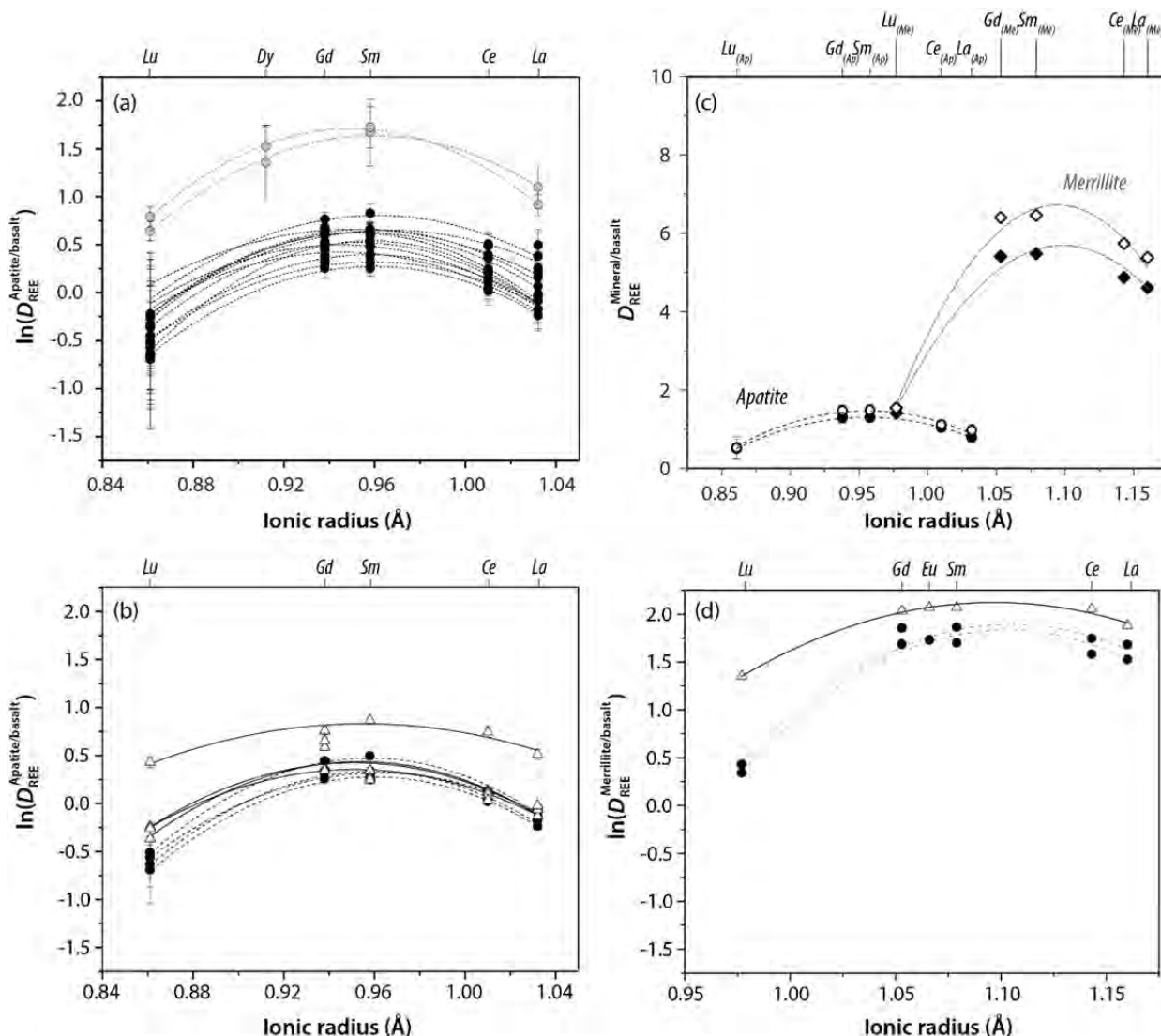
1599

Figure 13: Lattice strain model fits from experiments. (a) REE^{3+} partition coefficients with lattice strain models from apatite in all individual experiment data of monovalent $^{[VI]}REE^{3+}$ from this study (black circles), compared with data reported from basanite and tholeiitic andesite by Watson and Green (1981). Note that Ce is included in the model dataset because partitioning data indicates no influence from Ce^{4+} over the observed experimental conditions. Error bars reported in 1σ or where absent smaller than symbols. (b) REE^{3+} partition coefficients with lattice strain models from apatite four representative experiments using both EPMA (closed circles, dashed lattice strain curve) and LA-ICP-MS (open triangles, solid lattice strain curve) techniques. Note the two techniques record similar partitioning values, similar error and similar lattice strain model topology. (c) Lattice strain fits from experiments containing co-existing apatite and merrillite (ApREE-01a and ApREE-04), showing relative REE^{3+} partitioning among the two phosphate phases co-existing with basalt (diamonds correspond to merrillite and circles correspond to apatite). Note data obtained from EPMA, while merrillite ionic radii correspond to 8-coordinated sites of the dominant Ca sites within the mineral with elements in the Figure including La, Ce, Sm, Gd, and Lu (from right to left).

88

1614

1615   (d) REE^{3+} partition coefficients with lattice strain models from merrillite based on EPMA (including
1616   experiments ApREE-01a and ApREE-04, solid circles, dashed curves) and LA-ICP-MS (experiment ApREE-
1617   03a, open triangles, solid curve). Note that though the two techniques show similar topology and error,
1618   though direct comparison of data is not possible.

1619
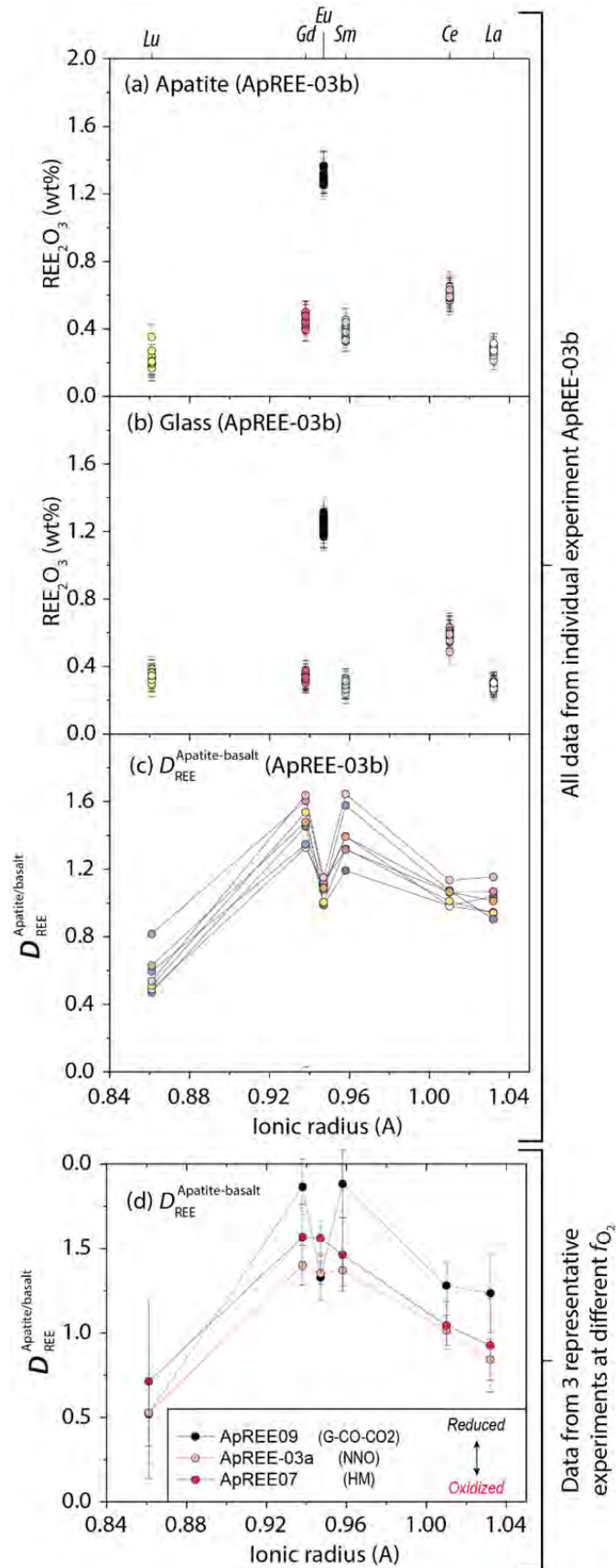
1620

1622   **Figure 14:** (a) Raw EPMA data from experiment ApREE-03b glass analyses, where colors correspond to
1623   individual REE_2O_3 (yellow = Lu_2O_3, salmon = Gd_2O_3, black = Eu_2O_3, green = Dy_2O_3, pink = Ce_2O_3 and white
1624   = La_2O_3. The reported uncertainty (δ) on data points represents the intrinsic error to the EPMA setup
1625   and is based on counting statistics. Also note that n=21 from this experiment. (b) raw EPMA data from
1626   apatite from the same experiment ApREE-03b, where REE_2O_3 colors are consistent with previous figure,
1627   and n=8. (c) Individual, apatite-glass partition data from experiment ApREE-03b, where color represents
1628   a given apatite-glass analytical pair used to make Eu/Eu* calculations (n=8). (d) Apatite/basalt partition
1629   coefficients as determined by EPMA from a series of isothermal (1150 °C) experiments equilibrated at
1630   different redox buffers. Note the intensity of the negative Eu anomaly (or Eu/Eu*)$_D$ increases with
1631   decreasing [$\log(f_{O_2})$]. HM = hematite-magnetite buffer [$\log(f_{O_2})$=-3.28], Ni-NiO buffer [$\log(f_{O_2})$=-8.31],
1632   and graphite-CO-CO_2 buffer [$\log(f_{O_2})$=-14.51]. Error bars reported in (d) as 1σ.

1633

1634
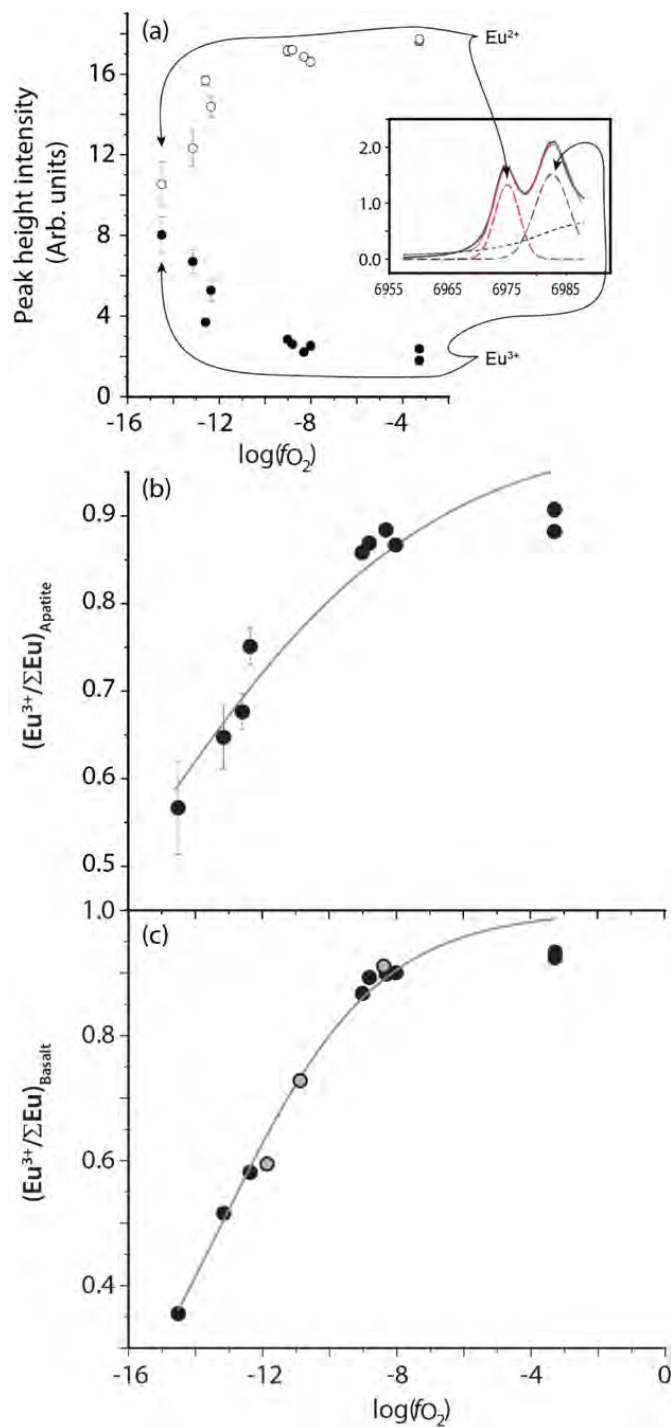
Figure 15: (a) Peak height intensity from Eu^{2+} and Eu^{3+} gaussian curves fit to apatite Eu L_3 XANES data from all experiments used to calculate $Eu^{3+}/\Sigma Eu$. Note the insert represents a single fit to an Eu L_3 XANES spectra from experiment ApREE-09 and is shown for guidance (with dashed purple curve = Eu^{2+} gaussian, dashed blue curve = Eu^{3+} gaussian, dashed black curve represents the arc tangent, solid red curve = model spectra and black curve represents measured spectrum. (b) Valence sigmoid from Eu L_3 XANES

1642   data from Table 6 fits to *eq. 11* (least squares) from in-situ analyses of (b) apatite crystals, and (c) co-
1643   existing glass from individual experiments (black circles) compared to experimental data in basalt
1644   presented by Karner et al. (2010; assuming equilibration at 1130 °C). It should be noted that the Karner
1645   et al. (2010) data was not included in the sigmoidal, least squares fit. Error reported in 1σ and where
1646   absent is smaller than symbols.

1647

1648

1649

1650

1651

1652

1653

1654

1655

1656

1657

1658

1659
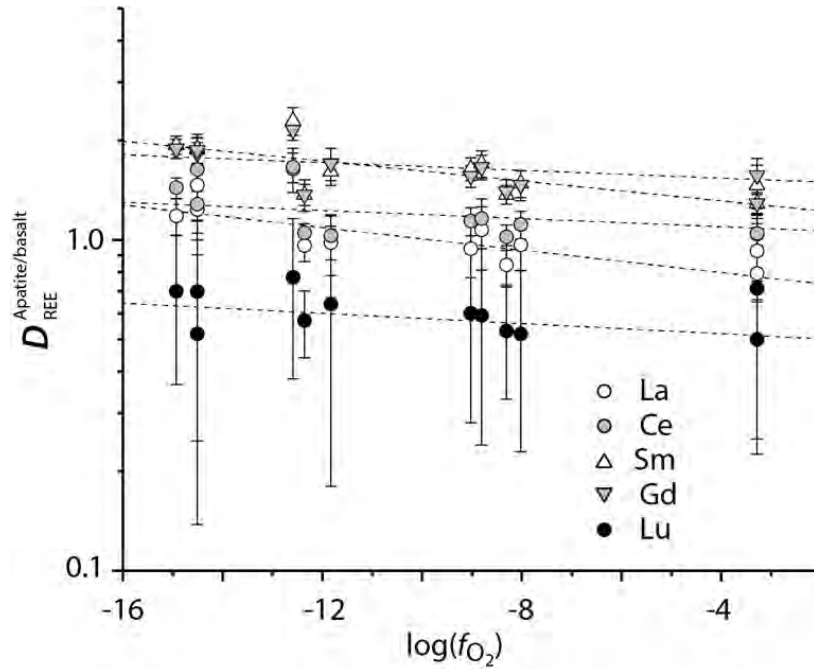
1660

Figure 16: Apatite/melt partition coefficients of isovalent REE^{3+} at various f_{O_2} as determined by EPMA (noting that while Ce is polyvalent, the data indicate only Ce^{3+} is compatible in apatite; see text). Linear regressions for individual elements are represented by sub-horizontal dashed curves and error bars represent 1σ. Note: the near constant partition coefficient observed among the isovalent REE^{3+} demonstrates these elements are unaffected by f_{O_2} over the experimental range. Symbols as indicated; uncertainties are +/- 1σ.

1667

1668

1669

1670

1671

94

1672
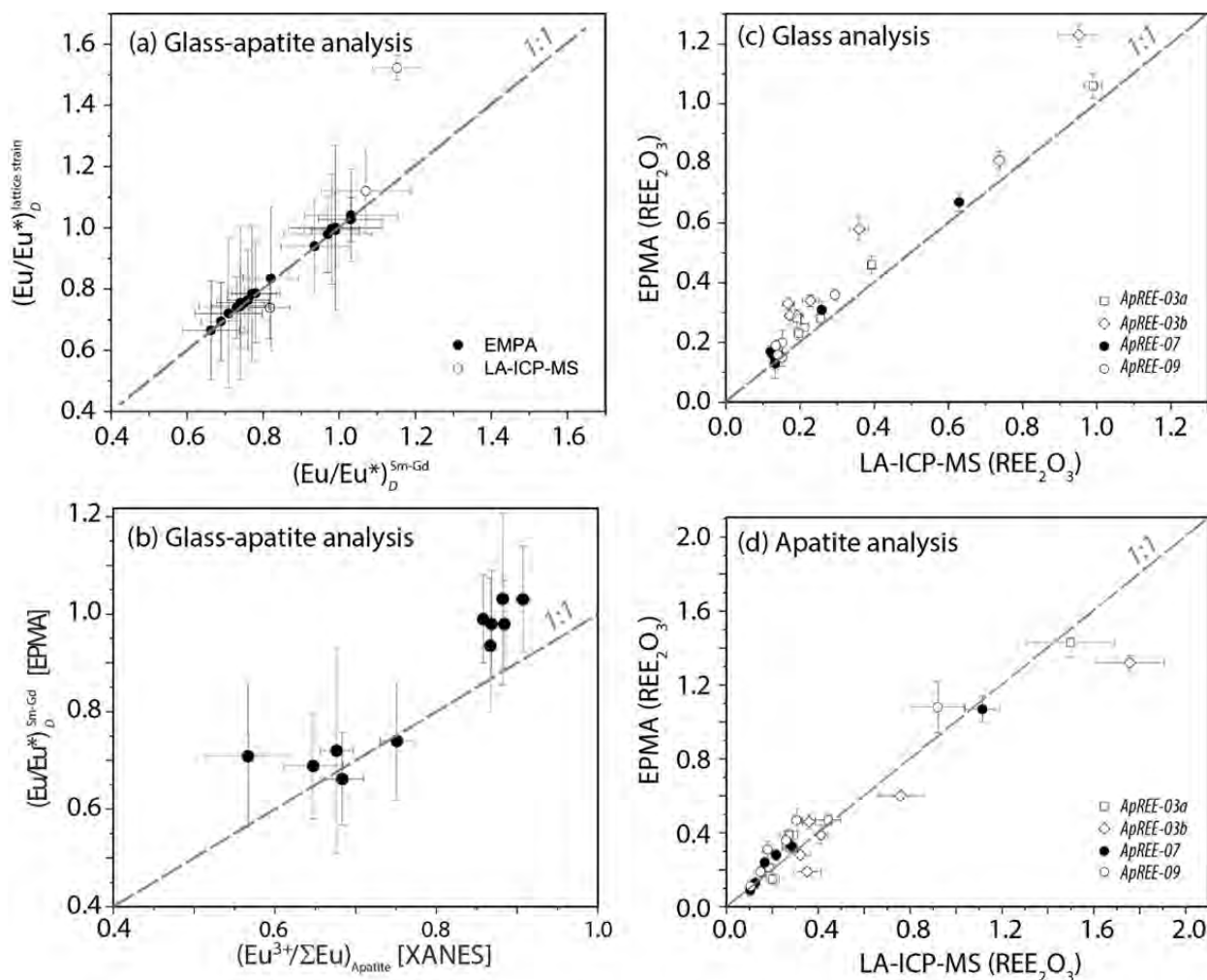
1673

1674

1675   **Figure 17**: (a) Comparison of (Eu/Eu*) in apatite as determined by lattice strain (i.e., $\left(\frac{Eu}{Eu^*}\right)_D^{lattice\ strain}$)

1676   versus (Eu/Eu*) as determined by the concentration of neighboring REEs Sm-Gd (i.e., $\left(\frac{Eu}{Eu^*}\right)_D^{Sm-Gd}$). Open

1677   symbols represent LA-ICP-MS data and closed symbols represent EPMA data. (b) Comparison of

1678   (Eu/Eu*) as determined by neighboring REEs Sm-Gd versus Eu/ΣEu determined from XANES for

1679   experiments where both analytical techniques have been applied. (c) Comparison of REE concentration

1680   reported in REE_2O_3 (including La_2O_3, Ce_2O_3, Sm_2O_3, Eu_2O_3, Gd_2O_3, Lu_2O_3) analyses from glass as

1681   determined by LA-ICP-MS and EPMA. (d) Comparison of REE_2O_3 analyses (same elemental oxides as

1682   listed in Fig.15c) from apatite grains within an individual experiment as determined by LA-ICP-MS and

1683   EPMA. Error bars represent 1σ. Note: dashed curves in graphs (a) and (d) represent 1:1 curve across the

1684   two analytical techniques being compared (i.e., EPMA vs LA-ICP-MS, etc).

1685

1686

1687

1688
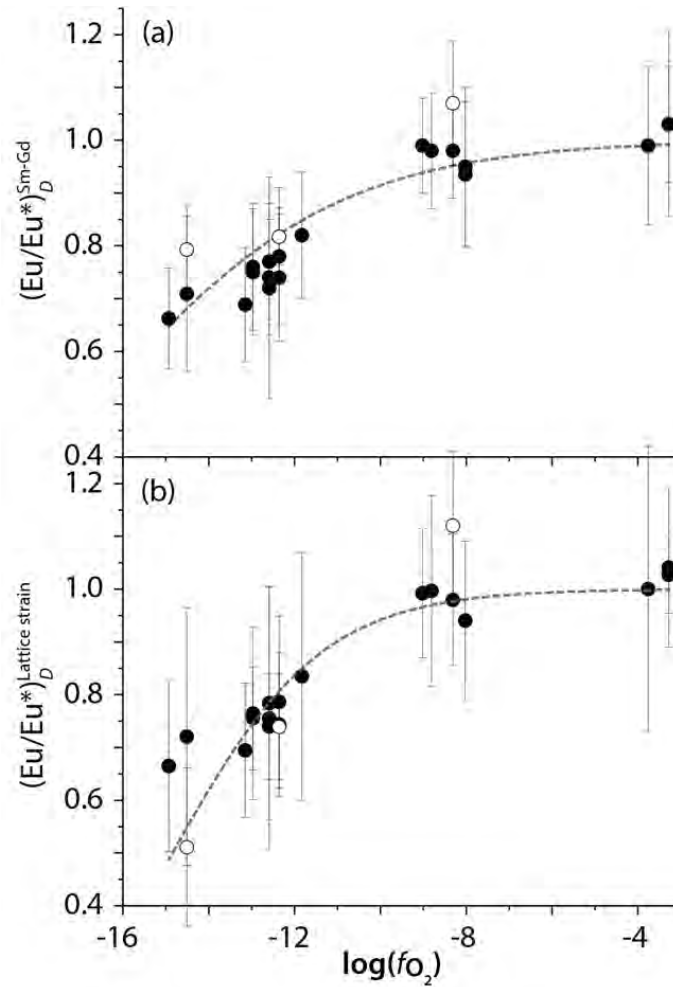
1689

1690

Figure 18: Eu valence speciation curves for apatite-basalt defined by experiments and obtained through least squares regression to data from Supplement 2. (a) $\left(\frac{Eu}{Eu^*}\right)_D^{Sm-Gd}$ calibration curve as determined by EPMA, error in 1σ. (b) $\left(\frac{Eu}{Eu^*}\right)_D^{lattice\ strain}$ calibration curve as determined by EPMA, error in 1δ. Closed circles in both figures represent EPMA data and open circles correspond to LA-ICP-MS data.

1695

1696

1697

96

1698

1699
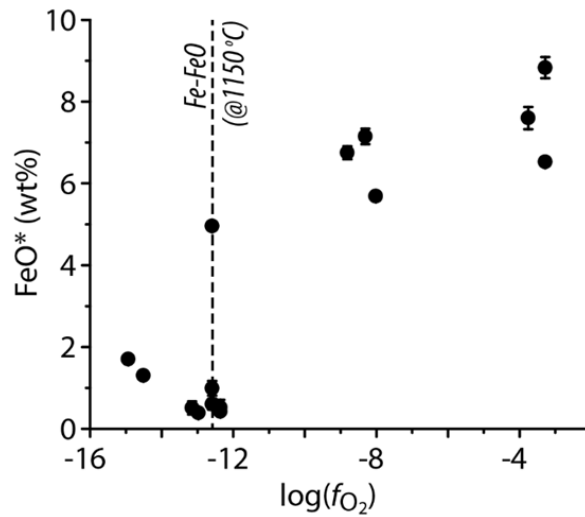
1700

Figure 19: Average FeO* from ApREE experimental glasses vs log(f_{O_2}). Note that most experiments at very reducing conditions [i.e., log(f_{O_2})<-12] report low FeO* and generally show the presence of schreibersite.

1704

1705
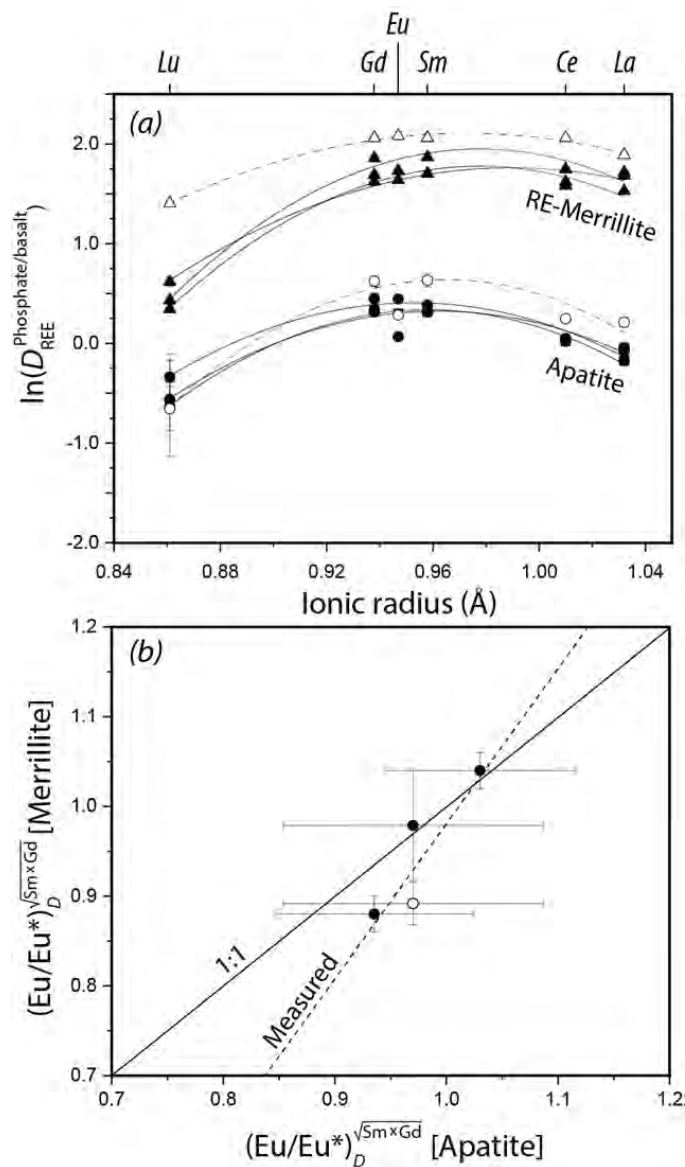
1706

Figure 20: Measured REE partition coefficients in experiments containing co-existing merrillite and apatite within syn-KREEP 15386-01a basalt. (a) Data from experiments ApREE-01a, ApREE-03a, ApREE-04 from oxidized experiments (i.e., Fe_2O_3-Fe_3O_4 or Ni-NiO buffers), where triangles correspond to RE-merrillite analyses, circles correspond to apatite analyses, open symbols represent LA-ICP-MS analyses and closed symbols represent electron microprobe analyses. Error is in 1σ. Note that ionic radii in (a) corresponds to a theoretical 6-coordinated site (as in Figure 2) and is not an accurate projection for merrillite but is used such that the two different crystal structures can be directly comparted via projection. The relative topography of the Onuma diagram and depth of the Eu anomaly in (a) can, however, be used as a guide to the relative partitioning behavior between merrillite-basalt and apatite-basalt. (b) Direct comparison of $\left(\frac{Eu}{Eu*}\right)_D^{Sm-Gd}$ or intensity of the negative Eu anomaly in co-existing

1717   merrillite and apatite for the same set of experiments (i.e., ApREE-01a, ApREE-03a and ApREE-04) with

1718   direct comparison to 1:1 curve. As in previous figure open symbols correspond to LA-ICP-MS analyses

1719   and closed symbols correspond to electron microprobe analyses.

1720

1721

1722

1723
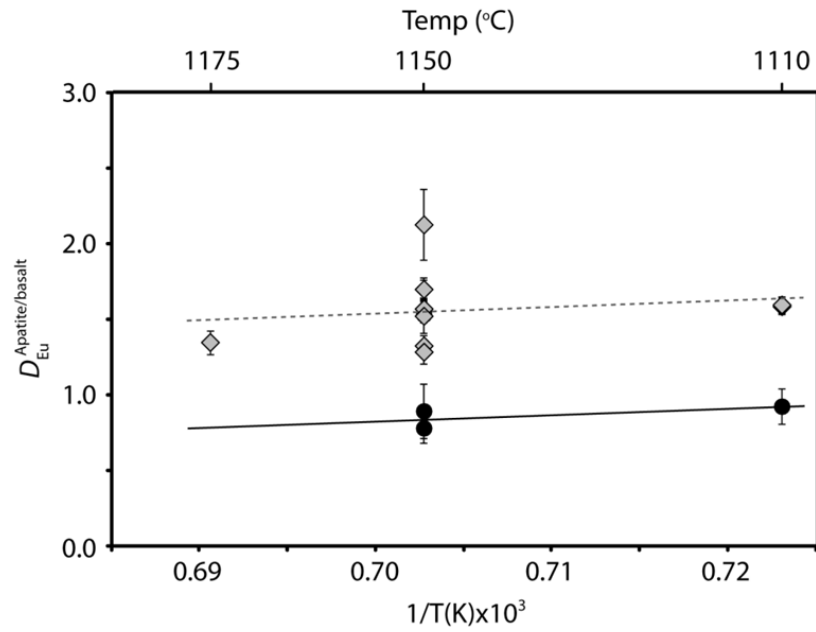
1724

1725   **Figure 21:** Linear regressions to Eu partition coefficients for Eu^{3+} (grey diamonds) and Eu^{2+} (black circles;
1726   preferred values) determined from experiments where both EPMA and Eu L_3 XANES data has been
1727   obtained. Error reported as 1σ.

1728

Table 1		15386, 19	15386, 1	15386-01a[‡]
in wt% oxide				
	SiO_2	50.28	50.83	46.31
	TiO_2	1.9	2.23	2.08
	Al_2O_3	15.3	14.77	13.98
	Cr_2O_3	0.36	0.31	n/i
	FeO	10.2	10.55	9.6
	MnO	0.15	0.16	n/i
	MgO	10.5	8.17	7.77
	CaO	9.5	9.71	12.23
	Na_2O	0.81	0.73	0.74
	K_2O	0.5	0.67	0.62
	P_2O_5	n/a	0.7	3.62
	F	n/a	n/a	0.6
in ppm				
	La	58	83.5	1950.2
	Ce	147	211	3860.6
	Sm	25.5	37.5	1936.1
	Eu	2.4	2.72	9163.4
	Gd	n/a	45.4	1926.1
	Lu	2.48	n/a	2210.9

[‡]synthetic starting material used in this study
n/a = not analyzed
n/i = not included in starting mix

Table 2

Experiment #	fO_2 buffer	log(fO_2)	Temp (℃)	Time (mins)	Capsule
ApREE-01a	NNO	-8.02	1175	1380	AgPd
ApREE-01b	NNO	-8.02	1175	1380	Apatite
ApREE-02a	IW	-12.26	1175	2660	AgPd
ApREE-02b	IW	-12.26	1175	2660	AgPd
ApREE-03a	NNO	-8.31	1150	750	AgPd
ApREE-03b	MMO	-12.59	1150	750	Mo
ApREE-04	HM	-3.28	1150	1145	AgPd
ApREE-06	QFM	-9.02	1150	720	AgPd
ApREE-06	IW	-12.59	1150	720	Fe
ApREE-07	HM	-3.28	1150	1500	AgPd
ApREE-07	MMO	-12.36	1150	1500	AgPd
ApREE-09	G-CO-CO_2	-14.51	1150	1275	Graphite
ApREE-12	G-CO-CO_2	-14.93	1110	1090	Graphite
ApREE-12	NNO	-8.81	1110	1090	AgPd
ApREE-12	WM	-10.63	1110	1090	AgPd
ApREE-13a	QFM	-9.53	1110	1590	AgPd
ApREE-13b	WWO	-11.83	1110	1590	AgPd
ApREE-15X	IW	-13.15	1110	1020	AgPd
ApREE-15A-01	MMO	-12.97	1110	1020	AgPd
ApREE-15A-02	MMO	-12.97	1110	1020	Ap

Run products

glass, ap, merr, plag
glass, ap, plag

glass, ap, plag
glass, ap

glass, ap, merr, plag
glass, ap, plag, pyx

glass, merr, ap, plag

glass, ap
glass, ap, pyx

glass, ap
glass, ap

glass, ap, schrib

glass, ap, plag, schrib
glass, ap, plag, spinel
glass, ap, px

glass, ap
only melt

glass, ap, plag
glass, ap, plag
glass, ol, ap

Table 3 Merrillite compositions in oxides and apfu from experiments

	ApREE-01a		ApREE-03a		ApREE-04	
n	24 (3)		48 (7)		15 (3)	
Composition (in wt% oxic	oxide	δ	oxide	δ	oxide	δ
P_2O_5	42.9	2.03	42.65	0.94	41.46	1.62
SiO_2	0.55	0.02	0.65	0.34	1.5	1.02
Al_2O_3	0.02	0.01	0.21	0.6	0.21	0.3
FeO	0.34	0.05	0.65	0.06	0.36	0.14
MnO	bdl	-	bdl	-	bdl	-
MgO	3.45	0.06	3.57	0.13	3.85	0.14
CaO	41.54	0.18	41.36	0.77	40.36	0.49
Na_2O	0.05	0.03	0.05	0.03	0.08	0.02
TiO_2	bdl	-	bdl	-	0.04	0.03
K_2O	bdl	-	bdl	-	bdl	-
La_2O_3	1.08	0.04	1.11	0.06	1.06	0.05
Ce_2O_3	2.23	0.06	2.32	0.11	2.19	0.07
Sm_2O_3	1.26	0.04	1.26	0.07	1.26	0.03
Eu_2O_3	5.24	0.07	5.46	0.27	5.75	0.09
Gd_2O_3	1.47	0.05	1.42	0.09	1.46	0.04
Lu_2O_3	0.39	0.04	0.52	0.06	0.38	0.02
Cl	bdl	-	bdl	-	bdl	-
F	bdl	-	bdl	-	bdl	-
Total	100.55	2.03	101.3	1.16	99.98	1.18
Cations per 56 oxygen at						
P	13.74		13.62		13.39	
Si	0.21		0.24		0.57	
$\sum(P,Si)_{tetra}$	13.95				13.96	
Al	bdl		0.09		0.09	
Ti	bdl		0.01		0.01	
Fe	0.11		0.2		0.11	
Mg	1.95		2.01		2.19	
Ca	16.84		16.72		16.49	
Na	0.04		0.04		0.06	
La	0.15		0.15		0.15	
Ce	0.31		0.32		0.31	
Sm	0.16		0.16		0.17	
Eu	0.68		0.7		0.75	
Gd	0.18		0.18		0.18	
Lu	0.04		0.06		0.04	
$\sum(cations)$	20.46		20.54		20.45	

$\sum$ (REE)	1.53	1.58	1.6
$\sum$ (Mg, Fe)	2.05	2.21	2.3

n = number of analyses (individual grains analyzed)

$\sum$ (P,Si)$_{tetra}$ = sum of phosphorus and silica on the tetrahedral site in merrillite (in apfu)

Table 4
Comparison of apatite-melt experiments

Reference	Pressure (GPa)	Temperature (°C)	*Experimental melt compos*	
			SiO$_2$	Na$_2$O
This study	1	1110 – 1175	39.7 – 50.2	0.2 – 0.8
Prowatke and Klemme	1	1250	35.9 – 61.5	1.3 – 16.8
Watson and Green	0.75 – 2.0	950 – 1120	40.1 – 69.6	3.0 – 4.0

[‡]*The Prowatke and Klemme (2006) experiments contain no initial H$_2$O within the melt but hydroxyapatite within the starting material (i.e., a potential H$_2$O source).*

ition (wt%)

H_2O
0
$0.0^{\mmp}$
0.0-10.4

does contain

Table 5: Lattice strain parameters derived from parabolic fits to equation 5

Experiment		T (°C)	$\log(f O_2)$	E (GPa)	δ	r_0 (Å)
This study						
EPMA	ApREE-01a	1175	-8.02	393	19	0.959
	ApREE-03a	1150	-8.31	372	28	0.957
	ApREE-03b	1150	-12.59	335	18	0.958
	ApREE-04	1150	-3.28	337	25	0.962
	ApREE-06	1150	-9.02	387	5	0.956
	ApREE-06	1150	-12.59	391	4	0.96
	ApREE-07	1150	-3.28	339	34	0.95
	ApREE-07	1150	-12.36	313	22	0.968
	ApREE-09	1150	-14.51	487	22	0.958
	ApREE-12	1110	-14.93	366	11	0.959
	ApREE-12	1110	-8.81	406	6	0.956
	ApREE-13A	1110	-11.83	417	28	0.95
	ApREE-15X	1110	-13.15	388	3	0.953
	ApREE-15A-1	1110	-12.97	427	6	0.96
	ApREE-15A-2	1110	-12.97	318	49	0.958
LA-ICP-MS	ApREE-03a	1150	-8.31	244	5	0.954
	ApREE-03b	1150	-12.36	157	30	0.957
	ApREE-07	1150	-3.28	293	9	0.953
	ApREE-09	1150	-14.51	316	152	0.953
	Average			352	25	0.957
Klemme and Dalpé (2003)						
	BS19	1250	uc.	223	28	0.943
	BS23	1250	uc.	321	95	0.94
	BS25	1250	uc.	405	170	0.94
	Average			316	97	0.941
Watson and Green (1981)						
	818	1080	uc.	327	16	0.96
	822	1120	uc.	385	4	0.952
	Average			356	10	0.956

uc. = unconstrained (i.e., run at intrinsic oxygen fugacity of the experimental medium)

δ	$\ln(D_0)$	δ
0.002	0.416	0.021
0.002	0.347	0.031
0.002	0.335	0.019
0.003	0.285	0.027
0	0.489	0.006
0	0.824	0.004
0.003	0.427	0.039
0.003	0.663	0.023
0.002	0.659	0.025
0.001	0.673	0.012
0	0.539	0.007
0.002	0.518	0.032
0	0.633	0.004
0.001	0.55	0.007
0.005	0.663	0.056
0.001	0.359	0.008
0.005	0.836	0.043
0.012	0.427	0.172
0.12	1.501	0.246
0.009	0.587	0.041
0.004	0.55	0.02
0.01	0.5	0.05
0.01	0.47	0.05
0.008	0.507	0.04
0.001	1.64	0.03
<0.001	1.72	<0.01
0.001	1.68	0.01

Table 7	(Eu3+/ΣEu)Ap as determined by Eu L3 XANES on oriented Apatite			
Experiment	Scan #	Orientation (relative to north)	Eu^{2+} ($\varphi_{(6975.5\ eV)}$)	sigma
ApREE-12				
	ApREE_12_ap4_0	0°	4.960	0.152
	ApREE_12_ap4_60	60°	4.977	0.154
	ApREE_12_ap4_120	120°	5.924	0.160
	ApREE_12_ap3_0	0°	5.815	0.161
	ApREE_12_ap3_60	60°	5.606	0.154
	ApREE_12_ap3_120	120°	5.715	0.156
	ApREE_12_ap2_0	0°	6.072	0.160
	ApREE_12_ap2_60	60°	5.756	0.162
	ApREE_12_ap2_120	120°	5.823	0.159
	ApREE_12_ap1_0	0°	5.956	0.168
	ApREE_12_ap1_60	60°	5.851	0.181
	ApREE_12_ap1_120	120°	6.120	0.165
	Average		5.722	0.161
	Standard deviation		0.337	0.009
ApREE-02				
	ApREE_2_ap1_0	0°	5.154	0.138
	ApREE_2_ap1_60	60°	4.679	0.147
	ApREE_2_ap1_120	120°	5.486	0.145
	ApREE_2_ap2_0	0°	5.723	0.157
	ApREE_2_ap2_60	60°	5.529	0.148
	ApREE_2_ap2_120	120°	5.620	0.148
	ApREE_2_ap3_0	0°	5.282	0.143
	ApREE_2_ap3_60	60°	5.690	0.149
	ApREE_2_ap3_120	120°	5.721	0.155
	ApREE_2_ap4_0	0°	5.934	0.155
	ApREE_2_ap4_60	60°	5.580	0.150
	ApREE_2_ap4_120	120°	5.370	0.148
	Average		5.481	0.149
	Standard deviation		0.330	0.005

Average orientation-dependent % variaton in $Eu^{3+}/\Sigma Eu$
Standard deviation

Eu^{3+} ($\varphi_{(6983.3\ eV)}$)	sigma	arctan	χ^2	reduced χ^2	R-factor	$Eu^{3+}/\Sigma Eu$	% valence change ($\Delta°$)
12.588	0.109	1.034	0.285	0.002	0.001	0.717	
13.467	0.120	1.013	0.364	0.002	0.002	0.730	7.848
12.184	0.114	1.029	0.319	0.002	0.001	0.673	
12.398	0.117	1.032	0.333	0.002	0.001	0.681	
12.987	0.118	1.001	0.358	0.003	0.002	0.698	2.989
12.012	0.109	1.041	0.280	0.002	0.001	0.678	
11.377	0.103	1.082	0.240	0.002	0.001	0.652	
12.692	0.114	1.074	0.308	0.002	0.001	0.688	5.229
11.838	0.109	1.039	0.279	0.002	0.001	0.670	
11.708	0.112	1.072	0.284	0.002	0.001	0.663	
12.667	0.120	1.086	0.329	0.002	0.002	0.684	5.406
11.220	0.107	1.072	0.254	0.002	0.001	0.647	
12.383	0.114	1.044	0.311	0.002	0.001	0.684	
0.711	0.005	0.031	0.039	0.000	0.000	0.024	
12.002	0.107	1.035	0.239	0.002	0.001	0.700	
12.363	0.101	1.059	0.221	0.002	0.001	0.725	7.215
11.296	0.093	1.089	0.182	0.001	0.001	0.673	
11.785	0.107	1.040	0.251	0.002	0.001	0.673	
11.542	0.097	1.078	0.207	0.002	0.001	0.676	1.366
11.251	0.095	1.063	0.197	0.001	0.001	0.667	
11.758	0.095	1.071	0.198	0.001	0.001	0.690	
11.500	0.098	1.071	0.206	0.002	0.001	0.669	5.803
10.624	0.101	1.144	0.171	0.001	0.001	0.650	
11.157	0.097	1.106	0.195	0.001	0.001	0.653	
11.492	0.097	1.085	0.201	0.001	0.001	0.673	3.023
10.761	0.097	1.112	0.163	0.001	0.001	0.667	
11.461	0.099	1.079	0.203	0.001	0.001	0.676	
0.492	0.004	0.031	0.025	0.000	0.000	0.021	
							4.860
							2.232

Table 6

(Eu^{3+}/ΣEu)$_{Ap}$ as determinde by Eu L$_3$ XANES Apatite-melt at random orientations

Experiment	T (K)	buffer	log (fO2)	n	(Eu^{3+}/ΣEu)$_{Ap}$	(δ)
ApREE-01a	1448	NNO	-8.02	6	0.867	0.004
ApREE-02	1448	IW	-12.26	12	0.676	0.021
ApREE-03a	1423	NNO	-8.31	1	0.884	n/a
ApREE-04	1423	HM	-3.28	2	0.907	0.009
ApREE-06	1423	QFM	-9.02	3	0.858	0.005
ApREE-07	1423	HM	-3.28	3	0.882	0.007
ApREE-07	1423	MMO	-12.36	2	0.751	0.021
ApREE-09	1423	C-CO-CO$_2$	-14.51	6	0.567	0.053
ApREE-12	1383	NNO	-8.81	2	0.868	0.004
ApREE-15X	1383	IW	-13.15	3	0.647	0.037
ApREE-2b	1448	IW	-12.59		0.676	0.021

preferred parition coefficients

Experiment	T (K)	buffer	log (fO2)	n	(Eu^{3+}/ΣEu)$_{Melt}$	(δ)
ApREE-01a	1448	NNO	-8.02	2	0.900	0.003
ApREE-03a	1423	NNO	-8.31	1	0.898	n/a
ApREE-04	1423	HM	-3.28	2	0.933	0.000
ApREE-06	1423	QFM	-9.02	2	0.867	0.002
ApREE-07	1423	HM	-3.28	2	0.924	0.001
ApREE-07	1423	MMO	-12.36	2	0.581	0.002
ApREE-09	1423	C-CO-CO$_2$	-14.51	5	0.355	0.006
ApREE-12	1383	NNO	-8.81	2	0.893	0.004
ApREE-15X	1383	IW	-13.15	2	0.515	0.000

$(Eu/Eu*)^{Sm-Gd}$	(δ)	χ^2	D_{Eu3+}	D_{Eu2+}
0.94	0.14	0.28	1.35	1.87
#REF!	#REF!	0.20	n/a	n/a
0.98	0.09	0.29	1.33	1.53
1.03	0.11	0.41	1.29	1.83
0.99	0.09	0.31	1.57	1.70
1.03	0.18	0.34	1.52	2.48
0.74	0.12	0.28	1.70	0.78
0.71	0.15	0.19	2.13	0.89
0.98	0.11	0.36	1.59	2.00
0.69	0.11	0.24	1.60	0.93
0.72	0.21			
			1.81	*0.87*

$(Eu/Eu*)^{Sm-Gd}$	(δ)	χ^2
0.94	0.14	0.28
0.98	0.09	0.31
1.03	0.11	0.42
0.99	0.09	0.33
1.03	0.18	0.36
0.74	0.12	0.24
0.71	0.15	0.29
0.98	0.11	0.35
0.69	0.11	0.26